2-1-2011

Experiments and Simulations on Granular Gases

Hongqiang Wang
University of Massachusetts - Amherst

Recommended Citation

Wang, Hongqiang, "Experiments and Simulations on Granular Gases" (2011). *Open Access Dissertations.* Paper 348.

EXPERIMENTS AND SIMULATIONS ON GRANULAR GASES

A Dissertation Presented

by

HONG-QIANG WANG

Submitted to the Graduate School of the
University of Massachusetts Amherst in partial fulfillment
of the requirements for the degree of

DOCTOR OF PHILOSOPHY

February 2011

Physics

EXPERIMENTS AND SIMULATIONS ON GRANULAR GASES

A Dissertation Presented

by

HONG-QIANG WANG

Approved as to style and content by:

_____

Narayanan Menon, Chair

_____

Jonathan Machta, Member

_____

Anthony Dinsmore, Member

_____

Corey S. O'Hern, Member

_____

Jonathan P. Rothstein, Member

_____

Donald Candela, Department Chair
Physics

To my wife Tingting and my daughter Meisu.

ACKNOWLEDGMENTS

ABSTRACT

EXPERIMENTS AND SIMULATIONS ON GRANULAR GASES

FEBRUARY 2011

HONG-QIANG WANG

B.Sc., NANJING UNIVERSITY

M.Sc., NANJING UNIVERSITY

M.D., UNIVERSITY OF NEVER-NEVER-LAND

Ph.D., UNIVERSITY OF MASSACHUSETTS AMHERST

Directed by: Professor Narayanan Menon

In this thesis we report experimental and simulation study of granular gases. As a non-equilibrium system composed of macroscopic particles, a granular gas often shows a picture similar to a molecular gas in that the system is dilute and particles interact with each other through instantaneous collisions. Unlike in molecular gases, the collisions are inelastic so that the interactions are a continuous sink of kinetic energy. The study of granular gases is not only of theoretical interest as an important example of non-equilibrium physics, but also of practical value since granular materials play an important role in many industrial processes and natural phenomena. In this dissertation, we study some of the open questions about the statistical properties of granular gases.

We investigate the role of the heating mechanism in determining the extent of non-equipartition of kinetic energy. Two species of particles in a binary granular system

typically do not have the same mean kinetic energy, in contrast to the equipartition of energy required in equilibrium. In most experiments, different species are unequally heated at the boundaries. We show by event-driven simulations that differential boundary heating affects the degree of non-equipartition even in the bulk of the system. This conclusion is fortified by studying numerical and solvable stochastic models without spatial degrees of freedom. In both cases, even in the limit where heating events are rare compared to collisions, the effect of the heating mechanism persists.

We have also performed an experimental study of particle kinematics in a three-dimensional system of inelastic spheres fluidized by intense vibration. The motion of particles in the interior of the medium is tracked by high-speed video imaging, yielding a spatially resolved measurement of the velocity distribution. The distribution is wider than a Gaussian and broadens continuously with increasing volume fraction. The deviations from a Gaussian distribution for this boundary-driven system are different in sign and larger in magnitude than predictions for homogeneously driven systems. We also find correlations between velocity components which grow with increasing volume fraction.

Following a recent experiment[Phys. Rev. Lett. **92**, 164301(2004)] we study two kinds of power fluctuations in a two dimensional granular gas by event-driven molecular dynamics simulations. Taking advantage of the convenience of changing system parameters in computer simulations, we explore this topic in greater detail. The fluctuation relation by Gallavotti and Cohen is applied to two kinds of power fluctuations for both vibrational boundary driving and static thermal boundary driving. The physical properties of the effective temperatures arising from the fluctuation relation is studied. Our numerical experiments directly checked the various aspects in applying fluctuation theorem to granular gases and leave some open questions.

TABLE OF CONTENTS

LIST OF FIGURES

xiii

xiv

xv

CHAPTER 1

INTRODUCTION

Granular matter is the term used for a variety of materials commonly seen in nature and daily lives. Their general form is an accumulation of macroscopic solid grains. Examples range from flour, rice, nuts, salt and pharmaceutical powders, to rocks, sand, coal and even the rings of planets like Saturn. Handling of granular matter is important in many industrial processes. The manipulation of seeds, grains, flours in the food industry, processing of powders and pills in the pharmaceutical industry, and grinding of ore in the mining industry are a few examples. Granular matter also relates to many geophysical phenomena and disasters, such as desert dune formation, land slides, and snow avalanches etc.. As de Gennes [1] said, if measured by weight, granular matter is the second-most-manipulated materials, after only water. However, the complexity of the collective behavior of these materials often exceeds people's intuition. Under different conditions, mostly related to the intensity of external excitation and system volume fraction, granular matter can stay at rest like a solid resisting to external shearing, flow like a fluid, and behave like a gas if maintained in a dilute state. These complex behaviors have led to the claim that granular matter is a distinct state of matter in its own right in addition to solids, liquids and gases[2].

Existing so widely in nature, these systems share some general features. Granular grains are macroscopic in size, so that Brownian motion is irrelevant. As an example, the typical energy scale for rearranging a single grain in a packing is mgd, where m is the mass of the grain, d the diameter and g the acceleration due to gravity. For a grain

with diameter 1mm and mass 1mg, the energy scale will be 10^{-11}J, which is much higher than $K_B T$(at room temperature $\sim 10^{-21}$J). The ordinary thermodynamics arguments for calculating statistical properties of an ensemble fail because grains can not explore phase space with the help of thermal fluctuations. In addition to their non-thermal nature, the inter-grain interactions are dissipative. In a dry granular system the grains interact with each other only via repulsive contact forces. After a collision of two moving grains, part of the total kinetic energy is lost and transferred to other forms, such as thermal energy of the grains, plastic deformations, microcrack formation, and attrition([3, 4, 5]). The energy dissipated and transformed to other forms is usually irrelevant to the dynamics of grains. Without external energy supply, the kinetic energy of the fluidized granular system is lost quickly and all grains come to rest finally under gravity. A fluidized steady state is possible only with a continuous energy supply. With sufficient external energy supply, granular materials can be fluidized and exhibit almost all known hydrodynamic behavior and instabilities, such as Rayleigh-Bénard convection, Taylor-Couette flows, gravity waves, shear flows etc.. This does not mean that granular fluids will necessarily behave the same as molecular fluid. The dissipative nature of granular grains causes new instabilities such as oscillons, clustering [6] and collapse[7] that are unknown in conventional regular hydrodynamics. Compared with classical molecular fluids, the number of grains is far less than the Avogadro's number, which leads to great fluctuations of statistical quantities. In addition, there is absence of size-scale separation and time-scale separation [8] in the fluids, which is usually an important assumption in regular hydrodynamic theories. The dissipative collisions and the non-thermal nature make granular matter rich in phenomena and complicated in physics.

Research on granular matter can be dated back to Coulomb, Faraday and Reynolds, but for a long time, little attention was paid to granular matter except for specific engineering purpose. In the last twenty years, physicists have developed an interest

in the study of granular matter both because of their practical importance as well as for their interest as a model of non-equilibrium system. In this dissertation, we focus on rapid granular flows, often referenced as granular gases.

1.1 Introduction to granular gases

A highly fluidized granular system is often referred as a granular gas (or rapid granular flows) where the grains interact with each other only through instantaneous collisions. Although in real world granular grains are often embedded in air or other ambient fluids, the forces exerted from the interstitial fluid can be small compared with inter-particle forces in many situations. The influence from the surrounding air is often neglected in theoretical modelling, simulations and practical experiments. A snapshot of a granular gas would be hard to differentiate from an elastic counterpart. It is not surprising that the theoretical study of granular gases starts with the similar framework of classical hydrodynamics of molecular gases, where the granular grains playing the role of molecules.

Grains existed in nature are usually non-spherical and polydisperse. The real interactions of these grains are complicated, including short range repulsive force in normal direction, tangential frictional force for dry grains. To simplify the interactions in theories and simulations, the grains are often modelled as disks in 2D and spheres in 3D, with a key feature that part of the total kinetic energy is lost after a collision. Grains are either hard or soft, with zero or finite collision time. The interaction is in the normal direction for smooth particles and involves tangential forces for rough particles.

Among the various models, the *Inelastic Hard Sphere*(IHS) model of smooth grains with a finite restitution coefficient is most commonly used in kinetic theories of granular gas. This model capture the discrete and inelastic nature of granular particles while discarding all other complexity. Consider two grains with velocities $\mathbf{v_1}$ and $\mathbf{v_2}$

colliding with each other with a unit vector $\hat{\sigma}$ pointing from the center of the second grain to the center of the first grain. The velocities after the collision $\mathbf{v_1'}$ and $\mathbf{v_2'}$ are determined by linear momentum conservation,

$$m_1\mathbf{v_1'} + m_2\mathbf{v_2'} = m_1\mathbf{v_1} + m_2\mathbf{v_2} \tag{1.1}$$

and a reduction of relative normal velocity quantified by the restitution coefficient η as,

$$\hat{\sigma} \cdot \mathbf{v_{12}'} = -\eta(\hat{\sigma} \cdot \mathbf{v_{12}}) \tag{1.2}$$

thus,

$$\mathbf{v_1'} = \mathbf{v_1} - \frac{m_2}{m_1 + m_2}(1 + \eta)(\hat{\sigma} \cdot \mathbf{v_{12}})\hat{\sigma} \tag{1.3}$$

$$\mathbf{v_2'} = \mathbf{v_2} + \frac{m_1}{m_1 + m_2}(1 + \eta)(\hat{\sigma} \cdot \mathbf{v_{12}})\hat{\sigma} \tag{1.4}$$

where $\mathbf{v_{12}} = \mathbf{v_1} - \mathbf{v_2}$ and $\mathbf{v_{12}'} = \mathbf{v_1'} - \mathbf{v_2'}$. Total energy loss after a collision is $(1 - \eta^2)m_1m_2(\hat{\sigma} \cdot \mathbf{v_{12}})^2/(2(m_1 + m_2))$.

As in the case of molecular gas, one can define the single grain distribution function $f(\mathbf{v}, \mathbf{r}, t)$ and basic macroscopic fields such as granular temperature T, velocity $\mathbf{V}$ and mass density ρ(or number density n). $f(\mathbf{v}, \mathbf{r}, t)$ is defined as the number density of grains having velocity $\mathbf{v}$ at position $(\mathbf{r}, t)$. The ensemble average number density, n, the velocity field, $\mathbf{V}$, and the granular temperature T, can be expressed as averages with respect to the single-particle distribution function, f, as follows:

$$n(\mathbf{r}, t) = \int d\mathbf{v} f(\mathbf{v}, \mathbf{r}, t) \tag{1.5}$$

$$\mathbf{V}(\mathbf{r}, t) = \frac{1}{n(\mathbf{r}, t)} \int d\mathbf{v} \; \mathbf{v} f(\mathbf{v}, \mathbf{r}, t) \tag{1.6}$$

and

$$T(\mathbf{r}, t) = \frac{1}{n(\mathbf{r}, t)} \int d\mathbf{v}(\mathbf{v} - \mathbf{V})^2 f(\mathbf{v}, \mathbf{r}, t) \tag{1.7}$$

4

It is necessary to point out that the granular temperature here is a measurement of the average of the square of the fluctuating velocities, thus has nothing to do with the internal thermodynamic temperature of the grains. In terms of energy scale, the granular temperature here is much higher than the thermodynamics temperature.

Standard kinetic theory starts from the inelastic Boltzman equation, corresponding to above model, in $D = 2$ or 3 dimensions,

$$
\frac{\partial f(\mathbf{v}_1, \mathbf{r}, t)}{\partial t} + \mathbf{v}_1 \cdot \nabla f(\mathbf{v}_1, \mathbf{r}, t)
$$
$$
= \sigma^{D-1} \int_{\hat{\sigma} \cdot \mathbf{v}_{12} > 0} d\mathbf{v}_2 d\hat{\sigma} (\hat{\sigma} \cdot \mathbf{v}_{12}) (\frac{1}{\eta^2} f(\mathbf{v}_1', \mathbf{r}, t) f(\mathbf{v}_2', \mathbf{r}, t) - f(\mathbf{v}_1, \mathbf{r}, t) f(\mathbf{v}_2, \mathbf{r}, t)) \quad (1.8)
$$

The integral is over grains approaching each other(that can collide). The positive(negative) term in the right hand side of the equation are called the gain(loss) term correspondingly, because it increase(decrease) the number of grains with velocity v_1. A pre-factor $\frac{1}{\eta^2}$ precedes the gain term to reflect the phase space shrink due to inelastic collisions.

At small inelasticity(η close to 1), a perturbative method by expanding the distribution function around the Maxwell-Boltzmann distribution is commonly used to solve this inelastic Boltzmann equation.

The Boltzmann equation is derived for dilute granular gases that interact via short-range repulsive interactions. The key assumption is *molecular chaos*, or Stosszahlansatz, which assumes that the velocities of colliding grains just before collisions are uncorrelated, i.e. the pair-distribution function $f(\mathbf{v}_1, \mathbf{r}_1, \mathbf{v}_2, \mathbf{r}_2, t) = f(\mathbf{v}_1, \mathbf{r}_1, t) f(\mathbf{v}_2, \mathbf{r}_2, t)$. $f(\mathbf{v}_1, \mathbf{r}_1, \mathbf{v}_2, \mathbf{r}_2, t)$ denotes the joint probability density of having two grains with grain 1 at position $\mathbf{r}_1$ with velocity $\mathbf{v}_1$ and grains 2 at position $\mathbf{r}_2$ with velocity $\mathbf{v}_2$.

Enskog's extension of the Boltzmann equation to a dense gas, known as Enskog-Boltzmann equation, is also based on the assumption of the absence of velocity correlation before collisions. The factorization of pair-distribution is revised as $f(\mathbf{v}_1, \mathbf{r}_1, \mathbf{v}_2, \mathbf{r}_2, t) =$

$\chi(\phi)f(\mathbf{v}_1, \mathbf{r}_1, t)f(\mathbf{v}_2, \mathbf{r}_2, t)$. The prefactor $\chi(\phi)$ is the radial pair distribution function at contact in local equilibrium, which is a function of volume fraction ϕ and usually taken from equilibrium results for elastic hard grains(see [9]). It accounts for the increased collision frequency in dense systems. The corresponding Enskog-Boltzmann equation in the absence of external forces is

$$
\begin{aligned}
&\frac{\partial f(\mathbf{v}_1, \mathbf{r}, t)}{\partial t} + \mathbf{v}_1 \cdot \nabla f(\mathbf{v}_1, \mathbf{r}, t) \\
&= \chi \sigma^{D-1} \int_{\hat{\sigma} \cdot \mathbf{v}_{12} > 0} d\mathbf{v}_2 d\hat{\sigma} (\hat{\sigma} \cdot \mathbf{v}_{12}) (\frac{1}{\eta^2} f(\mathbf{v}_1', \mathbf{r}, t) f(\mathbf{v}_2', \mathbf{r}, t) - f(\mathbf{v}_1, \mathbf{r}, t) f(\mathbf{v}_2, \mathbf{r}, t)). \quad (1.9)
\end{aligned}
$$

This molecular chaos assumption is not fully justified for granular gases, but under low density and close to elastic conditions it seems to work(see [10] and references therein).

The exact solution for Enskog-Boltzmann equation is unknown. A special case often under consideration is the spatially homogeneous granular gas. Therefore, the second term in equation (1.9) is omitted and the single particle distribution function is now a function of velocity. Following the standard Chapman-Enskog expansion[11], the time dependence of the distribution function is replaced by a dependence on the time-dependent hydrodynamics fields. Such hydrodynamics fields are supposed to not change much over the mean free path. Most earlier theories are based on the assumption that the distribution of particle velocity is Gaussian. This is found to be not true by many experiments and simulations. Another common choice is expanding the distribution function around Gaussian with Sonine polynomials.

By multiplying the Boltzmann equation with $1, v_1$ and v_1^2, the continuum hydrodynamics equations are obtained,

$$
\frac{dn}{dt} + n\nabla \cdot \mathbf{v} = 0, \quad (1.10)
$$

$$
n\frac{d\mathbf{v}}{dt} = n\mathbf{F} - \nabla \cdot \mathbf{P}, \quad (1.11)
$$

$$n\frac{dT}{dt} + P : \nabla \mathbf{v} - \nabla \cdot \mathbf{q} = -n\Gamma. \tag{1.12}$$

where n is the number density defined in 1.5, $\mathbf{F}$ is the external body force per unit molecular, P is the pressure tensor, $q \equiv \frac{1}{2}n < |v|^2 \mathbf{v} >$ is the heat flux vector and Γ is the rate of energy dissipation due to collisions and can be given as

$$\Gamma = \frac{\pi(1-\eta^2)\sigma^2}{8n} \int d\mathbf{v_1} d\mathbf{v_2} v_{12}^3 f(\mathbf{v_1}) f(\mathbf{v_2}). \tag{1.13}$$

Jenkins, Savage[12] and Lun *et al*[13] pioneered kinetic theories of the inelastic particle flow with these balance equations.

1.2   Current experimental and simulation methods

A steady state granular gas only exists when there is a continuous energy supply. Generally, we should distinguish two types of heating. In experiments, external heating is commonly through mechanical driving at boundaries, either vibration or shearing. A density and granular temperature gradient is built with increasing distance from heating boundaries. In kinetic theory treatments, starting from the inelastic Boltzmann equation, a uniform heating is more typically considered. Granular gases are heated through volumetric forces leading to a spatially homogeneous distribution without any macroscopic gradient fields. One common way of homogeneous heating is volumetric Gaussian white noise forcing, in which random uncorrelated forces accelerate particles between subsequent collisions. The motion is analogous to Brownian motion between collisions with kinetic energy dissipated through inelastic collisions in stead of hydrodynamic drag.

The experimental study of granular gases consists of two important technical steps: fluidizing the granular system and extracting information from the system for further analysis. Usually the grains under study are balls made of steel, glass and plastic materials etc. or grains obtained from natural sources, such as sands, seeds and nuts

etc. Typical experimental choices for the external mechanical forces to fluidize the system include vibration, shearing, rotating and gravity(see reference[2]). Although the quantitative measurement of the movements of individual grains is not required in all experiments, there are a few methods capable of tracking with a high resolution to individual particles. Optical imaging provides the most straightforward option. By a high-speed camera and special computer analysis, a collection of individual grains can be tracked. This method works powerfully in two dimension[14] and we have applied it to three dimension. Positron-Emission Particle Tracking(PEPT)[15] and Nuclear Magnetic Resonance Imaging[16] provide other choices for studying three dimensional systems. Although not as straightforward as optical methods, they can help explore the temperature and density profiles inside opaque 3D granular systems.

In our experimental system, a cage is mounted on top of a electromechanical vibrator, *Ling Dynamics Systems(LDS)*, model V400, driven by an *LDS* amplifier, model PA500L. Spherical grains are confined in the cage. A function generator HP(Hewlett-Packard) 33120A controls the vibrator to vibrate at desired frequency, amplitude and wave form - usually sinusoid. Grains are fluidized by collisions with the top and bottom walls of the vibrating cage. A high-speed camera located in the front images the motion of grains. An image analysis procedure, called particle tracking[17, 18] is then used to identify individual tracks of grains from these discrete video images.

Besides experiments, computer simulations provide another powerful method to explore granular gases. Compared with experimental methods, computer simulation can study many properties hard to measure in experiments. Changing of system parameters is also much easier. Of course, computer simulation works on the basis of simple models for the interaction of particles and other assumptions. Reliable computer simulations depend on how well the models and algorithms can capture the important characteristics of real granular systems.

Common simulation methods used in studying fluidized granular matter include time driven molecular dynamic method, event-driven molecular dynamics method and direct simulation Monte Carlo method. We will give a brief introduction to two kinds of molecular dynamics methods here.

The most widely used simulation method in studying granular gases is the event-driven molecular dynamics simulation method. It assumes free motion of grains until they collide with other grains or boundaries. During the free motion, the track of the grain is determined by deterministic kinetic equations of motion given its initial velocity and position. In the collision stage, the velocities of the two colliding grains are updated instantaneously from their velocities before the collision. If the collision is between a grain and the boundary, then usually only the velocities of the grain are updated since the boundaries are typically treated as infinitely massive. After each collision, the time for the next collision is calculated from the updated system and the next most immediate event for the whole system is picked up for the next update. In such a way, a continuous list of events can be built and the system can evolve as long as people want.

Since most of the simulations we discuss in this dissertation are based on event-driven molecular dynamics method, we introduce below the collision model we use[19, 20].

Suppose $\mathbf{v}$ and ω are translational and rotational velocity before collision, $\mathbf{v}'$ and ω' are translational and rotational velocity after collision.

Define: $\hat{\sigma} = \frac{\mathbf{r_1} - \mathbf{r_2}}{|\mathbf{r_1} - \mathbf{r_2}|}$

The relative velocity at the contact point is $\mathbf{v_c} = \mathbf{v_1} - \mathbf{v_2} - \left(\frac{d_1}{2}\omega_1 + \frac{d_2}{2}\omega_2\right) \times \hat{\sigma}$

So the linear momentum change of particle 1 is $\triangle\mathbf{P} = m_1(\mathbf{v_1'} - \mathbf{v_1}) = -m_2(\mathbf{v_2'} - \mathbf{v_2})$

Due to $-\hat{\sigma} \times \triangle\mathbf{P} = \frac{2I}{d}(\omega' - \omega)$, the final velocity is determined by $\triangle\mathbf{P}$

$$\mathbf{v_1'} = \mathbf{v_1} + \triangle\mathbf{P}/m_1 \tag{1.14}$$

$$\omega_1' = \omega_1 - \frac{d_1}{2I_1}\hat{\sigma} \times \triangle\mathbf{P} \tag{1.15}$$

$$\mathbf{v_2'} = \mathbf{v_2} - \triangle\mathbf{P}/m_2 \tag{1.16}$$

$$\omega_2' = \omega_2 - \frac{d_2}{2I_2}\hat{\sigma} \times \triangle\mathbf{P} \tag{1.17}$$

Next, $\triangle\mathbf{P}$ is determined using momentum and angular momentum conservation in combination with empirically motivated rules governing the inelastic interaction.

For normal component of the momentum change, $\triangle\mathbf{P}^{(n)}$, using the definition of the coefficient of normal restitution

$$\mathbf{v_c'}^{(n)} = -\eta\mathbf{v_c}^{(n)},$$

So

$$\triangle\mathbf{P}^{(n)} = -m_{12}(1+\eta)\mathbf{v_c}^{(n)} \tag{1.18}$$

where $m_{12} = m_1 m_2/(m_1 + m_2)$.

For tangential component of momentum change, it is necessary to distinguish two kinds of cases, i.e. sliding case and sticking case(also called Coulomb contact).

In the sticking case $\mathbf{v_c'}^{(t)} = -\beta\mathbf{v_c}^{(t)}$;

In the sliding case(Coulomb contact) $|\triangle\mathbf{P}^{(t)}| = \mu|\triangle\mathbf{P}^{(n)}|$;

Thus two parameters β and μ are introduced to determine the tangential momentum change. If we set $\beta_1 = -1 - (1+\frac{1}{q})\mu(1+\eta)\cot(\gamma)$,

where γ is the angle between $\hat{\sigma}$ and v_c, q is the dimensionless coefficient of the moment of inertia about the center of a particle (for disk, $q = \frac{1}{2}$, for sphere $q = \frac{2}{5}$) we can express these two cases in one formula

$$\triangle\mathbf{P}^{(t)} = -m_{12}(1+\beta)\frac{1}{1+\frac{1}{q}}\mathbf{v_c}^{(t)} \tag{1.19}$$

and now it is needed to introduce a constant β_0 with $-1 \leq \beta_0 \leq 1$to determine when it is the sliding case and when it is the sticking case. Generally, $\beta = \min[\beta_0, \beta_1]$. If

10

$\beta = \beta_1$, it is sliding case; if $\beta = \beta_0$, it's sticking case. So that using Eq. 1.18 and Eq. 1.19 $\triangle \mathbf{v}' P$ are determined.

To avoid inelastic collapse, in which grains undergo an infinite number of collisions, the normal elastic coefficient ϵ used in simulations is not a constant[21].

$$\eta(v_c^{(n)}) = \begin{cases} 1 - (1-\eta)(|v_c^{(n)}|/v_0)^{3/4}, & \text{for} \quad v_c^{(n)} < v_0 \ ; \\ \eta, & \text{for} \quad v_c^{(n)} > v_0 \ , \end{cases} \qquad (1.20)$$

For the normal relative velocity $v_c^{(n)}$ less than a crossover velocity v_0, the elastic coefficient becomes velocity dependent; the smaller the normal relative velocity is, the more elastic the collision is. Therefore, the velocity dependent η contains the benefit of both high computation efficiency at high velocity and the ability to avoid inelastic collapse. Experimental measurements also show that η decreases as $v_c^{(n)}$ increases(see[22]).

Comparing with the time driven molecular dynamics simulation method, event-driven molecular dynamics simulation methods are closer to models used in kinetic theories and are often utilized to compare with results derived from kinetic theories. But time driven molecular system is also useful in many cases, especially in dense granular systems when the instantaneous binary collision assumption can not be guaranteed. So that we also introduce time driven molecular dynamics method briefly.

The inter-grain interaction model in time driven molecular dynamics simulation is no longer a collisional model but rather determined by force calculations for grains at contact. To capture the inelastic interactions between granular grains, their interaction forces need to be non-conservative. The grains are modelled with soft potentials that allow overlap between two grains when they are at contact. There are already a number of models developed and we will introduce a variation[23] of one developed by Haff and Werner[24] here.

Soft grains with both translational and rotational degrees of freedom are modelled with a continuous potential. Two grains interact with each other when the distance between them is less than the sum of their radii, $r_{ij} = |\mathbf{r_i} - \mathbf{r_j}| < d$. Their forces exerted on each other during this collision process is expressed as

$$F_{ij} = ((k_n(d - r_{ij}) - \gamma_n m(\mathbf{v_{ij}} \cdot \hat{\sigma}/2)\hat{\sigma} + min(-\gamma_s m v_{rel}/2, \mu|\mathbf{F} \cdot \hat{\sigma}|)\hat{\mathbf{s}}, \qquad (1.21)$$

where $v_{rel} = \mathbf{\dot{v}_{ij}} \cdot \hat{\mathbf{s}} + d(\omega_i + \omega_j)/2$, $\hat{\sigma} = (\mathbf{r_{ij}} \cdot \hat{\mathbf{x}}, \mathbf{r_{ij}} \cdot \hat{\mathbf{y}})/r_{ij}$, $\hat{\mathbf{s}} = (\mathbf{r_{ij}} \cdot \hat{\mathbf{y}}, \mathbf{r_{ij}} \cdot \hat{\mathbf{x}})/r_{ij}$, and ω_i, ω_j are the angular velocity of grain i and j. k_n describe the elastic constant for deformations along the normal direction while γ_n characterize the normal damping constant which is proportional to the normal relative velocity. The shear force is determined by the shear damping constant, the relative tangential velocity and normal friction coefficient μ and normal force $|\mathbf{F} \cdot \hat{\sigma}|$. Choose a minimum between $-\gamma_s m v_{rel}/2$ and $\mu|\mathbf{F} \cdot \hat{\sigma}|)$ to distinguish sliding contact and Coulomb contact.

With the force model defined, standard molecular dynamics simulations can be carried out. To maintain the system in a steady state, various external driving forces can be introduced as needed. The path of individual grains are integrated based on their velocities and these velocities are updated by the interaction forces(i.e. corresponding to acceleration). With force driven model, granular gas flow with hydrodynamic interaction can be simulated[25].

Time driven molecular dynamics method is easy to implement and particularly suitable for simulating dense granular flows. The shortcoming is that even the grain is not at contact with other objects, it is still necessary to calculate the force and integrate the path of this grain for each time step. This is quite time consuming and unnecessary in many cases, especially for a dilute granular gas where most of the time particles are moving freely. Under the additional assumption that the collision of grains are binary and instantaneous, event-driven molecular dynamics greatly im-

proves the computing efficiency while still capture the important characteristics of discrete and inelastic interactions between granular grains.

1.3 Open questions

Over the past a few years, there have been vast amount literatures published on granular gases that both improved our understanding and bring new challenges in this field. The common theoretical approach to the kinetic description of granular gases, the mean field-type Boltzmann or Enskog-Boltzmann equation is used for low elastic(with restitution coefficient close to 1) granular gases. Qualitative agreement has been found comparing the current approximations in solving the equations with computer simulations or experiments, but the limitation and accuracy for higher inelasticity and volume fraction is unknown. To be maintained in a steady state, a continuous energy supply is necessary. The influence of the internal dynamics from the external heating still impose challenges to the statistical description of granular gases. Due to the limitation of current experimental methods, understanding of granular gases from microscopic statistics to macroscopic fields still needs to be improved. In this dissertation I study some of the open questions of granular gases using simulation and experimental methods described earlier in this chapter.

Energy non-equipartition is an interesting example to show the difference between granular gases and molecular gases. Two species of granular particles typically do not sustain in the same kinetic temperature in a mixture. Though this phenomena has been found in homogeneously heated granular gases, homogeneously cooling granular gases and boundary driven granular gases, little attention has been paid the the role of external heating in affecting this energy equipartition. In the second chapter of this dissertation, we study the energy non-equipartition level with differentiated boundary driving. The influence on energy equipartition from external heating is studied by molecular dynamics simulations, a numerical model and a solvable stochastic model.

Our study not only improves our understand of this phenomenon in a binary granular mixture, but also suggests that it might be hard to completely remove the influence of boundary conditions on the internal dynamics of a granular gas.

The three-dimensional experimental microscopic measurements of granular dynamics is lacking by comparison with those done in a two dimensional granular gas mainly due to the limitation of current experimental technique. Full field tracking of individual granular particles in three dimension is much harder than in two dimension. The two dimensional confinement does not exist in a three dimensional case, thus leading to less mechanical influence from the boundaries. We carry out high speed video imaging experiments to study the kinematics of a vibration fluidized three dimensional granular gas. The distribution function is a crucial descriptor of the statistics of a granular gas. By developing algorithms to identify particles moving in the bulk, we are able to give a detailed measurement of the distribution function of a three dimensional granular gas. Our experimental measurements of granular kinematics represent a major advance over the two dimensional experiments, and our finding demands for the development of better kinetic theories.

Granular gases provide a simple example of a non-equilibrium systems. The building of statistical mechanics description of non-equilibrium systems impose a big challenge to physicists. A recent progress is the so-called fluctuation theorem which is summarized as fluctuation relation[26] that applies to systems far from equilibrium. The fluctuation relation states as:

$$\Pi(\sigma_\tau)/\Pi(-\sigma_\tau) = \exp(\sigma_\tau \tau) \tag{1.22}$$

, where $\Pi(\sigma_\tau)$ is the probability of observing a positive entropy production rate σ_τ, measured over a time interval τ and the relation strictly hold as τ goes to infinity. As there is no good definition of entropy production in a granular gas, we study two kinds of power fluctuations in a two dimensional granular gas by event-driven molec-

ular dynamics simulations. Two kinds of power fluctuations including vibrational boundary driving and static thermal boundary driving are used to generate density and granular temperature gradients away from the boundaries. We test the fluctuation relation with the entropy production replaced by power fluctuation. We can define a quantity with the unit of temperature. The properties of this effective temperatures is then explored. Our simulations directly probe the possibility of applying fluctuation theorem to granular gases and also leave some open questions.

CHAPTER 2

EXTERNAL HEATING AND ENERGY EQUIPARTITION IN A BINARY GRANULAR MIXTURE

In this chapter, we examine the role of external heating in affecting energy equipartition of a binary granular mixture. By molecular dynamics simulation two species of granular particles are selectively heated at boundaries and we find that the kinetic temperature, or mean kinetic energy of these two species of particles is different and significantly affected by the differential boundary heating level. A numerical model and a stochastic model are developed for a similar binary granular system but without spatial ingredients to further strengthen the conclusion.

2.1   Introduction

Energy non-equipartition in a granular mixture is intriguing due to its dissimilarity with the equilibrium counterpart where the "zeroth law" of thermodynamics applies. When different species of materials are in thermal contact, a thermal equilibrium state will finally be reached where all components are at the same thermal temperature. For a particulate system, this thermal temperature is usually defined as the mean kinetic energy per degree of freedom. Take air as an example: nitrogen and oxygen generally share the same mean kinetic temperature although their molecular weights are different. However, if we mix two species of granular particles together and maintain them in a steady state by a continuous external energy supply, these two species of particles typically do not attain the same kinetic temperature, no matter how long we wait.

Although as a non-equilibrium system, there is no requirement for equilibrium thermodynamics, like the "zeroth law" of thermodynamics here, to apply for a granular gas, it is still undeniable that a statistical description of a granular gas, in analogy with equilibrium thermodynamics of a molecular gas, has achieved big success over the past ten to twenty years[5]. By defining a few macroscopic fields quantities, such as granular kinetic temperature, velocity and mass density, the inelasticity of granular particles can be incorporated into the kinetic description. The statistical properties, can be studied under the framework of inelastic Boltzmann equation or continuum equations.

A dilute system of granular particles is different from an equilibrium gas in that a continuous energy supply from an external source is necessary to maintain a steady state and replenish the energy dissipated by inelastic collisions between particles. In a typical real-world situation, the energy is input at the boundaries of the system by vibration, shear or other mechanical means. Due to the inelastic collisions, there are always gradients in density and particle motions as a function of distance from the energizing boundary, in contrast to an equilibrium gas where a uniform temperature and density field will build when the gas is placed in contact with a heat bath. For dilute gases of inelastic particles there has been considerable progress in describing the resultant inhomogeneous steady state in terms of density and "temperature" fields.

The necessity of external heating immediately introduces a further degree of complexity when one considers a system with two species of particles. There is no guarantee from equipartition that the two species acquire the same kinetic temperature, and indeed, a number of recent experimental [27, 28, 29] and simulation studies [30, 31, 32, 33] document this violation of equipartition. It is observed that two species a and b acquire temperatures whose ratio $\gamma \equiv T_a/T_b$ is affected strongly by the ratio of particle masses, m_a/m_b, and weakly by their inelasticity. The temperature ratio γ is also observed [28]to be only weakly affected by the composition -

the overall number density and stoichiometry - of the mixture. These observations have been reproduced and more comprehensively explored by event-driven simulations [30, 31, 33] of vibration-fluidized systems. Montanero and Garzo[34] have also studied a sheared granular mixture and shown energy non-equipartition by Direct Monte Carlo simulations and nonlinear Boltzmann equations.

However, a further, and often-neglected ingredient in this problem is that in a typical granular fluid, the driving mechanism couples differently to particles with different properties. For instance, in a vibration-fluidized system [27, 28, 29], the vibrating boundaries may be treated as infinitely massive, and therefore, impart a characteristic velocity scale (rather than an energy scale) to the particles. If the particles in the system are of different mass, then they are differentially heated at the boundary. This is not an issue in an equilibrium system, where even if the two species are coupled differently to a heat bath, equipartition is regained in the bulk of the system. In the granular systems under consideration, the temperature ratio γ is experimentally observed [28]to be close to the mass ratio of the two species of particles near the boundary, and then attain an apparently constant value after a few mean free paths. The question remains whether this apparently constant bulk value depends on the boundary condition.

This raises the question of whether the extent of departure from equipartition can be theoretically predicted, that is, can the temperature ratio, γ be expressed in terms of specified properties of the two particles in the mixture. If this were to be true, then it would not be necessary to introduce independently varying temperature fields to describe each species in the mixture. In fact, this question has been addressed theoretically in spatially homogeneous systems. Garzo and Dufty[35] studied theoretically the homogeneous cooling process of a binary granular mixture in which the two species were endowed with an initial temperatures. They found that the cooling rates of the two species are the same while their temperatures remain different,

thus maintaining a time-independent γ. Their calculation revealed the dependence of the temperature ratio on the mechanical properties of the particles, including the restitution coefficients, the reduced density, and the ratio of mass, concentration and sizes. A mean-field model of free-cooling inelastic granular mixtures by Marconi and Puglisi[36] demonstrate the existence of two different partial temperatures for the two components. There has also been theoretical work on homogeneously heated mixtures, where both types of particles get occasional velocity boosts from a noise source[30]. Morgado[37] computes the coexistence of different granular temperatures by a Langevin-like inelastic collision model in 1D.

We investigate the role of the heating mechanism in determining the extent of this non-equipartition of kinetic energy. In most experiments, different species of particle are unequally heated at the boundaries. We demonstrate that not only mechanical properties of particles influences the level of non-equipartition, but also this differential heating at the boundary.

2.2 Simulation method

In our event-driven simulations, two types of smooth discs (labelled a and b), both of diameter d, but with different masses, are fluidized inside a rectangle of dimensions $48 \times 32d$(see Fig.2.1). These simulation parameters are chosen to mimic an experimental geometry previously studied by us [28]. For the simulations reported here, the ratio of particle masses m_b/m_a is 5, the restitution coefficient of both species is 0.93 and an equal number of both species are used with the total number of particles 2N=200 corresponding to area fraction 10.2%. We set $g = 0$ and employ periodic boundary conditions in the horizontal (x) direction. In order to isolate the effects we are concerned with, we choose to heat the particles using fixed "thermal" walls rather than with the additional space- and time-dependence introduced by oscillating walls. Following a collision with the top or bottom boundary, a particle is reflected
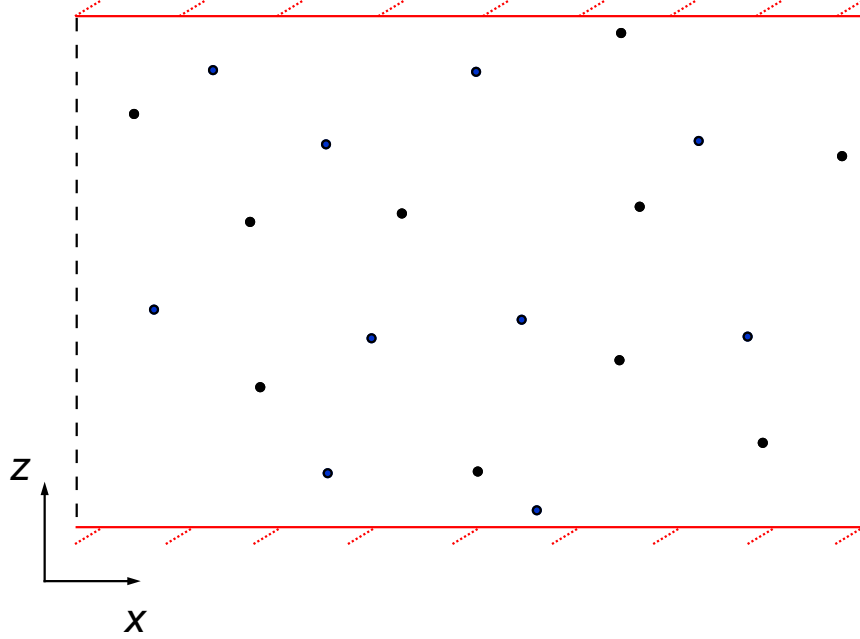
Figure 2.1. A cartoon illustration of our simulation system. Two types of particles are confined in a $48d \times 32d$ box and heated from fixed top and bottom boundaries. Periodic boundaries are applied in the horizontal direction.

with normal and tangential velocity components independently drawn from gaussian distributions. The width of the gaussian is chosen to be E_a and E_b for the two types of particles, with $< v_x^2 >=< v_y^2 >= 2E_{a,b}/m_{a,b}$, thus allowing us to control the differential heating at the boundary.

2.3 Spatial temperature ratio profiles with selective differential boundary heating

In Fig.2.2 we show three choices of differential heating: $E_b/E_a = 1$ where equal amounts of energy are fed to two types of particles at the boundaries, $E_b/E_a = 5$ where the energy fed is proportional to the mass ratio as in the vibrational experiments, and $E_b/E_a = 25$ which even more disproportionately emphasizes the heavier particles. Fig.2.2 displays (a) the average temperature ratio $\gamma = T_a(z)/T_b(z)$ and (b) number

density ratio $n_a(z)/n_b(z)$ profiles along the direction perpendicular to the top and bottom boundaries. Comparing any single pair of curves - say the case $E_b/E_a = 5$ - with experimental data [28] we find similar profiles of γ and number density ratio, although the energy-supplying boundaries are fixed and gaussian. In each of the three cases, the value of γ at the boundaries is determined by the heating mechanism, as expected, but changes to a nearly constant value in the bulk. However, taken together, the three cases show clearly that the bulk value of γ depends on the choice of differential heating at the boundary. Thus shows that the value of γ is not an intrinsic property of the pair of particle species and that the effect of the boundary permeates the bulk of the system.

We further check whether the persistence of the boundary condition into the bulk is a finite size effect by doubling the height of the system to $64d$ while holding fixed the total area fraction. The three heating schemes shown in Fig.2.2 are once again employed, and the temperature ratio and number density ratio as a function of z are shown in Fig.2.3. Clearly, the temperature ratio γ is still affected by the value of E_b/E_a specified at the boundary.

We want to call to attention of a relevant study published[38] by Brey and Ruiz-Montero. They simulated a similar two dimensional binary granular mixture with grains heated by thermal boundary only at bottom. Different from our model here, in their system the top is open and particles leaving the heated bottom will finally fall down again under gravitaty. Then they provide differential heating to the two types of particles and measured the kinetic temperature ratio as a distance from the heating bottom. They found that the ratios under different differential heating collapse to some finite value different than 1 at a distance away from the bottom. The ratio slightly changes with height. The reason why in their system differential heating leads to collapsed temperature ratio while in our system this never happens is not clear. One possible reason might be that in their system, in the region where the

21
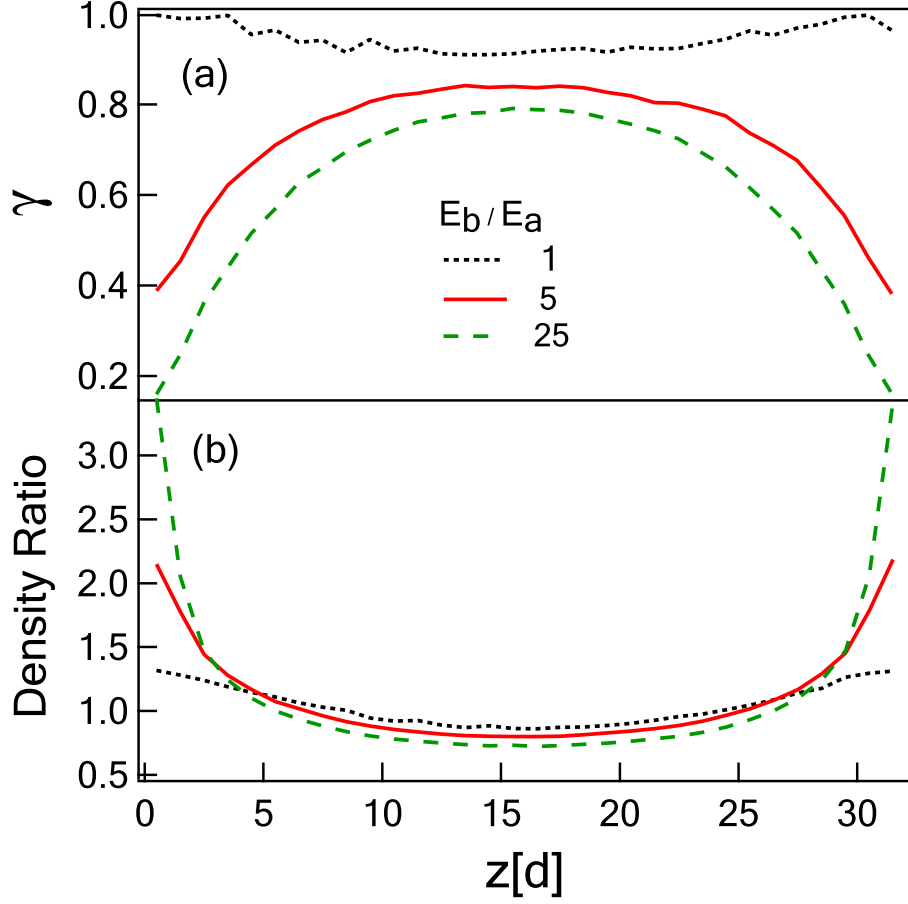
Figure 2.2. (a)Temperature ratio γ profile and (b) number density ratio profile for two species of particles along the vertical (z) direction. The particles differ only in their masses with $m_b = 5m_a$. There are 100 particles of each species in a rectangle of size $48 \times 32d$, corresponding to an area fraction of 10.2%. Three levels of differential heating are shown: $E_a = E_b$(dotted line), $E_a = E_b/5$(solid line), $E_a = E_b/25$(dashed line).
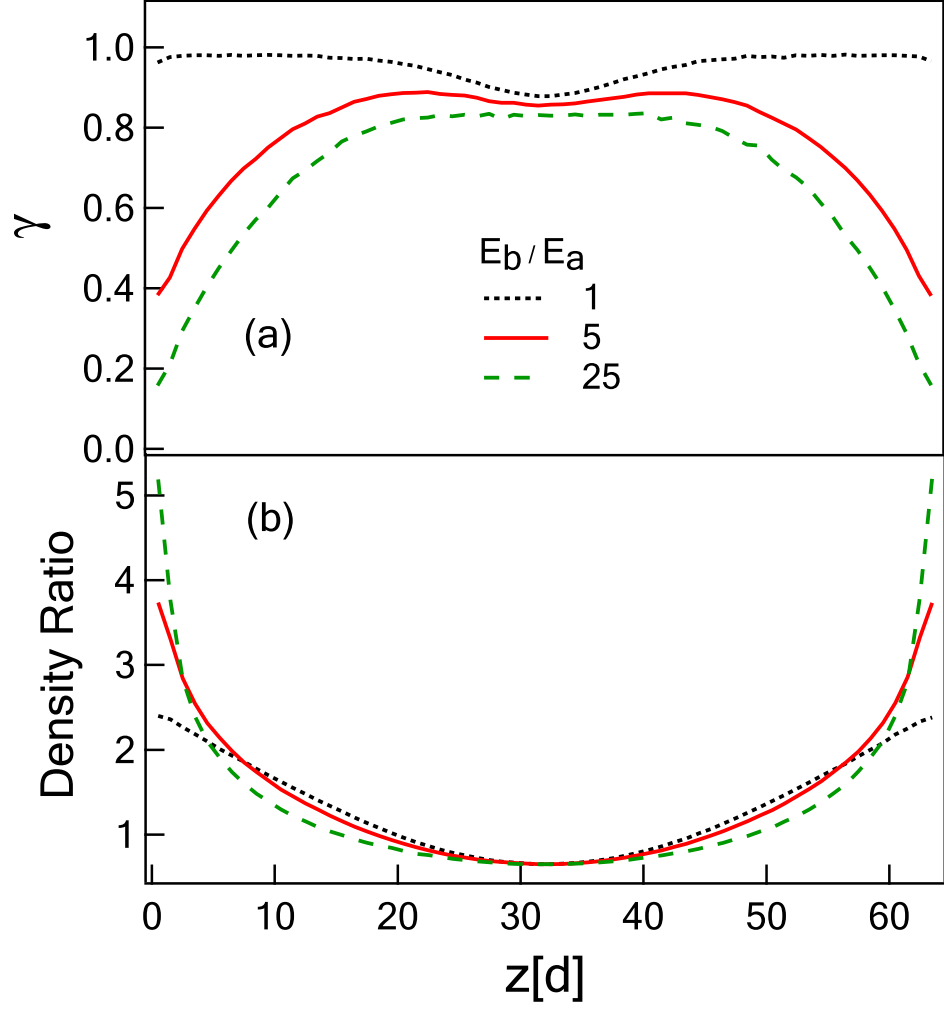
Figure 2.3. Vertical temperature ratio γ profile (a) and density ratio profile (b) in a system of height $64d$, double that of the system in Fig.2.2, with the area fraction maintained at 10.2% The lower panel shows greater segregation of the massive species to the centre of the system than in Fig.2.2.

temperature ratio collapses, the mean free path is big enough where the gravitational energy for a height difference of one mean free path is comparable with the mean kinetic energy. However, in our system, there is no region where the mean free path is very long.

2.4 Temperature ratio as a function of collision times

It is straightforward to simulate substantially taller systems, however, the increasing segregation of the heavier particles to the middle of the system presents a new complication. We thus address the issue of whether the data in Fig.2.2 and 2.3 are still affected by finite-size limitations by considering the number of collisions q suffered by a particle since it has collided with a boundary. Each time a particle i collides with another particle, q_i is incremented by 1, and after it collides with either heating boundary, q_i is set to zero. The probability distribution of the vertical distance l of a particle from the wall it last collided with, is shown in the inset of Fig.2.4 for various values of q. As expected, P(l) broadens and shifts monotonically to larger l, for larger q, saturating at the half-height of the system $16d$ for large q. Next, statistics for the kinetic energy of the two types of particles as a function of q are sampled at fixed time intervals during a long simulation time and the temperature ratio γ is obtained as a function of q. As shown in Fig.2.4, each curve of $\gamma(q)$ reaches a plateau after a small number of collisions. This is consistent with MD simulations of bidisperse systems[32] where it was found that after about 10 collisions the temperature ratio γ reached a steady-state value from arbitrary initial conditions. However, as can be seen in Fig.2.4 the asymptotic value of γ at large q remains a function of E_b/E_a. Therefore, details of the driving mechanism at the boundary appear not to be erased by inter-particle collisions. To ensure that this conclusion is not dominated by particles that suffered many collisions but happened to remain close to a boundary, we also plot in Fig.2.4 γ for the subset of particle trajectories that start at one heating
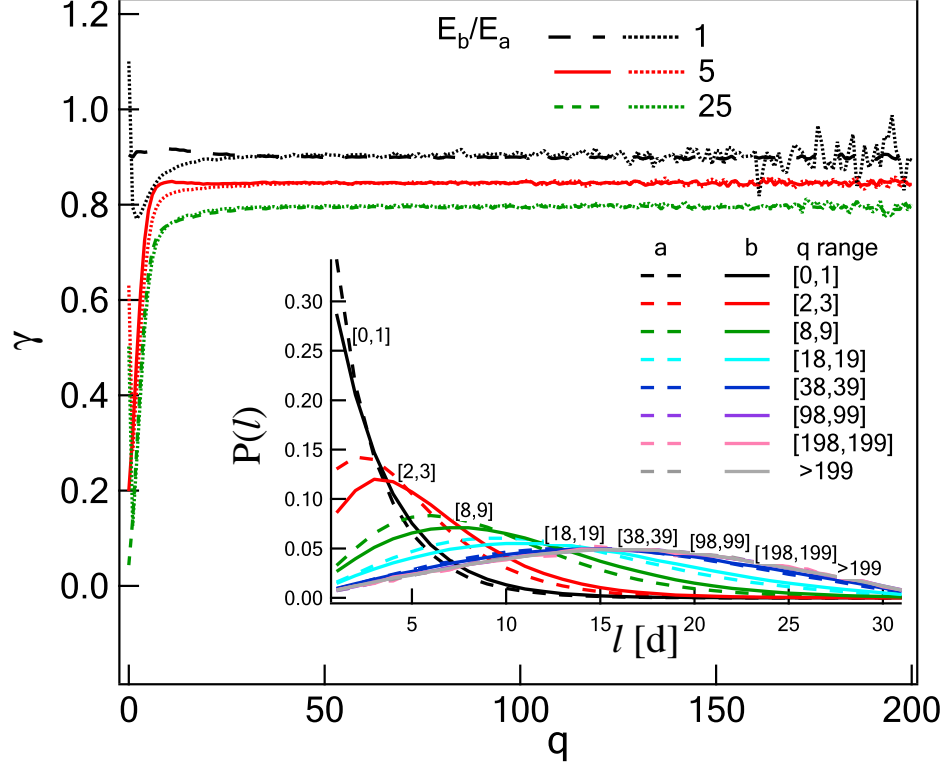
Figure 2.4. The temperature ratio, γ, as a function of collision number, q, under three levels of differential heating. The corresponding dotted curves sample only those trajectories that start at one heating wall and terminate at the other. The inset plots the distribution of the distance from the last heating boundary l for different ranges of q.

wall and terminate at the other. The plateau values of γ of these trajectories coincide with those from the entire set of particles.

2.5   Numerical and stochastic model

It may still be argued that a finite-size effect persists since particles with large q suffer collisions with particles that have recently collided with the boundary. In order to further confirm the persistent effect of the differential heating mechanism we turn to a numerical model without spatial degrees of freedom, based on that introduced by van Zon and MacKintosh[39] to simulate a monodisperse system. For a monodisperse system, van Zon and MacKintosh find that the shape of particle

velocity distribution strongly depends on the relative frequency of boundary heating events and inter-particle collision events. We adopt this model to include 2N inelastic particles initialized with gaussian-distributed initial velocities. In each time step, C pairs of particles are randomly selected to collide in a 2-dimensional inelastic collision, and H particles are selected for heating. The impact parameters for the collisions are chosen from a uniform random distribution. For each heating event, velocities are selected randomly from Gaussian distributions with average energy E_a and E_b, depending on the species of particle selected. Once again, the three cases of differential heating used in the spatial event-driven simulations can also be implemented here. For each of these three cases, statistics for the temperature ratio γ are accrued for many values of $q_{avg} = 2C/H$, the ratio of the frequency of collisions to heating events. (The large q_{avg} limit corresponds to a boundary driven system in which the inter-particle collisions are much more frequent than heating events, and corresponds to large q in Fig.2.4, without the complications introduced by spatial gradients). As shown by the three sets of data symbols in Fig.2.5, the temperature ratio γ as a function of q_{avg} is different for the three heating mechanisms even for large q_{avg}, where the heating events are rare relative to the collisions that one might intuitively expect to erase details of the heating mechanism.

The numerical model discussed above can be described in terms of an exactly solvable stochastic model [40] in which a dissipative system is coupled with a heat bath. We have adapted the model of Shokef and Levine[40] to incorporate equal numbers of two types of particles a and b. The time evolution of the energy $E^i(t)$ of a particle i of either species during an infinitesimal time step dt is expressed by a stochastic equation,

$$
E^i(t+dt) = \begin{cases} \text{value:} & \text{probability:} \\[2mm] E^i(t), & 1 - \mathrm{P}dt, \\[6mm] E^i(t) + \frac{\lambda_{ij}(1+\eta)^2}{2(1+\lambda_{ij})^2}E^j(t)- \\ \frac{2(1+\eta)\lambda_{ij}+1-\eta^2}{2(1+\lambda_{ij})^2}E^i(t)+ \\ (\frac{1+\eta^2}{4}+\frac{1}{2})E^i(t), & (1-f)\mathrm{P}dt, \\[8mm] E^i_a \ or \ E^i_b, & f\mathrm{P}dt, \end{cases} \tag{2.1}
$$

where $E^{i(j)}(t)$ is the instantaneous energy of the particle $i(j)$ at time t, P is the interaction rate per particle per unit time, f is the fraction selected for external heating, $\lambda_{ij} = m_i/m_j$, η is the restitution coefficient, $E^i_{a,b}$ is the external energy given to particle i for a heating event with an input energy E^i_a or E^i_b depending on the species of particle i. Therefore, the first line on the RHS of Eq.2.1 corresponds to particle i not undergoing interaction, the second line corresponds to particle i being selected for collision with another particle j (averaged over collisions with species a and b) and the third line corresponds to particle i being selected for heating. We use a simple model of head-on collisions (where the relative velocity of the two particles is parallel to the line joining their centers at contact) with uncorrelated pre-collisional velocities. In steady state, the ensemble averages obey $< E^i(t+dt) > = < E^i(t) >$. By solving this stochastic equation, we determine the dependence of the temperature ratio γ on q_{avg} as shown in Fig.2.5. To make comparison to the numerical simulations of the random heating model, we make the correspondence $f = H/(H+2C) = 1/(1+q_{avg})$. Once again, three different values of E_b/E_a are shown. Despite the simplified treatment of collisions within our adaptation of the Shokef-Levine model, we obtain reasonable agreement between the numerical model and this stochastic model. Qualitatively, the
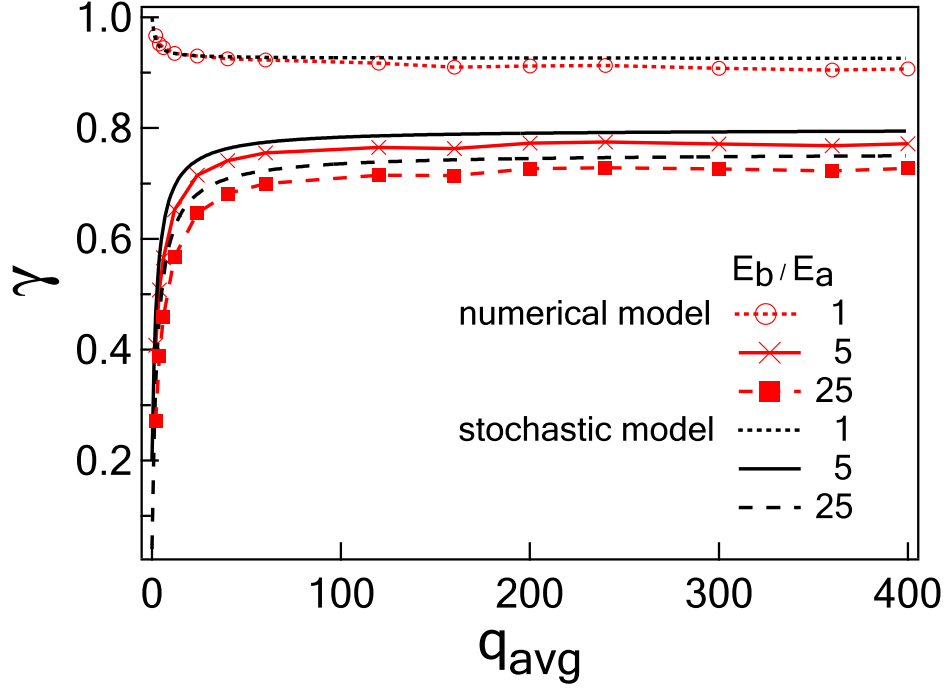
Figure 2.5. The temperature ratio γ as a function of the average particle-particle collision times q_{avg}. Numerical model results are expressed in lines with symbols, $E_a = E_b$(open circle), $E_a = E_b/5$(cross), $E_a = E_b/25$(solid square). The smooth curves correspond to results derived from the stochastic model, $E_a = E_b$(dotted line), $E_a = E_b/5$(solid line), $E_a = E_b/25$(dashed line). The corresponding asymptotic values as $q_{avg} \to \infty$ for these curves are 0.926, 0.798 and 0.755.

dependence on E_b/E_a follows the same trend, and the smooth curves in Fig.2.5 for the three heating conditions do not converge at large q_{avg}.

2.6 Summary and discussion

In summary, we have demonstrated by three independent means, the persistent effect of the boundary heating mechanism on the extent of non-equipartition in a binary granular system. The specific context for studying the effect of differential heating come from studies of vibration-fluidized granular systems, however, this type of differential heating should be generic to other forms of driving: in shear, for example, particles will be differentially excited depending on their frictional properties, shape, or size relative to the features of the shearing surface. Similar effects

may be anticipated even in monodisperse systems where the equipartition between rotational and translational degrees of freedom may not be determined purely by particle properties but by the degree to which each degree of freedom is pumped by the driving mechanism. More generally, details of the boundary heating mechanism can not be ignored in describing inelastic gases, leading to concerns about quantitative comparisons between theories of homogeneously excited granular systems and boundary-driven experiments.

CHAPTER 3

KINEMATICS OF 3D VIBRATION FLUIDIZED GRANULAR GASES

In this Chapter we present details of an experimental study of a vibration-fluidized 3D granular system. We track full field motion of particles in a thin laser-illuminated plane in the bulk of a 3D volume by high speed video imaging and image analysis methods. Temperature profiles and velocity distributions at different volume fractions are measured and compared with available kinetic theory.

3.1 Introduction

Experimental studies of three-dimensional steady state granular systems are much rarer than studies of 2D systems due to the challenges of tracking particles by direct imaging in the interior of a 3D volume. Instead, other physical probes of the ensemble properties of granular particles are utilized to provide indirect noninvasive experimental study of a 3D granular system, such as capacitance[41], magnetic resonance imaging[42], diffusing-wave spectroscopy[43], and mutual inductance[44]. Two recently developed experimental techniques are positron emission tracking [15, 45, 46] of tracer particles(PEPT), and nuclear magnetic resonance imaging(NMR) [16, 47, 48]. These two recent studies focused on the study of kinetic quantities in the dilute regime, including spatial profiles of temperature and number density, although volume fraction up to 0.45 is reported in the NMR experiments[48]. A non-Gaussian velocity distribution was reported in[48].

The PEPT method provides a pseudo-full-field measurement of kinetic temperature and number density profiles in a vibration fluidized granular medium. A tracer

particle is first created by irradiating a glass sphere with ^{3}He. This particle is physically indistinguishable from other beads in the experimental cell, except that the radionuclide decays by positron emission. A positron quickly annihilates with an electron and produce a pair back-to-back gamma rays that detected by diametrically placed positron sensitive gamma ray camera heads. A line close to the point of emission is then determined. Through successful location events, the position of the tracer particle can be located in three dimensions. The authors reported a spatial resolution up to ± 1mm at grain speeds of about 1m/s[15], with the diameter of beads about 5mm. Under the assumption of ergodicity, the spatial granular temperature and number density profiles can be determined.

In the NMR experiments[48], a small number of mustard seeds are confined in a cylindrical sample tube and driven by vertical vibration. Pulsed field gradient(PFG) and magnetic resonance imaging(MRI) signals are acquired that reflect the position and motion of the propagator, i.e. ensemble average of collective mustard seeds. The number density, displacements and root mean square displacements are obtained to provide spatial profiles of granular temperature and number density.

Compared with the above techniques, high speed video imaging method has advantage of being able to get full-field tracking of individual particles. We would like to benefit from the development of high speed digital cameras, fast computer and image analysis software to build statistics of particle movements in the view field. The success of this technique has been fully demonstrated in two dimensions, especially in the dilute regime[22]. The study in a three dimensional space is quite immature, compared with its two dimensional counterpart. The only previous attempt we are aware of is by Feitosa, in our research group[22].

Here we report on an experimental study of a vibration-fluidized granular gas by high speed imaging methods. New particle locating methods are developed to track particles at different depths inside the 3D volume. We focus on measurements

of velocity distributions, which have not been studied in much details in previous experiments.

3.2 Experimental method

The experimental data acquisition composed of two steps: how to image particles and how to track particles. We describe the experimental setup in 3.2.1 and particle tracking technique in 3.2.2.

3.2.1 Experimental apparatus

As shown in Fig.3.1, a cubical cell made with acrylic plates is mounted on an electromechanical shaker (Ling Dynamics V456) which vibrates vertically to drive granular particles confined in the cell. Shaking of the vibrator is controlled by a wave function generator. We choose sinusoidal driving with the vibration frequency ranging from 50Hz to 80Hz, velocity amplitudes V_0 from 2.3 m/s to 3.7 m/s, and accelerations from $90g$ to $190g$. These driving conditions ensure full fluidization of the granular system as no apparent clustering observed.

The size of the cell is 51.2mm or $\approx 32d$ each side, with d the diameter of a sphere. Two laser sheets produced by expanding beams from laser diodes (Thorlabs ML101J8) with a cylindrical lens travel through the cell from two sides to illuminate particles passing through the thin sheet. The thickness of the sheet in the y-direction is $\approx 1d$, and its y-position can be varied, allowing us to study particle motions in x-z planes at varying depth from the front wall. The light path is illustrated in Fig.3.3. A real photograph of the experimental set up is given in Fig.3.2.

We use Delrin spheres, purchased from McMaster-Carr, of diameter $d = 1.560 \pm 0.003$mm. The advantage of Delrin particles is that any incident light is scattered over the whole volume of the particle, thus making it optically uniform even if it is unevenly illuminated. The average normal coefficient of restitution is $\varepsilon = 0.92 \pm$
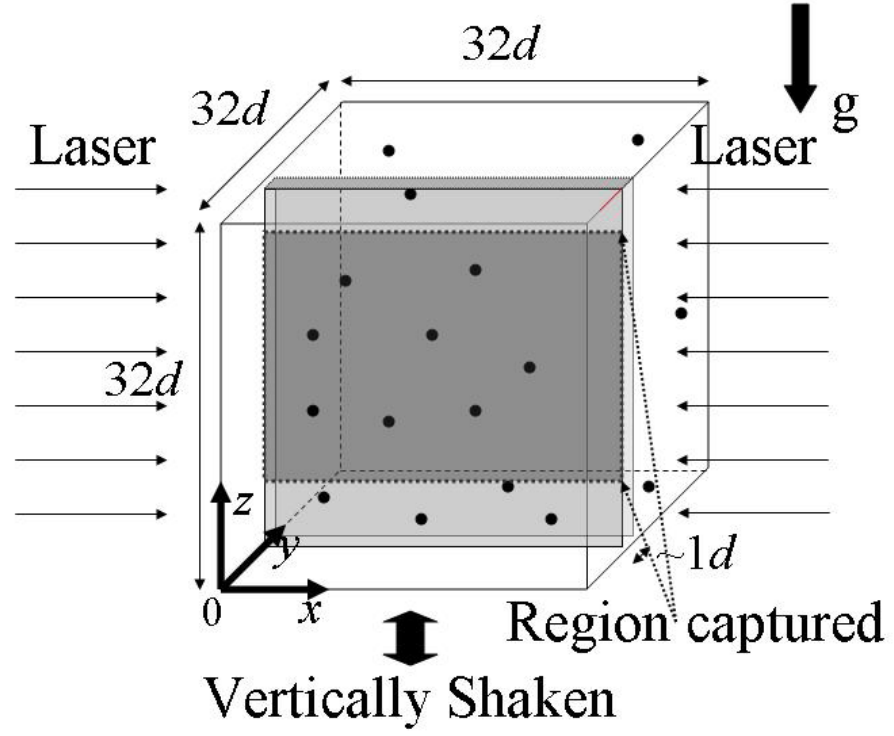
Figure 3.1. Sketch of the 3D granular system under study. Delrin particles are confined in a cubical acrylic box which is driven vertically by a shaker. The shaded rectangle is a pseudo-two-dimensional plane with the thickness in the third direction $1d$ illuminated by laser sheets from both sides. The darker shading shows the area imaged by the camera.
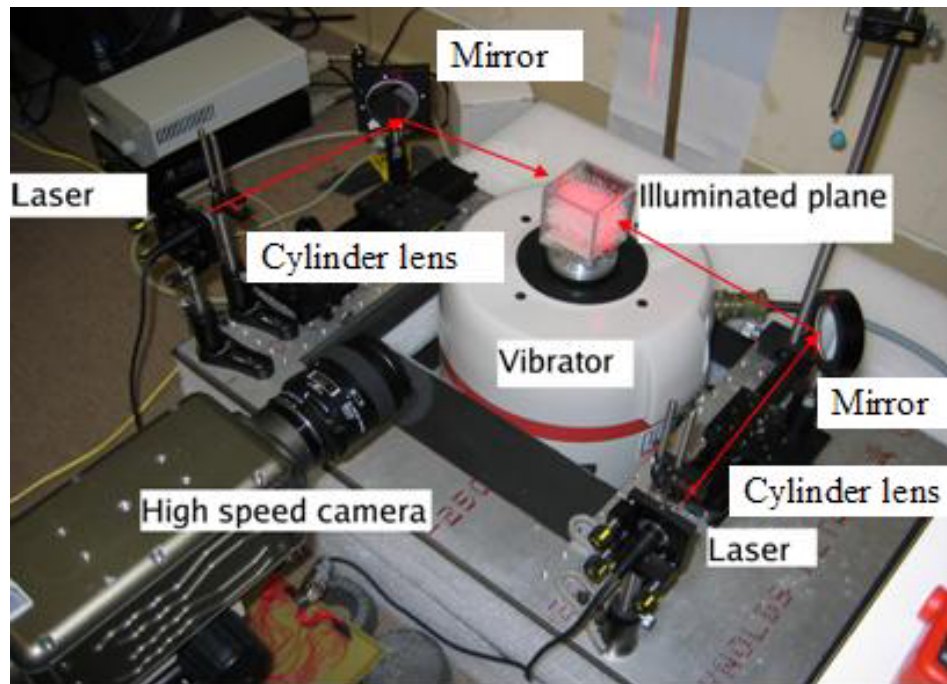
Figure 3.2. A photograph of the real experimental set up.
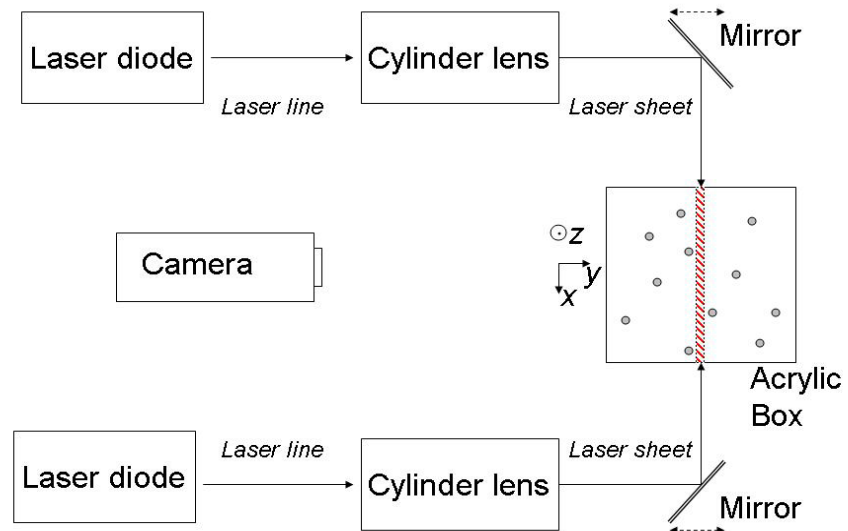
Figure 3.3. Light path for the experimental illumination.
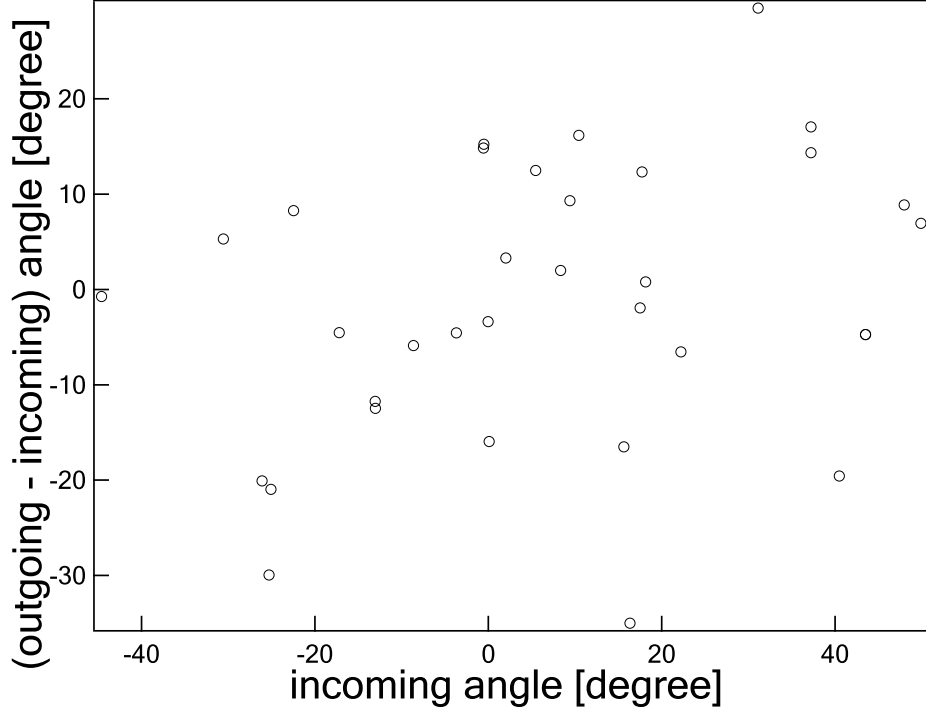
Figure 3.4. Outgoing angle minus incidence incoming angle for bounces at rough glass surface. Particles are randomly scattered with different angles.

0.21, experimentally measured from hand picked particle-particle collisions, i.e. by measuring the ratio of the relative normal velocities before and after a collision for each of these collisions. The error bar reflects the dependence of ε on impact parameter, relative particle velocity, and spin.

The bottom and top walls are rough glass plates that provide a low-inelasticity surface but also randomize the direction of collisional momentum transfer. This helps suppress small, but persistent collective motions of particles in the cell. To check the randomizing effect we carefully measure the incoming and outgoing angle of a few particle-bottom collisions and show the results in Fig.3.4. These rough plates provide effective randomizing as for the same impact angle the outgoing angle is widely scattered. The r.m.s vertical roughness of the surface is about 0.1d, and the lateral scale of the roughness is about 1d.

A Phantom v7 camera images the x-z plane selected by the light sheet, at 5,000 frames/second, with a resolution of 640×480 pixels. The field of view is a rectangle of width $\approx 30d$ and height $20d$, centered on the middle of the cell.

3.2.2 Particle tracking

Generally speaking, there are two technical procedures before we can study the kinematics of a granular gas: yielding the positions of particles in each image and binding particles in consecutive images to generate individual tracks for each particle. The difficulty of yielding positions of particles here stems from two distinct eclipsing effects. First, spheres in the middle of the cell are of less chances to be illuminated because the light path is obstructed by spheres close to the sides. For individual illuminated Delrin spheres any laser light incident on it is scattered through its volume which makes the illumination homogeneously saturated over the volume. But, as long as the laser sheet is at some depth away from the front plane, illuminated spheres can be partially eclipsed by other spheres in the front. A video frame with examples of partially eclipsed particles is shown in Fig.3.5. Actually, in a typical experimental image, most spheres are eclipsed more or less. These two eclipsing effects are strongly affected by the depth of laser sheet and the volume fraction of particles. And, it is often that spheres physically located in the illuminated plane are not illuminated or mostly eclipsed that they are impossible to be located. We give up to locate these spheres and ensure the correctness and accuracy of all the located spheres in our analysis. As a result, we focus on velocity statistics rather than number density distributions since the detection probability of a particle depends on these two effects. We will show later that unable to track all the particles physically in the illuminated plane will not bias our sampling of kinematics.

Single particle tracking is a long topic with applications in many scientific and engineering fields. Algorithms for general particle tracking include cross-correlation of
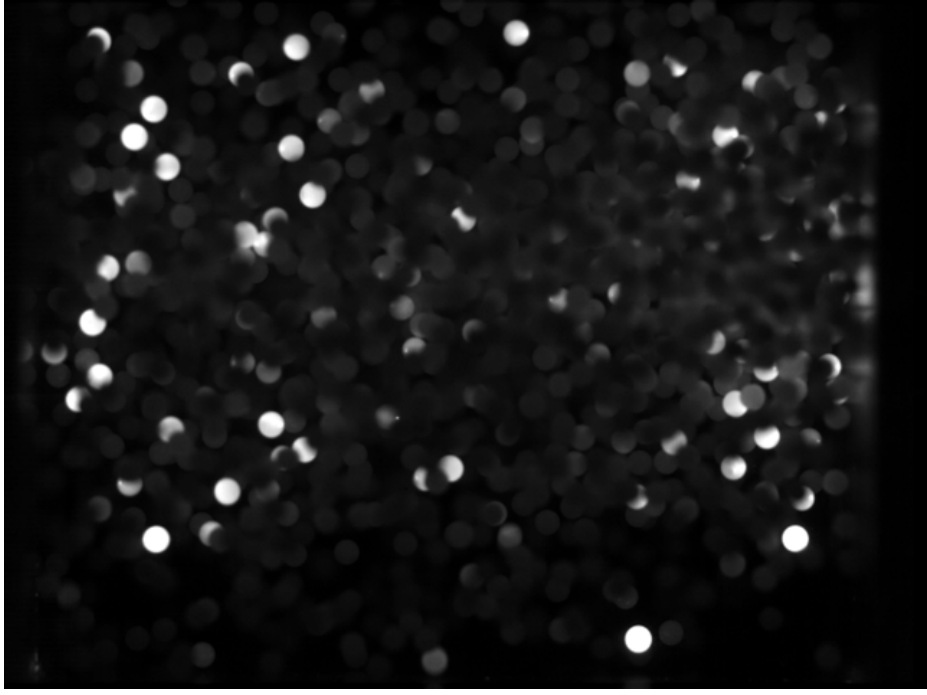
Figure 3.5. A real experimental image at about 8d behind the front plate with the laser illumination on, illustrating the two eclipsing effects.

subsequent images, calculating the center of mass(centroid) of the feature objects, and directly fitting Gaussian or other masks to the intensity field[49] etc. Unfortunately, none of these methods works for our system. The particles in our system are eclipsed spheres. The shape of the exposed part is unpredictable and under continuous change in any image sequences. All the above general particle tracking methods need a relatively stable shape of the feature objects to provide accurate tracking.

For circular detection, the Circle Hough Transform(CHT) method is most commonly used. This method allows part of the circles to be blocked. But there are some other complex issues if applying this method in our image. The immediate problem is locating spheres in front of the illuminated plane due to the projected circular edge on the eclipsed illuminated spheres, i.e. these concave edges produced by eclipsing. Consequently we might get two sphere locations very close to each other. This not only introduces spheres that are out of the illumination plane to our data, but also

causes serious problems in the further tracking steps as we need particles to be well distinguished in consecutive images to build individual tracks for each particle while particles too close to each other makes it to be hard or even impossible.

Instead of these traditional methods, we introduce a new method that isolates the convex parts of the illuminated edge of spheres to locate their centers to sub-pixel precision. The algorithm details can be found in the IDL routines in the appendix of this dissertation. The edges are circular arcs of known radius. Those more complex edges due to heavy eclipsing will be automatically discarded by a cut-off threshold. We first detect all the sharp edges (Fig.3.6b) in the image by a Sobel operator[50] as shown in the sample image Fig.3.6a. Then, a threshold value is selected as the starting points to plot rays from these edge points in the direction of the local intensity gradient drawn pixel by pixel as shown on the image. A fast algorithm to plot these lines is the Bresenham's algorithm. The local intensity gradient is obtained by applying a Gaussian gradient filter. For points belonging to the convex illuminated edges, these rays converge to the center of the sphere, while concave edges produce rays that diverge (Fig.3.6c). Third, local maxima for accumulations of rays (Fig.3.6d) above a cut-off value are picked up as candidates for particle centers; objects with an insufficient length of illuminated perimeter are rejected. By this threshold cut off, we not only can pick up spheres that are to be located at good resolution, but also discard those features that can give us wrong or inaccurate locations due to insufficient edges exposed. Finally, particle centers are determined with sub-pixel resolution by minimizing the squared distance to the gradient rays. In short, suppose the center is at (x, y), d_i is the distance of point (x, y) to the ray line i. Define a function $f = \sum_i d_i^2$. We can find sub-pixel (x,y) by minimizing the function f.
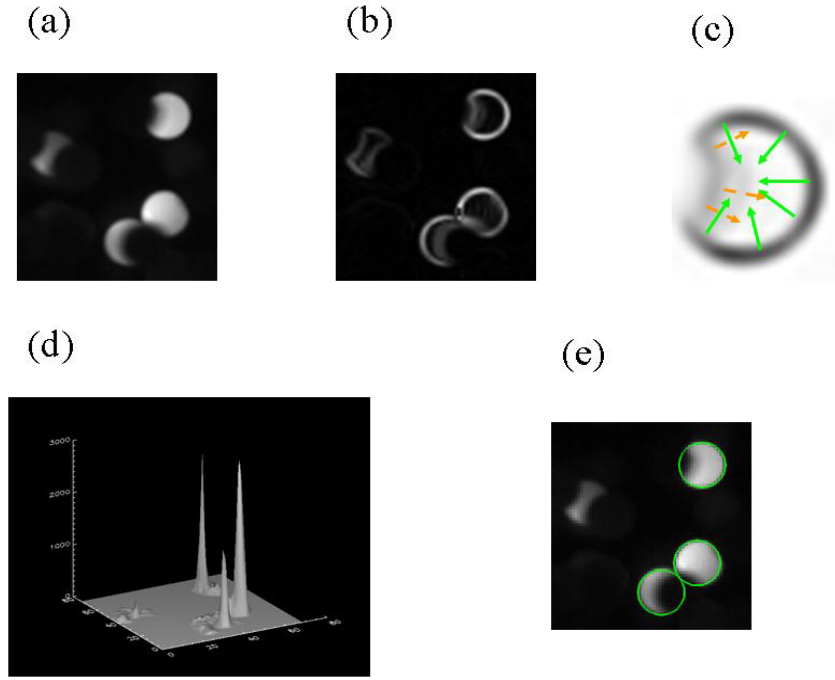
Figure 3.6. (a) Part of a video frame. (b) Edge detection performed on this frame. (c) Illustration of the rays emanating from the edge, along the intensity gradient, for the top right particle in (a). The solid rays converge toward the center and dashed rays diverge. (d) Plot of values for all the accumulated gradient rays. (e) Located particle positions. For the value of the threshold applied to the peaks in (d), the fourth particle in the frame is not located.
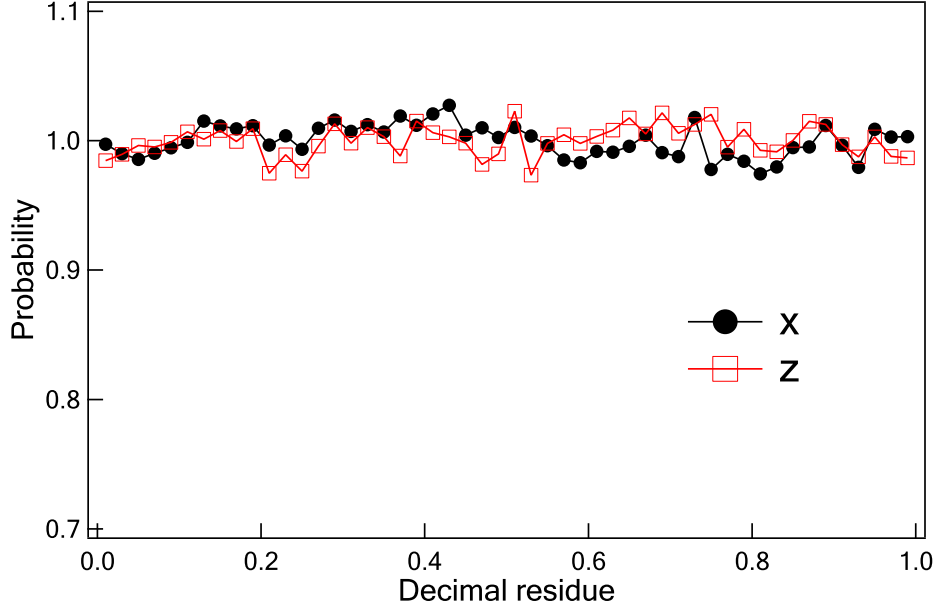
Figure 3.7. Decimal residue distribution for all the particles located in a set of raw video frames.

3.2.3 Test of systematic error

We need to check the performance of this new particle locating algorithm and ensure that it will not lead to systematic bias. The first to check is the distribution of the sub-pixel part of the particle locations we get. We call this part the decimal residue. This residue is required to satisfy a homogeneous distribution as the physical locations of particles should be random. We analyze data from a set of video frames, i.e. about 10,000 frames, and find that this distribution is indeed flat as shown in Fig.3.7. Therefore, there is no tendency for the sub-pixel part to bias toward any region between 0 and 1.

The determination of particle positions depends on the eclipsing effect. Since particles moving in the front affects the length of edges exposed and the locating of the particle, we test the dependence of the accuracy of the algorithm on the eclipsing by gradually covering a sampling particle by another blocking particle artificially. The test particle is got by picking up a completely exposed particle from a real experimental image. The blocking particle is a computer generated black disk(with

zero brightness) with the same rounded diameter with the sampling particle. We can gradually approach these two particles from different angles and make parts of the edge of the test particle blocked. Results from different directions are averaged finally to get the dependence only on distance. Actually, by setting a reasonable exposure time of the high speed camera, we can not see noticeable difference for approaching from different angles.

The position of the test particle is first obtained by the standard mass centroid method[17]. As we gradually blocking this test particle, its position is located by our new algorithm. The distance δr between these two positions, i.e. the uncovered center and the new blocked center, is plotted as a function of the overlapping length l as shown in Fig.3.8. We can see that as the overlap length close to the diameter of the particle, corresponding to about 50% of the circumference is blocked, the difference of the two locations is still kept at about 0.2 pixel, about 1% of the diameter.

The particles picked out from the cumulative gradient rays image(Fig.3.6(d)) depends on the peak cumulative gradient ray value. In principle, the peak cumulative gradient ray value of a particle depends on brightness of illumination and the length of edge exposed. We needs to select a cut-off value to select particles. The number of particles we get from an image depends on this cut-off value. As we increase this cut-off value, we might loose particles that are physically located in the plane. Actually, we should set this cut-off value at an proper range. This value should not be too low, otherwise, we might get fake identifications. If this value is too high, we get poor statistics, as only few particles can be picked out. We must also ensure that our sampling velocity is not biased by this cut-off value.

We measured the average peak cumulative gradient ray value as a function of particle velocity in Fig.3.9. The graph illustrates that the peak value is pretty insensitive to particle velocity. In addition, we measured the velocity distribution with two different cumulative cut-off value. With the lower value 500, we already can not
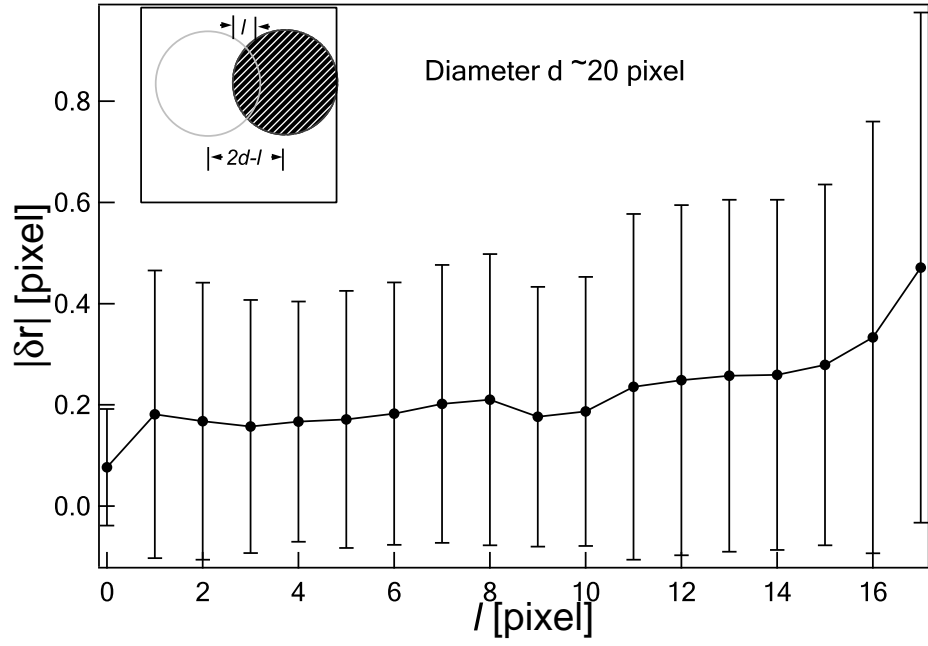
Figure 3.8. Deviations for particle centers as the test particle is gradually blocked by another particle compared with the test particle without blocking. When there is no blocking, the center is located by standard mass centroid method. The diameter of the particle is about 20 pixel. The data is averaged for ten cases with different test particles.
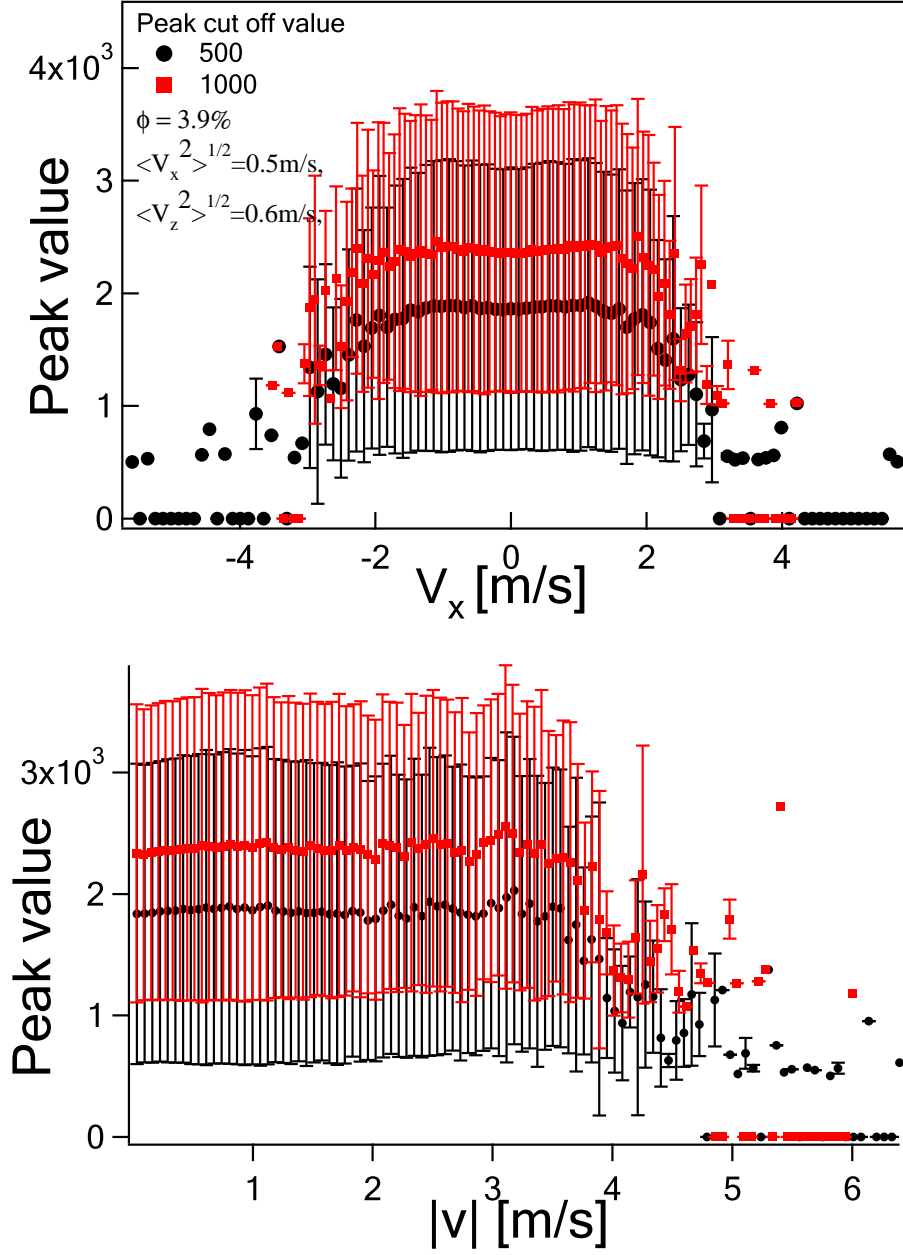
Figure 3.9. Peak values of the cumulative gradient rays as a function of particle velocity. The volume fraction is 3.9% and the threshold peak value for particle selection is 500 and 1000. Root mean square value of horizontal velocity and vertical velocity is about 0.5m/s and 0.6m/s. An error bar is also appended for each curve.
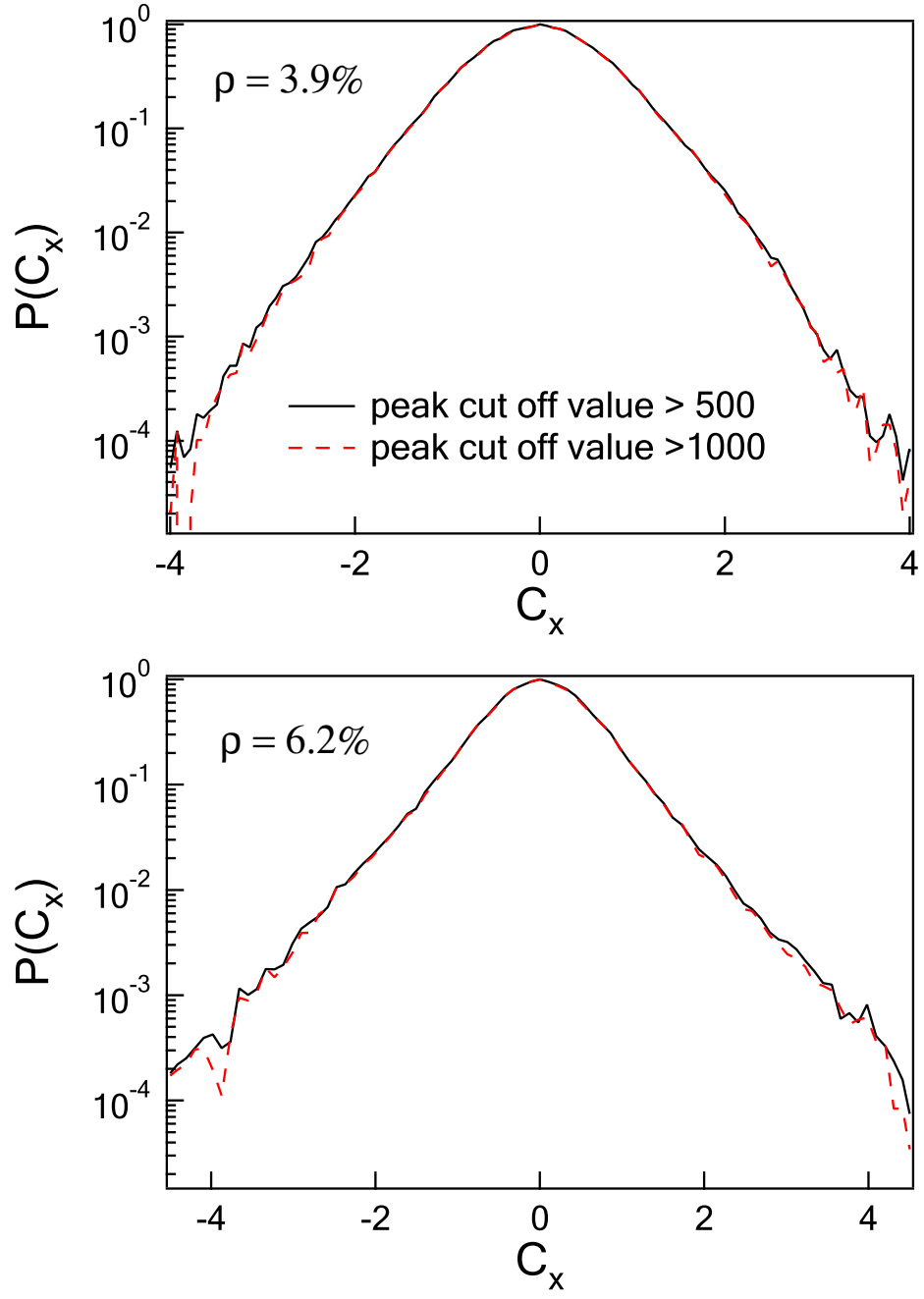
Figure 3.10. $P(c_x)$ at two different volume fractions with the cumulative cut-off value set at 500 and 1000, leading to the detected number of particles changing by 32% for ϕ=3.9% and 44% for ϕ=6.1%.

observe any fake particles for a test video of about 200 frames, where for the higher value, we are still able to get good data statistics. We find that the velocity distributions collapse at these two different cut-off values as shown in Fig.3.10. This is strong evidence that the measured velocity distribution is not subject to a systematic error from blocking and eclipsing of light.

To more directly verify that our sampling is not systematically biased by the eclipsing and blocking effects, we have carried out event-driven molecular simulations of discs in a 2D box with dimension 48d x 32d, and number of particles $N = 200$ with elastic coefficient 0.93. The system is heated by thermal bath at $y = 0$ and $y = 32d$. The particles are sampled in a strip between the height $8d < y < 9d$, which is intended to represent the width of the sheet illumination. The cross-section of particles in this strip are projected to $y = 0$ with projections blocked by other eclipsing particles at $y > 0$. We compared three data sets for the velocity distribution v_x, 1)all particles in the strip 2) particles that are less than 50% eclipsed, and 3) particles that are less than 20% eclipsed. It is shown in Fig.3.11 that the velocity distribution is the same for these three cases. This is more direct confirmation that eclipsing does not have a systematic effect on velocity distribution.

Finally, the analyzed result for the example image shown in Fig.3.5 using our algorithm is shown in Fig.3.12. Green circles are centered around particles located out. After locating particles from individual frames, we can build continuous tracks for a whole set of video frames for further data analysis.

3.3 Temperature profiles

The kinetic temperature $T = \frac{1}{2}(\langle v_x^2 \rangle + \langle v_z^2 \rangle)$ is measured at several depths, y, between the front plane and a little beyond the middle of the cell. As shown in Fig.3.13 (top row), in any given x-z plane, T is higher near the top and bottom wall, and lower in the middle. Comparing x-z planes at different depths y, we see that T
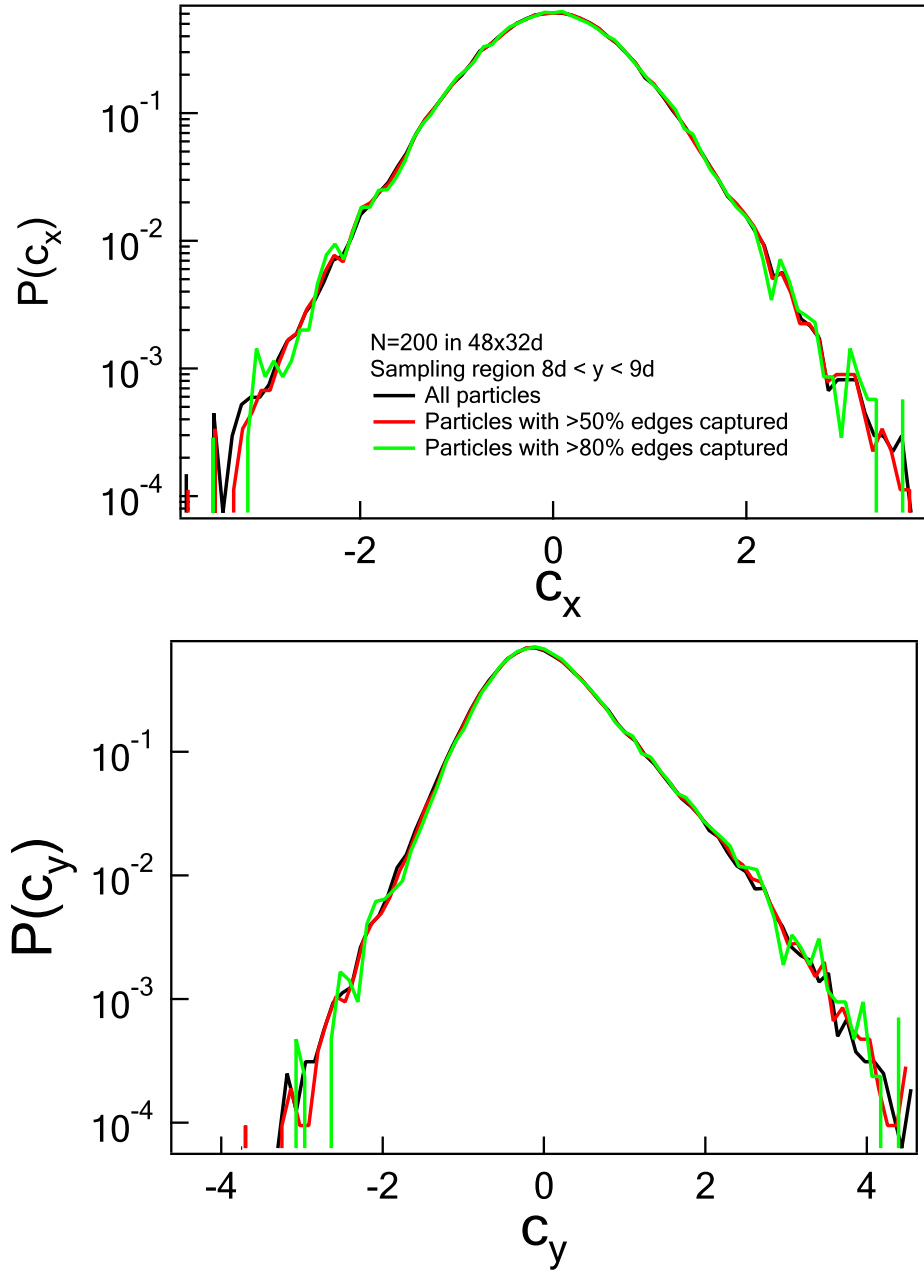
Figure 3.11. $P(c_x)$ and $P(c_y)$ for particles inside a strip in a 2-dimensional boundary heating system by event-driven molecular dynamics simulation. Black curve: all particles in the strip; red curve: particles in the strip with more than 50% edge projected to the bottom; green curve: particles in the strip with more than 80% edge projected to the bottom..
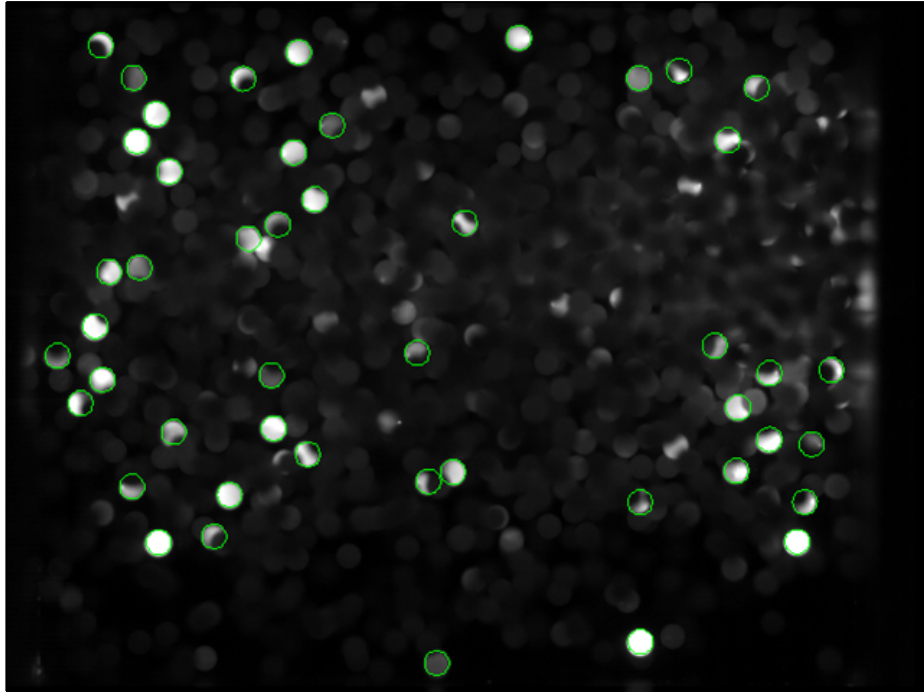
Figure 3.12. An example image of the 3D fluidized granular medium at about $y = 8d$, i.e. 8 diameter from the front plate. Green circles are centered at captured particles.
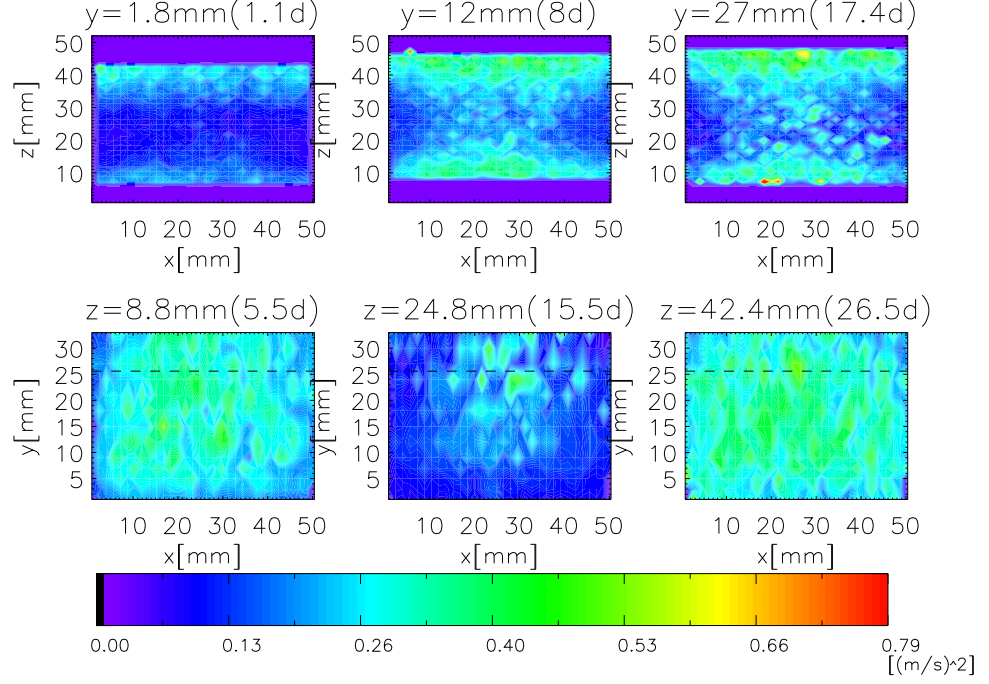
Figure 3.13. Distribution of the kinetic temperature at planes of various y(top row) and z(lower row). The driving frequency is 60Hz, $\Gamma = 110g$ and volume fraction 5.1%. (Refer Fig.3.1 for the coordinate definition.)

goes up in the middle of the cell comparing with that close to the front boundary, revealing the dissipative effect of the front vertical wall. The data are then reorganized to show $T(x,y)$ at a few heights, z (Fig.3.13 bottom row). Within each plane, T is lower close to the vertical walls, due to the dissipation at the walls. The length scale over which the wall dissipation manifests itself is comparable to the mean free path, and grows at lower ϕ.

3.4   Distribution of velocity

The distribution of particle velocities is a fundamental descriptor of the statistics of a particulate system. We know that a granular gas is inelastic - particles interact by dissipative contact forces, with the energy lost by collisions being compensated by a driving mechanism to keep the system in a steady state. Since the inelastic gas is both of fundamental interest and closely related to technologically important

granular media, it has been the subject of much recent experimental, simulation and theoretical activity[51].

Inelastic steady states may be broadly divided into systems driven from the boundaries and those that are driven homogeneously in the bulk. Homogeneously heated granular gases are represented theoretically by inelastically colliding particles energized by random, spatially homogeneous, uncorrelated boosts of energy between collisions. It has been shown [52] that the high-velocity tail of the velocity distribution for this model is of the form $P(c) \propto \exp(-Ac^{3/2})$ where $c = v/\sigma$ is a velocity component, v normalized by its r.m.s value σ. The velocity distribution for low velocities was computed by finding perturbative solutions to the Boltzmann equation in an expansion in Sonine polynomials around a Gaussian [52, 53]. In both limits, the results depend on inelasticity but not on volume fraction, ϕ. These results have been confirmed by simulation[54, 55, 56]. Simulations show [33, 39, 57, 58, 59] that the velocity distribution evolves continuously from a nearly-Gaussian distribution to $f(c) \sim exp(-Ac^{\beta})$ depending on mechanical properties of particles and external driving. There are no direct predictions for boundary-driven systems, but models [39, 60] which vary q, the ratio of the frequency of particle collisions to the frequency of heating events, give some intuition on the passage from the homogeneously heated ($q \approx 1$) to the boundary-driven ($q \gg 1$) case.

The closest experimental analogues for this model are 2D monolayers of particles fluidized by a vibrated base[27] where velocity distributions depend strongly on the nature of the base[61]; for a sufficiently rough base [62], the Sonine expansion describes the distribution satisfactorily. There are no 3D realizations of the homogeneously heated granular gas with random forcing in the bulk of the medium. Actually, most experiments of inelastic gases have focused on 2-dimensional (2D) systems driven at boundary. Rouyer[14] and Kudrolli[63] have studied 2D systems driven by vibration. Aranson[64] studied an electrostatic driving 2D system. Experiments by Rouyer[14]

and Aranson[64]show the entire distribution of velocity fluctuations can be described by the functional form $P(c) \propto exp(-Ac^{\beta})$ with $\beta \approx \frac{3}{2}$ over a broad range of number density and inelasticity. However, the relationship of these experimental results to the prediction of [52] are unclear. Simulations of the homogeneously heated gas [65] show that the asymptotic high-velocity behavior only sets in extremely deep in the tail, too rare to be experimentally detectable. Furthermore, the measured distribution differs between experiments, possibly because these quasi-2D experiments are sensitive to the specifics of the confinement in the thin dimension [14, 66, 67] or to the substrate on which they move [63].

We now turn to the entire distribution of the velocity fluctuations. The velocity fluctuations are anisotropic due to the energy flux from boundary; we concentrate on v_x, the horizontal component, perpendicular to the driving direction. The distribution $P(c_x)$ of c_x, the normalized horizontal velocity $c_x = v_x/(2T_x)^{1/2}$ where $T_x = \langle v_x^2 \rangle$, shows weak dependence on position very close to the walls of the cell (as also seen in simulations [33, 57]). Therefore, we report data at $y = 8d$ which is far from the front wall, and yet not so deep in the cell where the velocity statistics are greatly diminished by eclipsing effects.

Our sampling window is about $30 \times 20d$. We divide it into seven equally spaced stripes with increasing x and z. The velocity distributions at different x strip and z strip are shown at Fig.3.14 and Fig.3.15. We can find although the kinetic temperature changed by up to a factor of 2(as seen in Fig.3.13, $P(c_x)$ remains almost the same at these different x and z positions. And the distributions agree with $P(c_x)$ sampled over the whole area.

The dependence of $P(c_x)$ on different driving frequencies and amplitude is shown in Fig.3.16. As the overall temperature is changed by a factor of 3, we observe no systematic changes in $P(c_x)$. In experiments on 2D monolayers [61, 62] it was noted that velocity distribution depended on the smoothness of the driving surface, as might
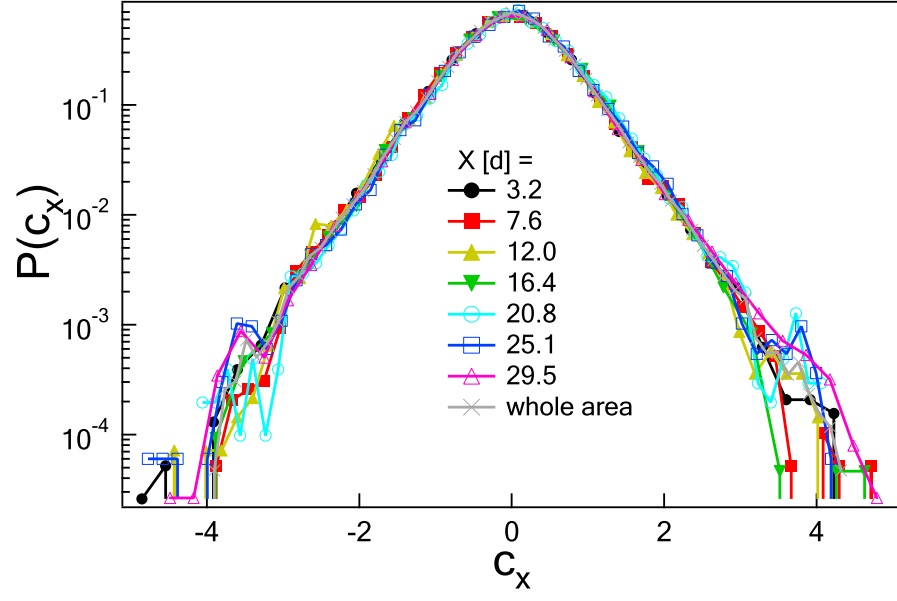
Figure 3.14. $P(c_x)$ for $\phi = 5.1\%$ at different horizontal positions x.
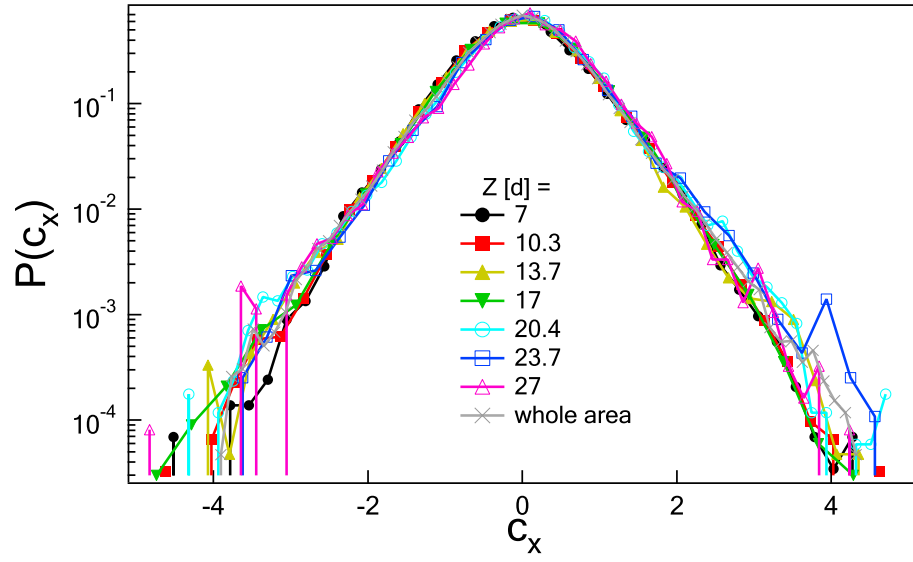
Figure 3.15. $P(c_x)$ for $\phi = 5.1\%$ at different vertical positions z.
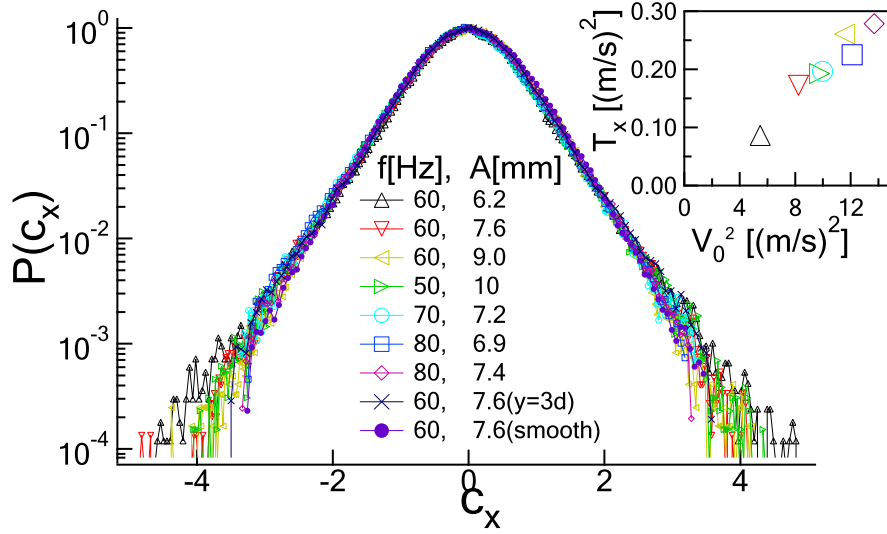
Figure 3.16. $P(c_x)$ for $\phi = 5.1\%$ for various driving frequencies and amplitudes, sampled at $y = 8d$. One data set taken with smooth top and bottom plates, and another set taken at $y = 3d$ are included for comparison. The inset shows the average kinetic temperature of the sampled region as a function of V_0^2, where V_0 is the amplitude of the driving velocity.

be expected when inter-particle collisions and heating events occur with comparable frequency. To test whether the influence of the boundary persists into the interior, we replace the rough glass plates by smooth Delrin plates and do not observe any change in $P(c_x)$. This suggests that the observed statistics are a consequence of inter-particle collisions, and are insensitive to the details of the driving surface.

Having established that distribution of horizontal velocities is insensitive to T, to the driving surface, and to location within the cell, we now discuss the dependence of $P(c_x)$ on the number density of particles. We have studied six volume fractions ϕ ranging from 1.8 to 7.2% with the results shown in Fig.3.17. The lower limit on ϕ is chosen so that the mean free path is still much smaller than the cell dimensions, and the upper limit is constrained by poor detection statistics at high volume fractions. Deviations from a Gaussian are apparent even at the lowest ϕ. With increasing ϕ, the tails of $P(c_x)$ get broader. Thus the velocity distribution varies continuously with

density unlike in some 2D experiments [14, 66] where $P(c_x)$ is unchanged over a broad range of ϕ. This is also unlike predictions for the homogeneously driven or cooled state [52] where $P(c)$ is independent of ϕ.

The high-velocity tail of $P(c_x)$ cannot be described by the form $\exp(-c_x^\beta)$: as shown in the bottom of Fig.3.17, a plot of $ln(-lnP(c_x))$ against $ln(c_x)$, shows curvature, whereas in the equivalent 2D experiment[14] we observed a straight line with a slope $\beta = 1.55 \pm 0.1$. The statistics in the experiment only capture the tail up to 4 decades below the peak, and leave open the possibility that this could be the asymptotic form of the distribution at large c. However, for any realistic description of grain dynamics, even rarer fluctuations are probably irrelevant. Earlier simulations[33, 39, 57, 58, 59] have found density-dependent velocity distributions, however, this is the first experimental study in 3D to observe this effect.

In the absence of predictions for the a boundary-driven system, we compare $P(c)$ to predictions for a homogeneously heated inelastic gas, where at small velocities, the deviations $D(c)$ from the gaussian distribution, $\Phi(c)$, have been perturbatively calculated [52, 53] as an expansion in Sonine polynomials $S_p(c^2)$:

$$P(c) = \Phi(c)\left[1 + D(c)\right] = \Phi(c)\left[1 + \sum_{p=1}^{\infty} a_p S_p\left(c^2\right)\right] . \tag{3.1}$$

The first two polynomials are $S_1(c^2) = -c^2 + \frac{1}{2}\hat{d}$ and $S_2(c^2) = \frac{1}{2}c^4 - \frac{1}{2}(\hat{d}+2)c^2 + \frac{1}{8}\hat{d}(\hat{d}+2)$ where $\hat{d}$ is the dimensionality. The coefficients a_p are given in terms of the moments of the distribution, $P(c)$: $a_1 = 0, a_2 = 4\langle c^4\rangle/(\hat{d}(\hat{d}+2)) - 1$. Predictions [52] for the dependence of a_2 on the restitution coefficient for the homogeneously heated and cooling states have been validated by both DSMC and event-driven simulations[54, 55, 56]. In Fig.3.18 we test whether the Sonine expansion is a good description of $P(c_x)$ in our boundary driven system by fitting the data for varying volume fraction to a second-order Sonine expansion with a_2 as a free parameter.
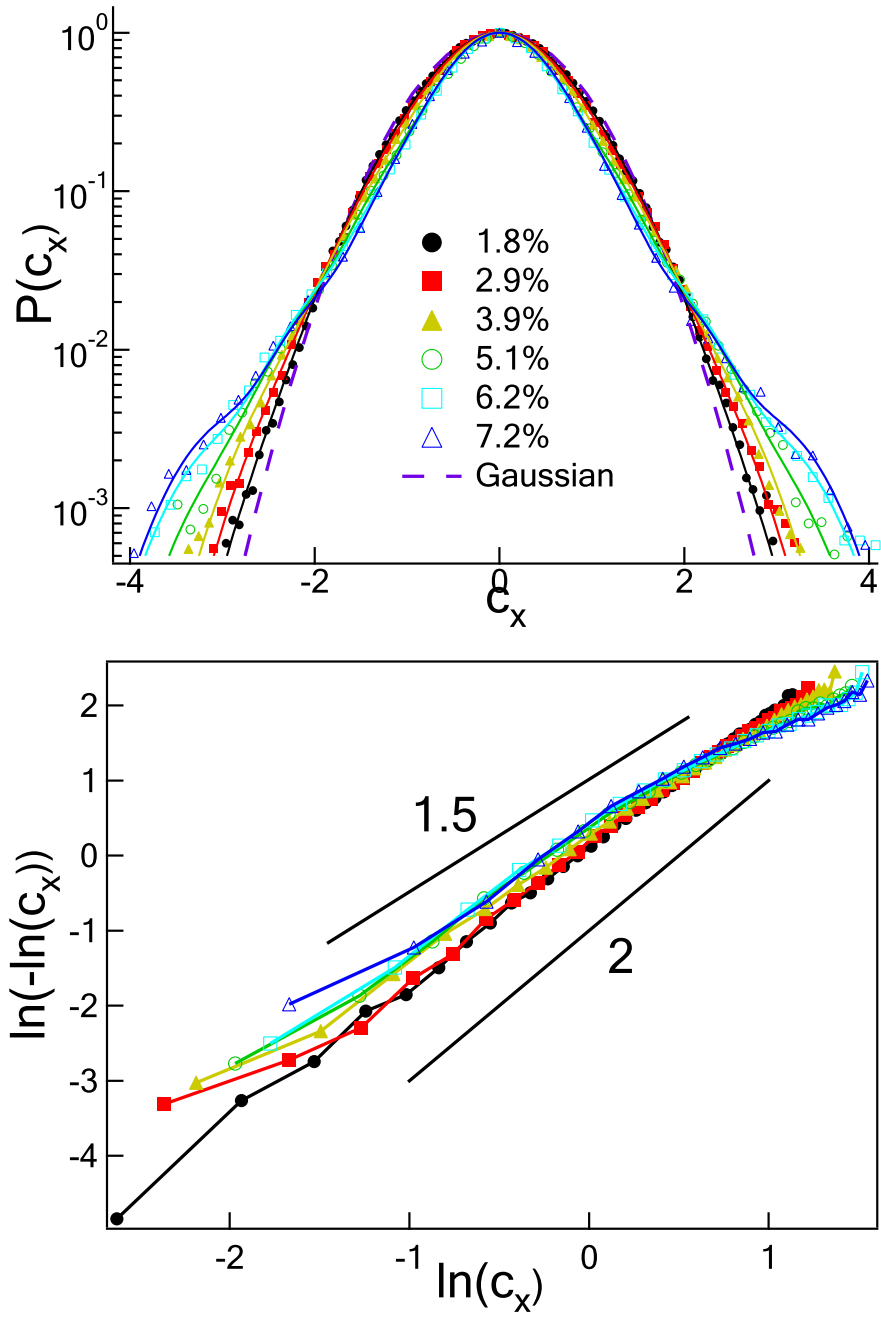
Figure 3.17. Probability distribution function for horizontal velocity at different volume fractions with the range from 1.8% to 7.2%. The smooth lines connecting symbols are a guide to the eye. The bottom shows $ln(-ln(c_x))$ vs $ln(c_x)$.
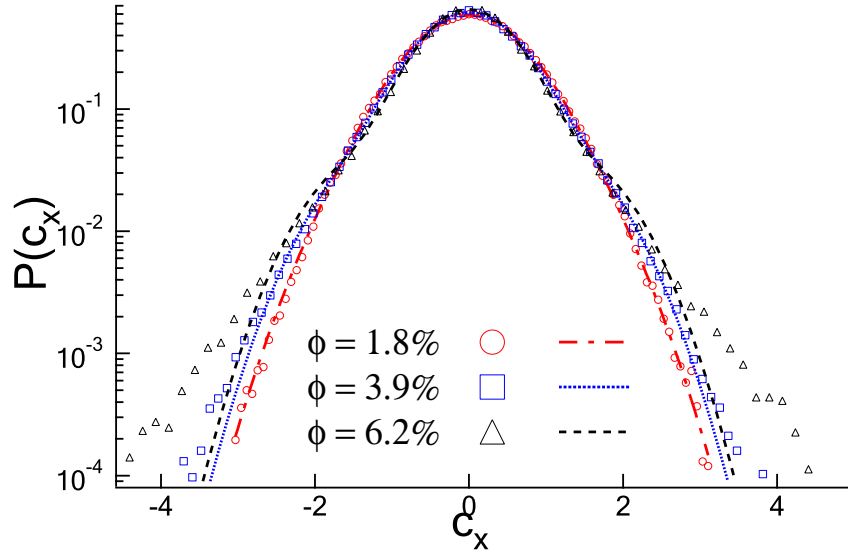
Figure 3.18. $P(c_x)$ at volume fractions $\phi = 1.8\%$, 3.9% and 6.2% fitted to second-order Sonine polynomials with a_2 treated as a free parameter.
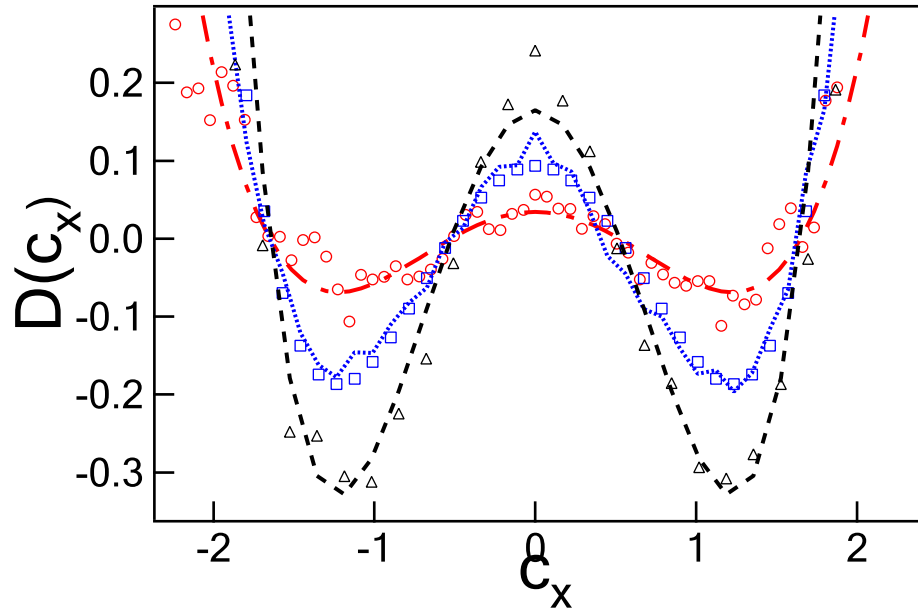
Figure 3.19. The deviation function $D(c_x)$ at small c_x for the above volume fractions.
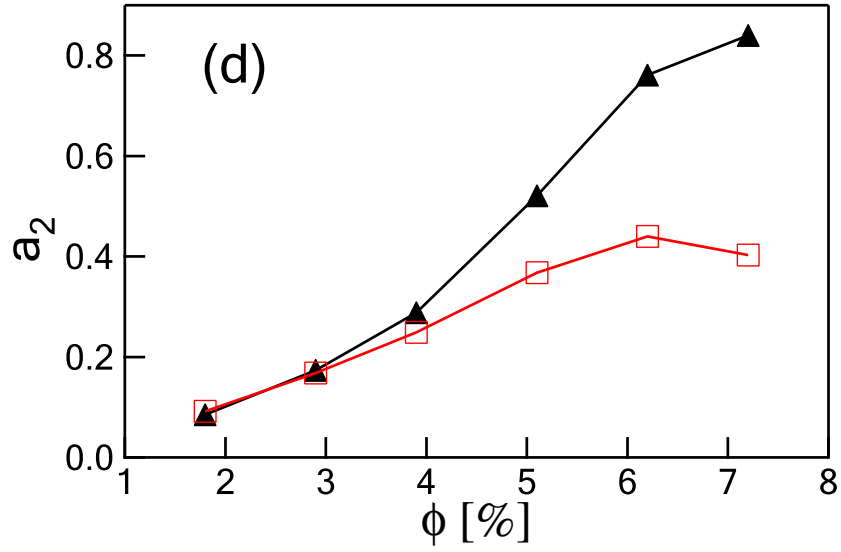
Figure 3.20. The best fit value of a_2 (▲) compared with a_2 (□) computed from $\langle c^4 \rangle$.

Fig.3.18 and Fig.3.20 show that the second-order Sonine correction works best at the lowest volume fraction and the range over which $D(c)$, the deviation from a gaussian, is well-fit diminishes at higher volume fractions. As in the quasi-2D experiment of [62] which models a homogeneously heated gas; the quality of the fit is reasonable for $c \lesssim 2$. A third-order Sonine term does not improve the fit, as shown in Fig.3.21.

Apart from the dependence on ϕ of the fit parameter a_2, we also note that a_2 is opposite in sign, and much larger in magnitude than that found in the homogeneously heated or cooled states for the same nominal restitution coefficient. Furthermore, as shown in Fig.3.20 the best-fit value of a_2 disagrees with the value directly calculated from the 4th cumulant, $\langle c^4 \rangle$, raising the possibility that the gaussian reference state may not be appropriate for a boundary-driven system. To our knowledge, the only predictions for P(c) in a boundary-driven system were made in [68], where the 4th cumulant is treated as an independent hydrodynamic field. They find $\langle c^4 \rangle$ shows a
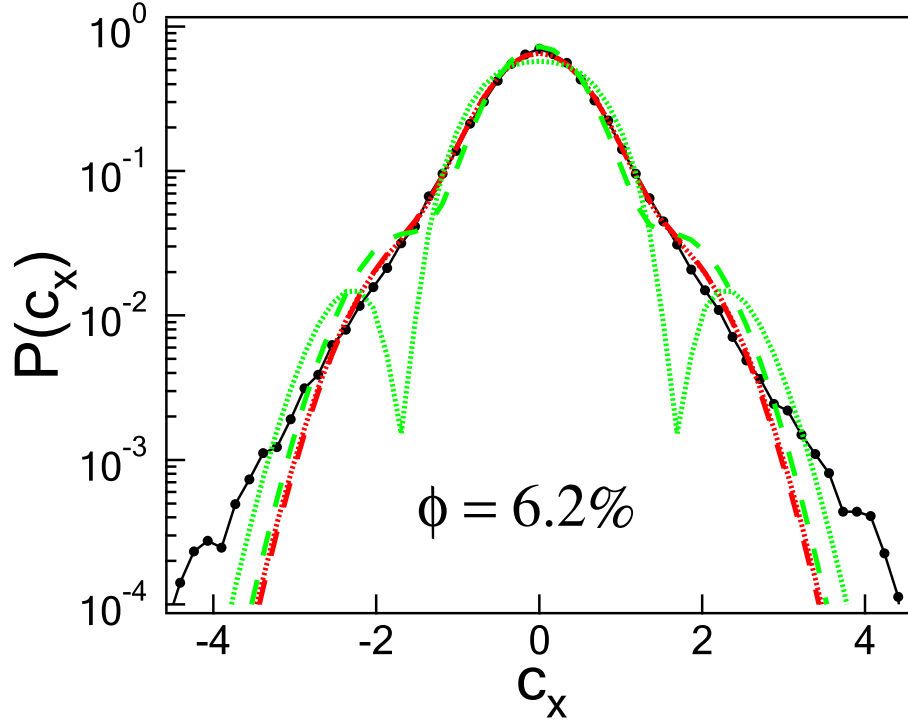
Figure 3.21. $P(c_x)$ at volume fraction $\phi = 6.2\%$ with best fit second- (red dash line, $a_2 = 0.440$) and third-order (red dotted line, $a_2 = 0.455$, $a_3 = $ -0.0287) Sonine forms. We also plot the distribution function up to the second- (green dash line) and third-order(green dotted line) with the predicted Sonine coefficient a_2 and a_3.

density dependence qualitatively like ours, but with much lower magnitude than we measure.

3.5   Velocity correlations and energy anisotropy

A general consideration regarding $P(c)$ is that if a velocity distribution is isotropic and if the velocity components are uncorrelated, it must be a gaussian distribution. A non-gaussian distribution implies that one or both of these assumptions is invalid. For low volume fractions, the velocity fluctuations are anisotropic, but they become more isotropic at higher densities. This trend is shown in the inset to Fig.3.22 where the anisotropy is quantified by $\langle v_z^2 - v_x^2 \rangle / \langle v_z^2 + v_x^2 \rangle$. However, since the velocity distribution does not tend towards a Gaussian at large ϕ, the velocity components must be correlated as shown in Fig.3.22. Indeed, the correlation between velocity components $\langle v_x^2 v_z^2 \rangle / \langle v_x^2 \rangle \langle v_z^2 \rangle$ grows with volume fraction ϕ.

Our measurements of the 3D particle kinematics in the interior of a vibration-fluidized granular medium thus reveal a non-Gaussian velocity distribution that is insensitive to conditions at the driving surface. The shape of the distribution evolves continuously with volume fraction; the functional form differs markedly from the homogeneously heated state, thus emphasizing the need for theoretical development for boundary-driven systems.
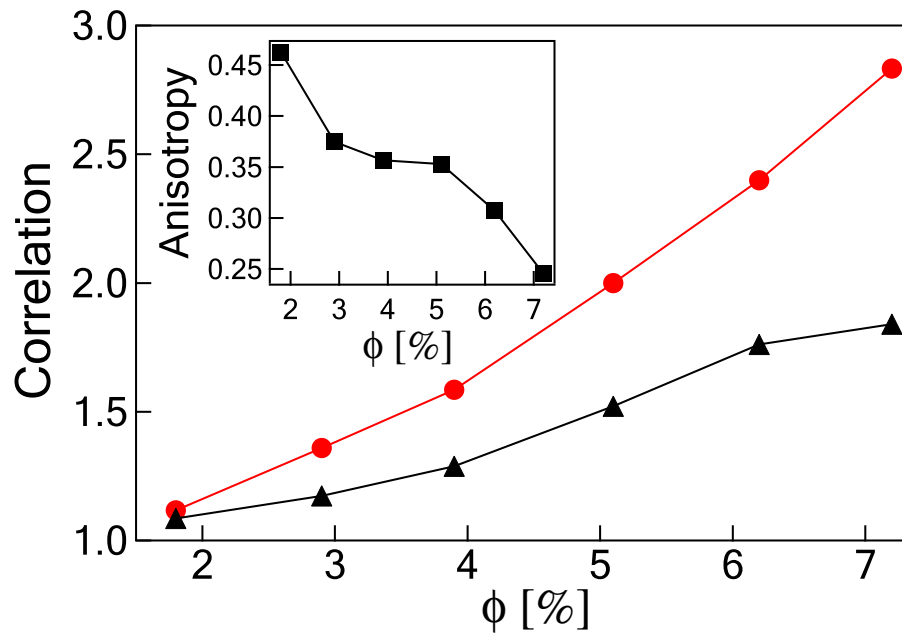
Figure 3.22. The correlation of v_x and v_z ($\bullet$), compared with the correlation implicit in the Sonine formula($\blacktriangle$): $1 + a_2$. The inset shows the anisotropy, $(v_z^2 - v_x^2)/(v_x^2 + v_z^2)$.

CHAPTER 4

POWER FLUCTUATIONS IN A BOUNDARY DRIVEN GRANULAR GAS

4.1 Introduction

Recently, a series of results known as fluctuation theorem(FT) gave a strong statement for systems arbitrarily far from equilibrium. Initially observed in sheared fluid[69] and later rigorously proven for chaotic time reversible thermostatic steady state [26] fluctuation theorem can be stated in terms of a simple mathematical relation,

$$\Pi(\sigma_\tau)/\Pi(-\sigma_\tau) = \exp(\sigma_\tau \tau) \qquad (4.1)$$

Here $\Pi(\sigma_\tau)$ is the probability of observing a positive entropy production rate σ_τ, measured over a time interval τ and this relation strictly hold as τ goes to infinity. In the dynamical system[26] first considered in the theoretical developments of FT, the entropy production rate σ_τ, is defined in terms of the "phase space contraction rate". In this chapter we are going study this fluctuation relation in terms of two types of power fluctuations in a boundary driven granular gas.

The fluctuation relation Eq.(4.1) has been applied in various practical systems. Examples include extending the entropy fluctuations from dynamical systems to stochastic systems[70], fluctuations of momentum flux in a two-dimensional shear flow[71], turbulence in shear flow[72], study of a granular medium model[73] and a Burridge-Knopoff spring-block model[74], fluctuations of electrical current in steady

chaotic convectional motion of a liquid crystal film[75], temperature fluctuations in a Rayleigh-Benard cell[76], work fluctuations of a colloid particle in an optical trap[77, 78, 79], energy fluctuations in electric circuits[80, 81].

The remarkable features of the fluctuation theorem are the absence of adjustable system-dependent parameters and applicability to systems far away from equilibrium. It is then natural to ask whether or not the fluctuation relation can be observed in a granular system, which is a system typically far from equilibrium. This has previously been studied in the experiment[82] and simulations [74, 73] with theoretical discussion covered in [83, 84, 85]. Since it is hard to measure entropy production or consumption directly for granular matter, an important issue to settle is what should be the appropriate fluctuation variable. In the previous experiment of our group, we measured fluctuations of a kind of stream power transported in and out of a subsystem centered in a vibrated granular gas[82]. Another group by Aumaitre *et al* has taken the energy transferred to the whole granular gas by a vibrated piston as the fluctuation variable[74, 73]. It is to be mentioned that the fluctuation relation Eq.(4.1) was proved strictly in mathematical form for a time reversible thermostatical and chaotic dynamic system [26]. When the role played by phase space contraction rate or entropy production rate is replaced by power fluctuations, there is no guarantee that fluctuation relation Eq.(4.1) should be satisfied. And there is argument if power fluctuations can be applied to the fluctuation theorem[86]. However, a good statistical agreement is still observed in the range under study in [82, 74, 73].

In this dissertation, I will describe my numerical study of two types of power fluctuations in a granular gas similar to that in the experiment[82] by event-driven molecular dynamics simulation. Taking advantage of the convenience of computer simulations in selecting and changing system parameters we can explore these two kinds of power fluctuations in far more details compared with that in experiments. One of the interesting result in [82] is the natural emergence of a new quantity in

unit of kinetic temperature, called "effective temperature T_{eff}". Our numerical simulations here will more focus on properties of this new "effective temperature" and its comparison with kinetic temperature T_{kin}.

4.2 Systems for numerical experiments

As that in the experiment [82], the granular system under study is a 2D granular gas confined in a rectangular cage with width W and height H. Energy is supplied from the top and bottom boundaries and dissipated by intrinsic particle-particle collisions to maintain the whole system at a steady state. The energy transfer in the vertical direction leads to a vertical kinetic temperature gradient which is at the boundary and lower in the center. For a subsystem located within the cage, the mechanical energy balance over a time interval τ can be expressed as

$$\triangle E = D_b + D_i + P + \triangle E_g. \tag{4.2}$$

where $\triangle E$ is the total energy change of this subsystem, D_b is the energy exchange due to collisions at the boundary (one of the colliding pair of particles is inside the subsystem while the other one is outside), D_i is the collision energy lost with both particles inside the subsystem and P is the energy change by particles moving into(added) and out(subtracted) of the subsystem which is named as the streaming component of the power considered in [82], $\triangle E_g$ is the change of total gravitational energy. In a steady state, the time-average value of $\triangle E$ should be zero. $\triangle E_g$ also has a zero average and is much smaller in magnitude than the other terms in Eq. 4.2 in this strongly excited system. The average power transferred to the subsystem by the streaming part P is balanced by the summation of the two kinds of collision part $D_b + D_i$ and we get

$$< P >= -(< D_b > + < D_i >). \tag{4.3}$$

Actually, if we only think about heat released by intrinsic inelastic collisions, the entropy production is always positive and observation of fluctuation relation is impossible. However, the kinetic temperature gradient in the vertical direction creates a positive average of P and a negative average of $D_B + D_i$ and thus gives hope to apply fluctuation relation to these two kinds of power fluctuation quantities. In the experiment [82], only the streaming part P is studied. Here, we will consider the fluctuations of both the streaming part P and the collision part $D_B + Di$. It is necessary to mention that if we count the actual energy supplied to the subsystem from its environment, the fluctuation quantity should be $P + D_B$ and the average value of this variable is unequal to zero. But our simulations do not support such a choice. Taking $P + D_B$ as the fluctuation variable can not satisfy the fluctuation relation.

Therefore, the fluctuation relation to be tested here is changed from Eq.(4.1) to

$$\Pi(p_\tau)/\Pi(-p_\tau) = \exp(p_\tau \tau/T_{eff}) \tag{4.4}$$

where p_τ is the power flux averaged over a time interval τ and τ is expected to be larger than any hydrodynamic or correlation time scale of the system. As described above, we have two choices of p_τ, namely P/τ, and $(D_b + D_i)/\tau$. The appearing of the new quantity T_{eff} is natural. When we replace the entropy production rate σ_τ by the power fluctuation rate p_τ, there is no problem for the left hand side since it is only a ratio of probability. However, for the right hand side of Eq. 4.1, the non-dimensionality quantity σ_τ is replaced by power fluctuation p_τ in the unit of energy(kinetic temperature)/time. To make the right hand side with correct dimensional unit, introducing of a new variable is unavoidable. The new variable introduced is in unit of energy, and it is defined as the effective temperature T_{eff} [82]

In order to make close comparison with the experiment[82], the event-driven molecular dynamics simulation is performed with N hard disks(diameter d=1.6mm) in a 2D rectangular cage with a dimension $W \times H$. Particles move in the 2D cage and

63

rotate along the axis perpendicular to the 2D plane. Collisions between particles are instantaneous and the inelasticity is characterized by a normal elastic efficient ϵ and two friction related parameters μ and β_0. μ is the dynamic friction coefficient and β_0 is used to distinguish sliding and sticking collisions[20]. Between subsequent collisions, particles move freely under the gravity g which is pointed downward. Instead of the fixed boundary in experiments, periodic boundary is applied in horizontal direction.

In the experiment[82], a continuous energy supply comes from the vibrated top and bottom plate. Here we also use this driving method. In addition to driving by vibration, we can use thermal walls to energize the system from boundary. We can keep positions of the top and bottom plates fixed and maintained at a thermal temperature T_s. After a collision of a particle with the thermal wall, the particle is kicked back with the normal velocity selected randomly from a Gaussian distribution

$$\phi(v_z) = \frac{m}{k_B T_w} |v_z| \exp[-\frac{m v_z^2}{2 k_B T_w}] \tag{4.5}$$

. For comparison, we also apply thermal boundary driving to study T_{eff}.

A snapshot of the system is shown in Fig. 4.1. The sampling of both the streaming(P) and collision($D_b + D_i$) power fluctuations are taken on a rectangle window centered in the cage. Typically the height of this window h is chosen to be $1.5d$, a small number to get small gradients of kinetic temperature and number density in vertical direction. The width of the sampling window is as big as that of the cage. Therefore, particles can only move into and out of the sampling area from top and bottom. We define the power flux at time t as $p(t)$. The average power during a time piece τ is then $p_\tau(t) = \frac{1}{\tau} \int_t^{t+\tau} p(t')dt'$. A normalized power $P(t) = p(t)/\overline{p(t)}$ is defined and correspondingly, $P_\tau = p_\tau/\overline{p_\tau(t)}$, where $\overline{p(t)}$ is the time average of $p(t)$ and $\overline{p_\tau}$ the time average of p_τ.
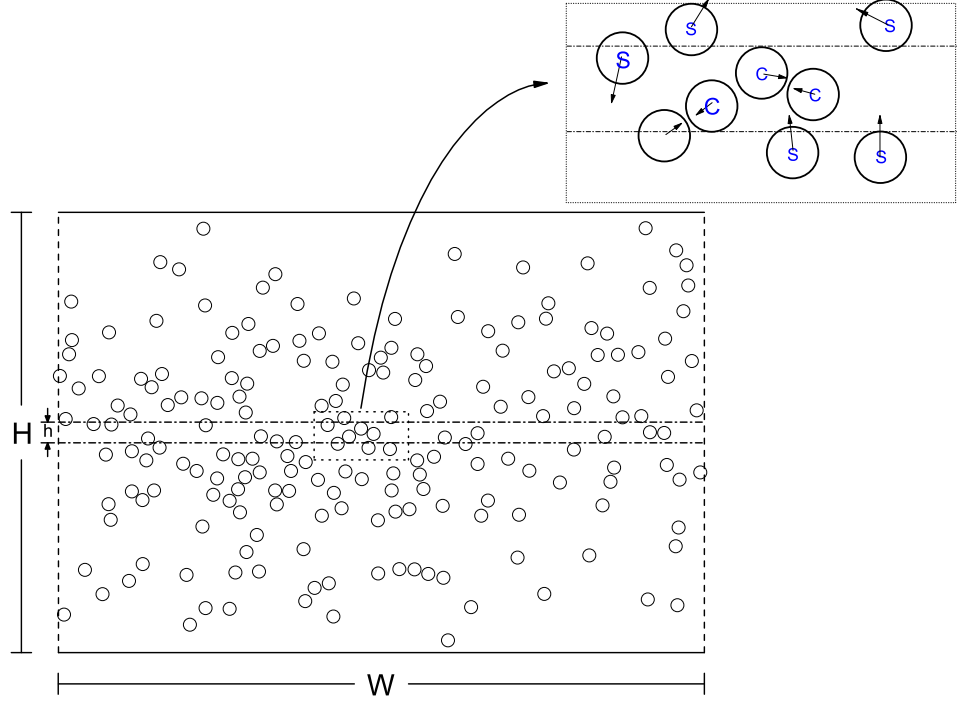
Figure 4.1. Sketch of the simulation box with width W and height H. Periodic boundary conditions is applied as indicated by dashed lines. External driving is supplied from the top and bottom plate. Gravity points vertically downward. The dash dotted thin stripe of height h centered in the system box and extended across the whole system width in horizontal direction is the sampling window for power flux statistics. The top right inset is an illustration for the streaming part(indicated by s) and collision part(indicated by c) power flux.
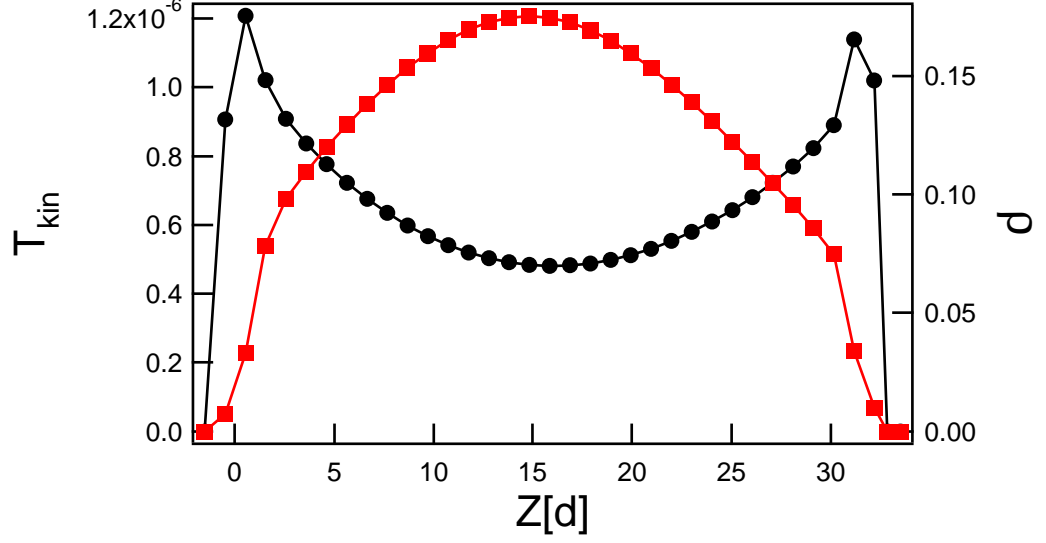
Figure 4.2. Kinetic temperature T_{kin}(●, left scale) and number density(■, right scale) versus height Z[d].

4.3 Spatial kinetic temperature and number density profiles

In Fig. 4.2 we show the typical kinetic temperature and number density profiles along the vertical direction under vibration driving. The profiles for thermal boundary driving in a similar shape. Since we heat the system from bottom and top, the kinetic temperature is greater near the boundaries and smaller in the center whereas the number density shows the opposite trend. Due to the influence of gravity g, the peaks of the profiles is a little bit off the geometrical center. Under such a strong external driving, the influence from gravity can be negligible. The slope of these gradients are smaller in the center than close to boundaries. In the horizontal direction, due to periodic boundary condition both profiles are uniform and we choose to not show them here.

4.4 Statistics of two types of power fluctuations

The probability distribution for fluctuations of the streaming power $\Pi(P_\tau^s)$ and collision power $\Pi(P_\tau^c)$ are illustrated in Fig. 4.3(a) and Fig. 4.3(b) for a vibration

system. For the normalized streaming power fluctuation $\overline{P_\tau^s}$ with an average value 1 and the normalized collision power fluctuation $\overline{P_\tau^c}$ with an average value -1, substantial negative/positive tails are observed. At the same time, although their average values are symmetric about the axis P_τ equal to zero, these two kinds of distributions themselves are not mirror symmetric about each other. Fig. 4.3(c) and Fig. 4.3(d) show the evolving of the ratio $ln[\Pi(p_\tau)/\Pi(-p_\tau)]$ with various τ. Since the collision term has a negative average, we plot this term with a negative sign in order to allow direct comparison with the streaming term with a positive average to get the slope positive(and later to get a positive collision effective temperature for comparison). Dividing $ln[\Pi(p_\tau)/\pi(-Pi_\tau)]$ by τ we get Fig. 4.3(e) and Fig. 4.3(f) and the convergence of $ln[\Pi(p_\tau)/\Pi(-p_\tau)]/\tau$ at large τ is observed.

Effective temperature T_{eff} is the inverse of the slope at large τ asymptote shown in Fig. 4.3(g) and Fig. 4.3(h) for T_{eff}^s and T_{eff}^c. It is noticed that the time interval τ needed for convergence of P_τ^c is much smaller than that needed for P_τ^s. The effective temperature T_{eff}^c is a little smaller than T_{eff}^s. This is consistent in all the simulations we have done. And the difference of the two kinds of effective temperatures is not due to the existence of gravity g. We verified this by simulating over the same system without gravity g. It is found that even without g, T_s is still a little bigger than T_c. Compared with the experiment[82], the convergence time is much longer. This might partly because of that the sampling region is much thinner than that in the experiment. It is also argued that the convergence here is a linear approximation due to shortage of events that are able to be observed for large negative power fluctuations in the capacity of experiments and simulation resources[73, 83]. Unfortunately, our simulation results also can not give us enough data for statistics of negative power fluctuation, which seems to need much longer simulation time that prevents a direct test of this argument.
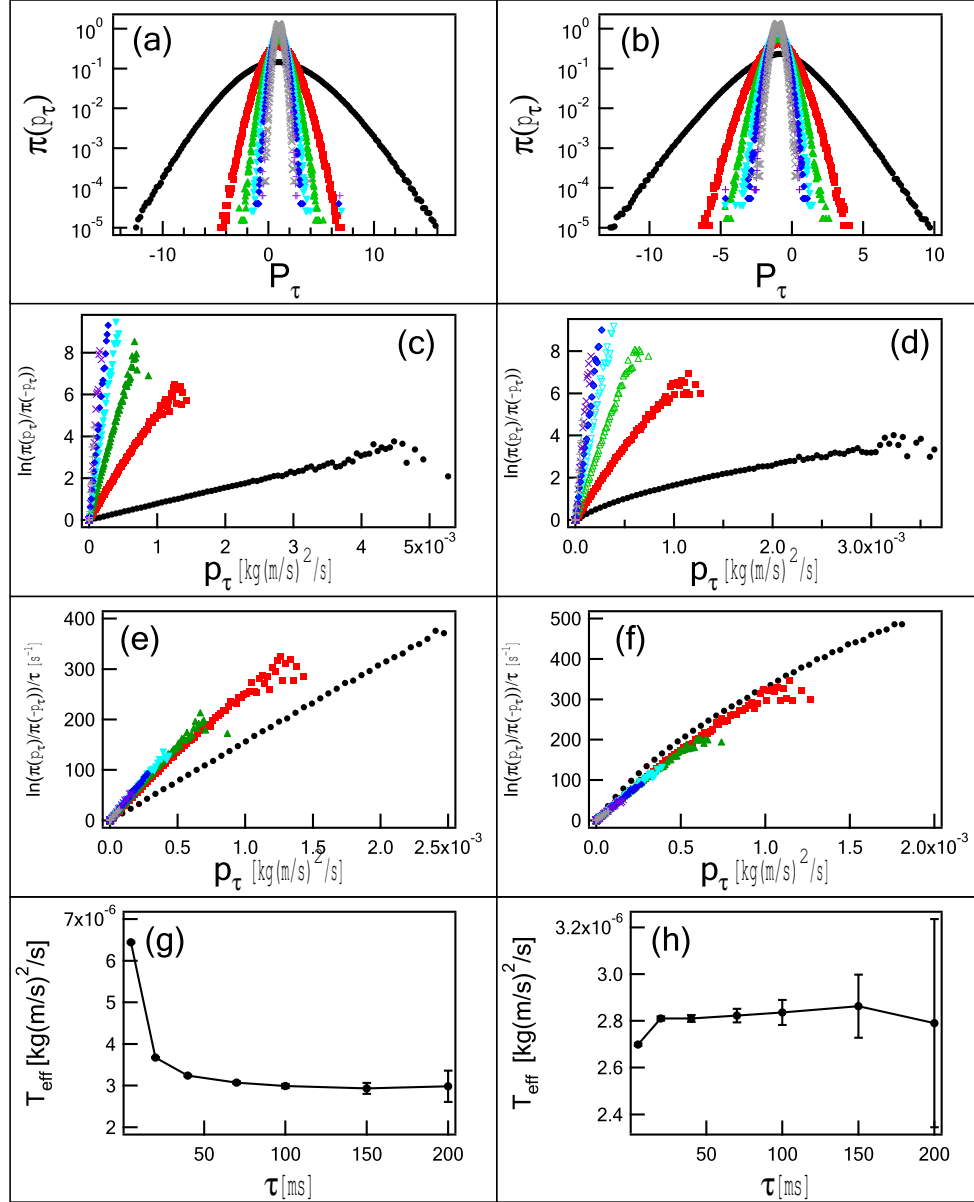
Figure 4.3. Probability distribution $\Pi(P_\tau)$ for streaming part(a) and collision part(b) at different sampling interval τ(● 5ms, ■ 20ms, ▲ 40ms, ▼ 70ms, ♦ 100ms, × 150ms, + 200ms). The normalized average value of streaming power flux $\overline{P_\tau^s}$ is 1 and -1 for collisional power flux. Graphs (c) and (d) are $\ln[\Pi(p_\tau)/\Pi(-p_\tau)]$ versus p_τ of streaming part(c) and collision part(d). Graphs (e) and (f) are $\ln[\Pi(p_\tau)/\Pi(-p_\tau)]/\tau$ versus p_τ for streaming part(e) and collision part(f). (g) and (h) is the T_{eff} calculated for streaming part(g) and collision part(h) versus τ. The system is composed of 200 particles under vertical vibration. The vibration amplitude is 1.0d and the frequency 160Hz.

4.5   The exploration of effective temperature

To be a temperature-like variable, the "effective temperature" should be an intensive quantity. The dependence of this new effective temperature T_{eff} on the area of sampling regions is studied in Fig. 4.4. In Fig. 4.4(a), we change the system width W from $16d$ to $80d$ and keep the number density of particles fixed. In this case the sampling window width L is changed at the same scale correspondingly. In Fig.4.4(b), the system width W is fixed at 96d while the sampling window width L is changed from 16d to 80d. By expanding in the horizontal direction, we are able to keep most of the physical quantities(number density, kinetic temperature, gradients etc.) the same while only changing the size of the subsystem under study. It is shown in Fig. 4.4 that T_{eff} is independent of the system width. This is apparently different from that observed in the simulations of a two-dimensional shear flow model[71] where only energy flux through a single line is taken into accounted, in which T_{eff} was found to be size-dependent.

The dependence of T_{eff} on T_{kin} is studied in Fig. 4.5 with T_{kin} varied by a factor more than 5. Both the thermal boundary driving and vibrated boundary driving are used. The driving is strong enough that the shapes of number density and kinetic temperatures profiles along the vertical direction are kept with little change. T_{kin} and T_{eff} are sampled in the subsystem defined by the sampling window. In the thermal boundary driving T_{kin} is changed by changing the boundary temperature T_w(see Eq.(4.5)) while in vibration driving we keep the vibration amplitude fixed and only change the vibration frequency. The results clearly indicate that the ratio T_{eff}/T_{kin} does not depend on T_{kin}.

We also tested the dependence of T_{eff}/T_{kin} on different vibration amplitude. It is found that T_{eff} changed significantly as the vibration amplitude in this 48dx32d cage changed from 0.5d to 2.6d. The ratio T_{eff}/T_{kin} is found to increase with the vibration amplitude. To check whether or not this is due to boundary effect, we simulate again
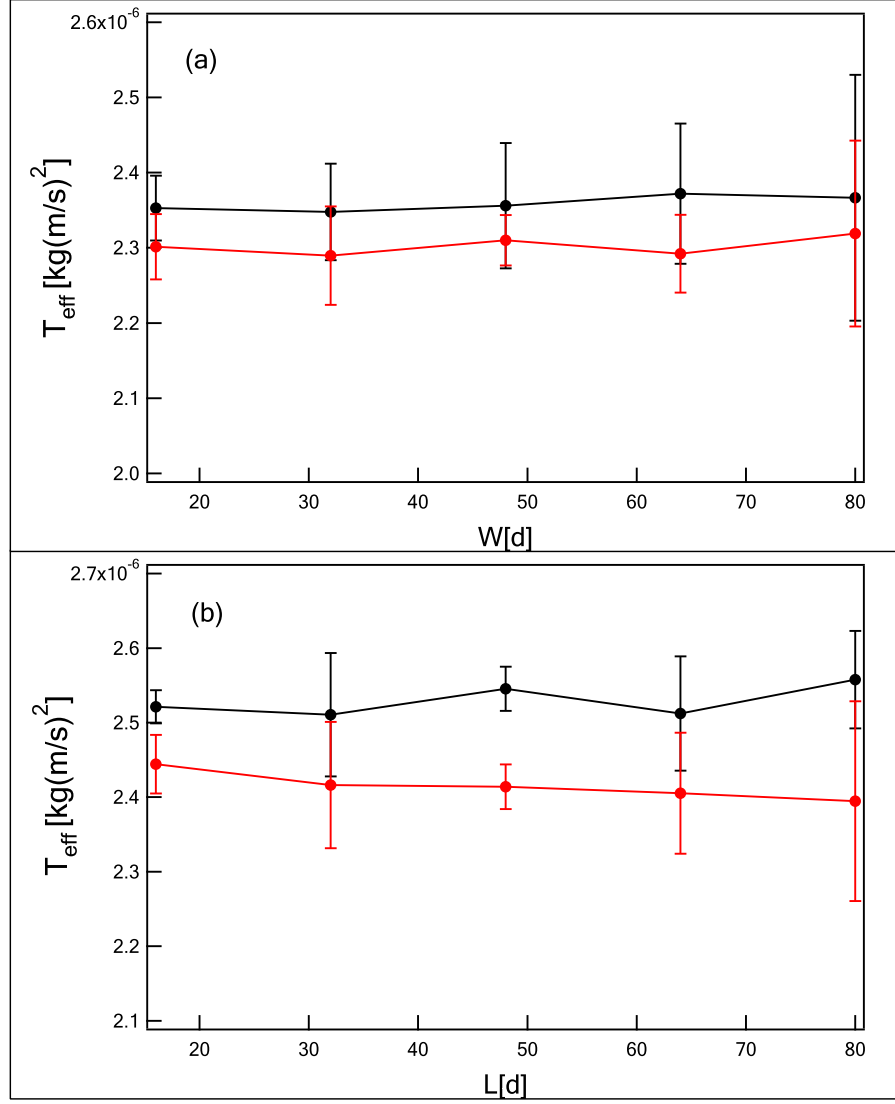
Figure 4.4. (a)T_{eff} at different system width W. (b)T_{eff} at different sampling window width L with system width fixed at 96d.
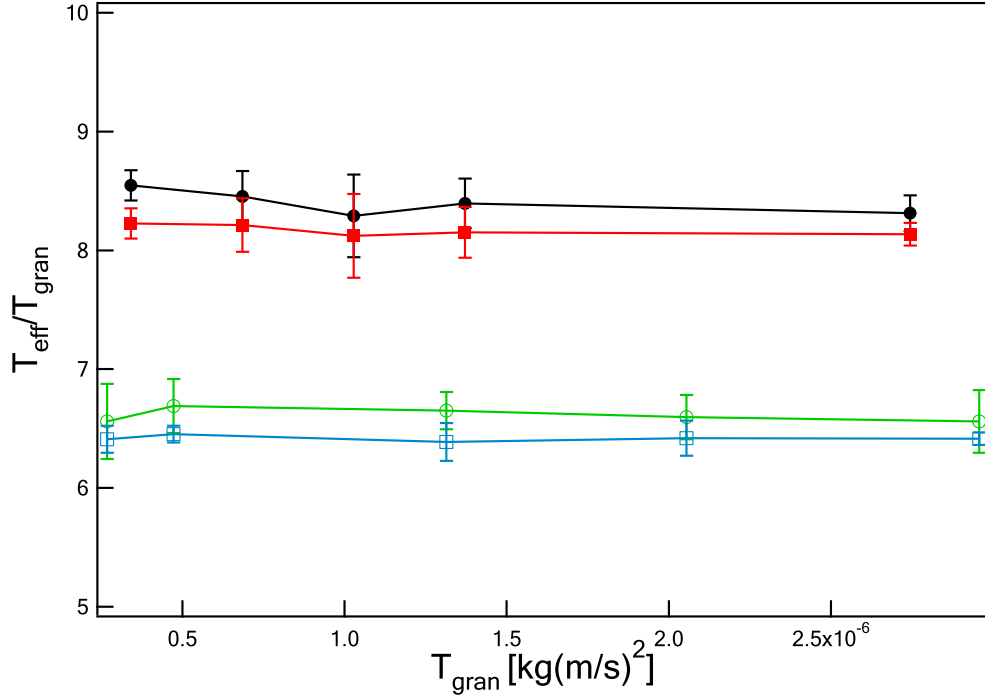
Figure 4.5. The ratio between T_{eff} and T_{kin}. Symbols $\circ$ and $\square$ represent the streaming and collision part under vibrational boundary driving. Symbols $\bullet$ and $\blacksquare$ represent the streaming and collision part under thermal boundary driving.

in a thin and tall cage with a dimension $24d \times 64d$. We find that the ratio dependence becomes less sensitive as show in Fig.4.6, especially when the vibration amplitude is small. An interesting finding is that although the ratio T_{eff}/T_{kin} does not depend on external driving now (T_{eff}/T_{kin} already remains constant at small amplitudes), the temperature ratio we get in the vibration driving system is still different from that we get from systems with thermal boundary driving. This is strange since most of the macroscopic field physical quantities in these two physical situations are very close, including number density, kinetic temperature and the gradients of these quantities. We have tested the velocity distribution in these two kinds of driving and the difference is still very small. Whether there is other microscopic dynamical difference between these two types of driving or if it is hinted that the effective temperature is not just not just a function of local hydrodynamic quantities is unclear.
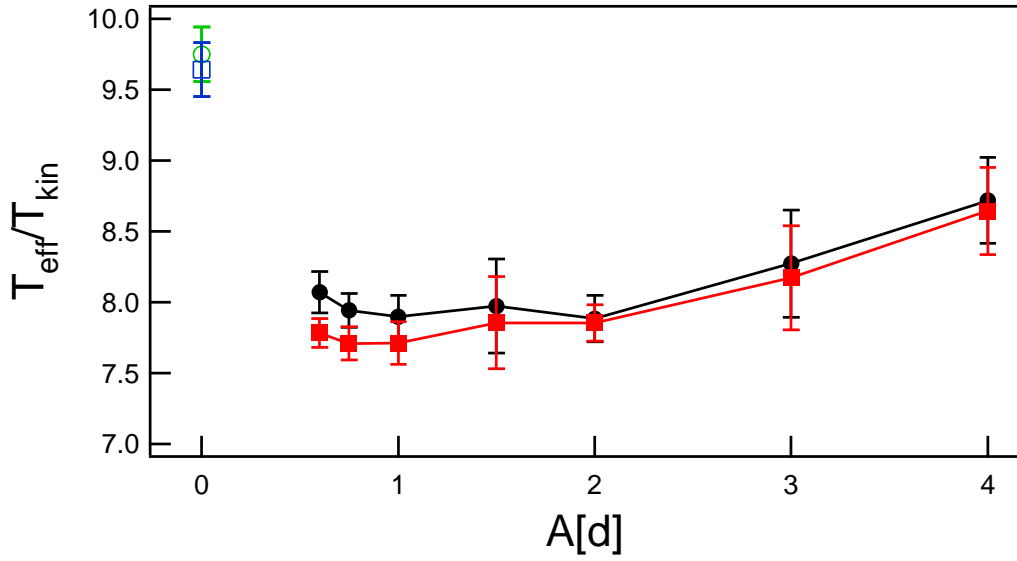
Figure 4.6. T_{eff} in a thin tall box with width 24d and height 64d. The measurement is taken within a thin stripe in the center of this box with the sampling window height h 1.5d. Symbols ● and ■ represent T_{eff}/T_{kin} of the streaming and collision part for systems under external vibration with the vibration amplitude varying from 0.6d to 4d. For comparison, we also measured T_{eff}/T_{kin}(○ for streaming and □ for collision) in the same system with thermal boundary driving. The total number of particles are 150 and the normal restitution coefficient is 0.98.

So far, the sampling is taken at the center of the cage where the gradients of density and kinetic temperature are small. It is also interesting to know if the gradient of kinetic temperature will influence the ratio of T_{eff}/T_{kin} or not. In [83], it is found that the effective temperature greatly depend on the kinetic temperature gradient across the sampling region. Therefore, we shift the sampling window from the center to close to the bottom while keeping the size of the sampling window constant. The temperature ratio at different vertical positions in the system is shown in Fig. 4.7. For comparison, the local density and kinetic temperature profile is also plotted. We find that the ratio of T_{eff}/T_{kin} does not depend on gradient very much, especially for the three data points measured as the sampling window close to system center where the kinetic temperature gradients changed most significantly. As we know from Fig. A.3 below, T_{eff}/T_{kin} also depends on local number density. To exclude the density effect here, we tried another simulation with fewer total number of particles to make the local density at the system center the same as that at $z = 9d$ here. A new sampling window is taken at the same local number density but much lower kinetic temperature gradient. The measured ratio T_{eff}/T_{kin} is added to Fig. 4.7, which is about twenty percent lower than the ratio measured at $z = 9d$. This verified our conclusion that ratio of T_{eff}/T_{kin} does not depend strongly on the gradient of kinetic temperature.

Similar with changing sampling window size in horizontal direction, we tried to change the size of the sampling window in the vertical direction. As we keep the cage size at 48x32d and change the sampling window height h, T_{eff}/T_{kin} does not stay constant as shown in Fig.4.8. As h goes up, the ratio goes down and finally seems to approaches to a plateau. Although the size change in the vertical direction induces the changes of a few physical quantities, including local number density, temperature gradients and kinetic temperature etc., the change of the temperature ratio due to these local hydrodynamic quantities should be small. Actually, as h changes from

73
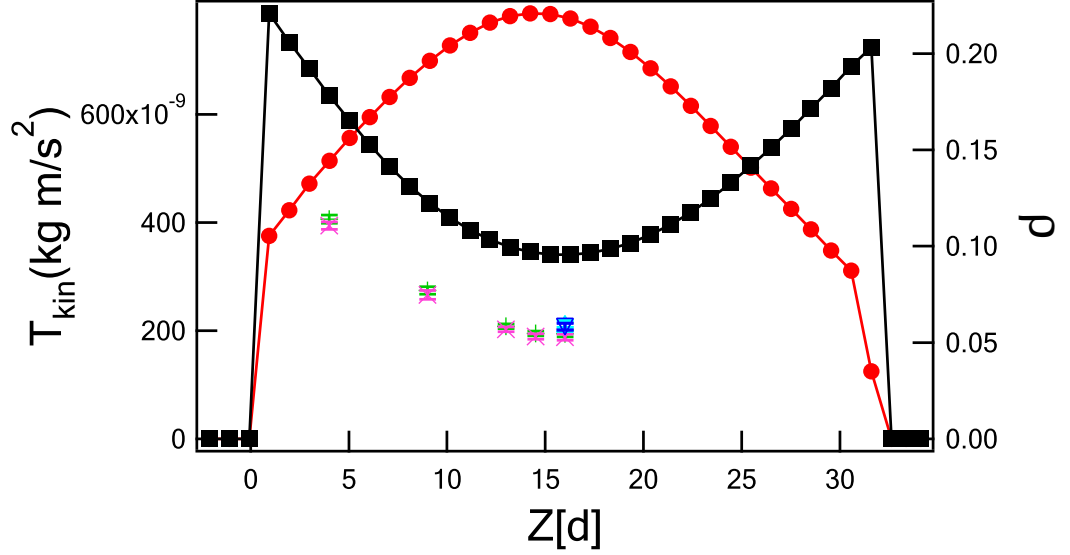
Figure 4.7. The dependence of T_{eff} on different kinetic temperature and number density gradients. The total number of particles are 250 and the system is under thermal boundary driving. Symbols ■ and ● correspond to the kinetic temperature(left scale) and number density(right scale) versus height Z[d]. Symbols + and × represent T_{eff} measured at the corresponding height(with the sampling window height h all kept at 1.5d) divided by 9 for eye convenience. We also measured another set of T_{eff}(△ for streaming and ▽ for collision) by selecting a system with the same local density in the center of this system (where the density and kinetic temperature gradient are both small) as that represented by the second point of + and ×(where the gradients are large). It's easy to see that the effective temperatures of these two points are not much different while the gradients of kinetic temperature and number density are significantly different.
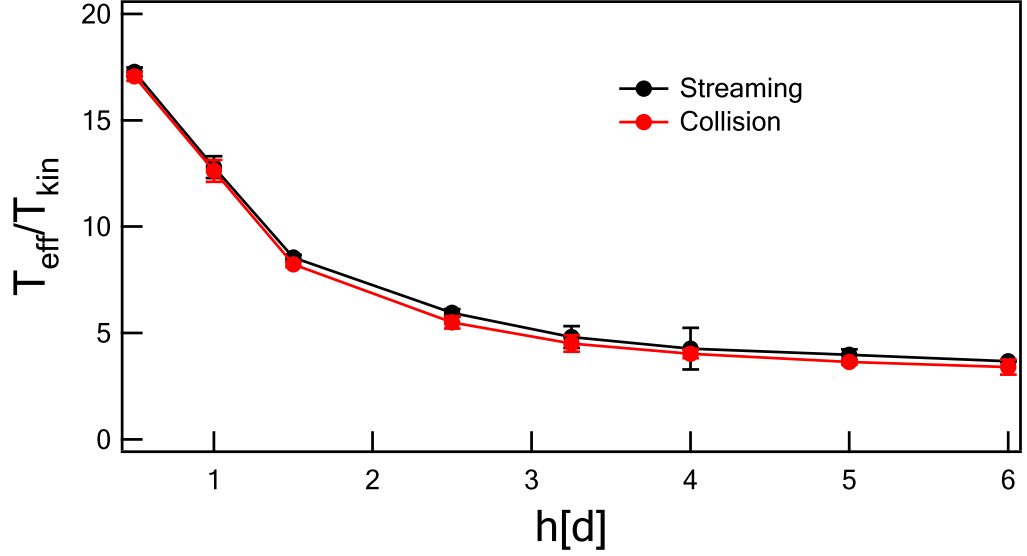
Figure 4.8. Ratio T_{eff}/T_{kin} versus different sampling window height h.

0.5d to 6d, the change of local number density is less than 10%. Meanwhile, the kinetic temperature gradient does change a lot but as shown above this should not be the main cause for the big change of T_{eff}/T_{kin}.

The dependence of T_{eff}/T_{kin} on particles number density and elastic coefficient is shown in Fig. 4.9 and Fig.4.10 for both vibrational driving and thermal boundary driving. The ratio increases along with number density. With the normal elastic coefficient ϵ changed from 0.7 to 0.99, the ratio T_{eff}/T_{kin} decreases first then increase, forming a plateau at ϵ around 0.9.

4.6   Summary

By molecular dynamics simulations we study the streaming and collision type of power fluctuations in a boundary driven 2D granular gas. The gradients of kinetic temperatures in the vertical direction make the average power fluctuations of these two types to be unequal to 1 and provides us the possibility to apply the fluctuation relation. Our results verified that the statistics of these two kinds of power fluctuations both show agreement with the fluctuation relation in the parameter range we
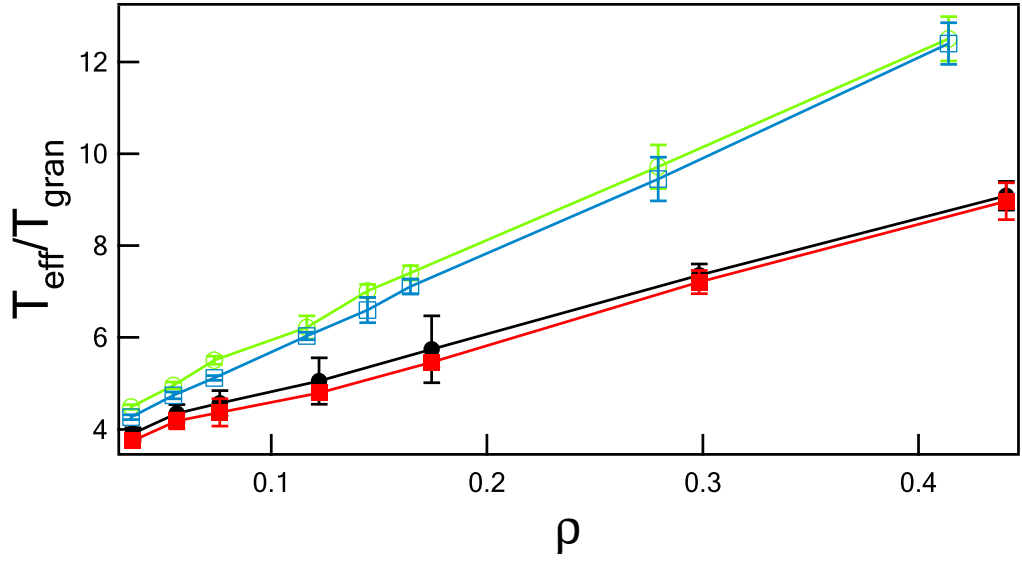
Figure 4.9. T_{eff} versus particles number density inside the sampling region. Symbols ● and ■ correspond to the streaming and collision part for systems under vibrational driving. Symbols ○ and □ correspond to the streaming and collision part under thermal boundary driving.
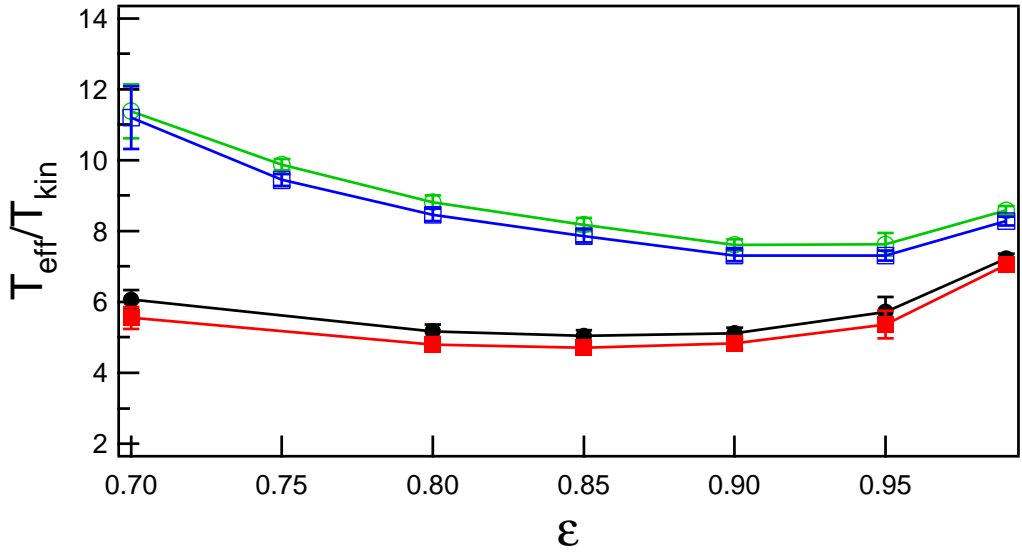
Figure 4.10. T_{eff} versus different restitution coefficients. Symbols ● and ■ correspond to the streaming and collision part for systems under vibrational driving. Symbols ○ and □ correspond to the streaming and collision part under thermal boundary driving.

studied. The effective temperatures arose from the fluctuation relation is also studied with the changing of various system parameters. It is found that the effective temperature does not depend on kinetic temperature and system width, but does depend on elasticity, number density and sampling box height h. Our results also show that kinetic temperature gradient is not a critical effect in determining T_{eff}. Besides these numerical findings, our simulation results also leave us a few open questions that need further understanding.

CHAPTER 5

SUMMARY

In this thesis we have studied three different topics of granular gases. The dissipative nature of inelastic collisions distinguish granular gases from equilibrium molecular gases and impose many serious challenges to the proper understanding of this non-equilibrium system. We investigate the statistical properties of inelastic gases from three different perspectives, specifically the influence of heating mechanism in affecting the energy equipartition of a binary granular mixture, the experimental sampling of the micro kinematics of a 3D vibration fluidized granular gas and the power fluctuations in a boundary driven granular gas.

First we have demonstrated by event-driven molecular dynamics simulations that with selective differential boundary heating, the level of energy non-equipartition is changed remarkably even in regions spatially deep in the bulk. Reorganizing the kinetic temperature of particles as a function of particle-particle collision times fortifies this finding. Additionally, we designed a numerical model and a solvable stochastic model for a binary granular mixture without spatial ingredients, and the same effect was verified. Our result illustrate that not only mechanical properties, but also external heating play an important role in determining the energy non-equipartition level of a granular mixture. Compared with equilibrium systems, the memory from boundaries persists in the bulk of a granular gas. The reason for this long memory effect remains to be answered. Our result suggests for new kinetic theory incorporating this long memory effect, especially when people want to compare kinetic theory

predictions from homogeneous systems to experimental results of boundary driven systems.

Our experiments of high speed imaging on a vibration fluidized 3D granular gas provides detailed measurements of the granular temperature and velocity distributions. The distribution of velocity is found to be independent of smoothness of the driving boundary, external vibration frequency and amplitude. This distribution is shown to be different from the robust form first predicted in homogeneous heating granular gases and later found in 2D experiments, where the function $P(c) \sim \exp(-Ac^\beta)$ with $\beta = 1.5$. The tail of the distribution continuously broadens with increasing volume fraction. Good fitting with Sonine expansion is only found at low volume fraction. No available kinetic theory predicts the distribution we found at higher volume fraction, thus calling for theoretical development for boundary-driven systems.

Finally we numerically investigated two types of power fluctuations in a 2D boundary driven granular system. We tried to apply the so called fluctuation relation predicted in the recent Fluctuation Theorem(FT) by Gallavotti and Cohen to these two types of fluctuations. We found good agreement between the fluctuation relation and our statistics of both types of power fluctuations. In addition, an effective temperature inherently arising from the fluctuation relation is studied with various system parameters. We found that the effective temperature does not depend on kinetic temperature and system width, but does depend on elasticity, number density and sampling box height. We have to mention that our system does not satisfy some of the conditions required by the theorem. Neither of the two types of power is equivalent to the entropy quantity which is the FT originally applied for. Therefore, there is more work needed on this topic to clarify these issues.

Our experiments and simulations on granular gases have provided new insights into the physical properties of granular gases. However, there are new questions emerged

with these new findings at the same time to challenge physicists in the future study of granular gases. We would briefly bring the attention to a few of these questions.

Energy non-equipartition in granular mixtures poses the problem of using kinetic energy of particles as the definition of granular temperature. Our results about the persistent effect of the boundary heating mechanism on the extent of non-equipartition in a binary granular system lead to concern about comparing theories of homogeneously heated granular systems to boundary-driven experiments. It looks that details of boundary heating mechanism should not be ignored in determining the dynamics of a granular system. This brings challenge to incorporate this issue in the future development of kinetic theories of granular gases. Similar effect can be anticipated in the energy non-equipartition of translational and rotational degree of freedom in a monodisperse boundary-driven granular system. Study of this effect in addition to the mechanical properties of particles is needed.

Understanding the distribution of velocity is one of the crucial problems for the development of kinetic theory of a granular gas. Our measurements of the 3D particle kinematics find different forms of distribution with that found in previous 2D experiments. Neither the tail nor the small velocity part of the distribution has been captured well by the current kinetic theories of homogeneously heated systems. We do not know that if we should choose functions other than Gaussian as the base function for expansion or completely new theories should be developed for boundary driven systems. More studies are needed to elucidate the current puzzles.

The emerging of "effective temperature" from theorems other than traditional kinetic theories might provide an alternative way to the theoretical description of granular gases. Currently we are not quite clear about the seemingly good agreement of the fluctuation relation with the two types of power fluctuations in our numerical experiments. We are expecting new studies to provide better explanation. Especially if people can clarify whether the agreement is merely a linear approximation due to

limitations in the statistics for large negative power fluctuations in the capacity of experimental and simulation resources. Meanwhile, the entropy or entropy production is not well defined in granular gases. We hope that there could be more reasonable connection between the fluctuation theorem and granular gases.

In conclusion, our experiments and simulations have explored several aspects of the physical properties of granular gases. Our study on the long lived boundary effects, the measurements of micro-structure kinematics of a vibration fluidized 3D granular gas and the numerical experiments connecting fluctuation theorem to two types of power fluctuations should clarify some questions of the statistical properties of inelastic gases and contribute the study in related fields. However, much remains to be done to improve our understanding further. We wish that future work combing theoretical development, experiments and numerical simulations will elucidate these puzzles and help people to broaden our knowledge of granular materials.

APPENDIX A

ROTATIONAL DYNAMICS IN A 2D VIBRATED GRANULAR GAS

This Appendix presents a study on the rotational dynamics of a granular gas made of spheres confined to move in a vertical plane under continuous excitation by vigorous vertical vibrations. The experimental work in this project was completed in the PhD thesis of Klebert Feitosa. I performed evet-driven simulations to support the experimental results.

We study the kinematics of the spheres by high speed full field tracking of the 2-dimensional positions and 3-dimensional orientations. The results show a non-gaussian distribution of angular velocities distinct from the translational velocity distribution. In addition, the kinetic energy was found to be unequally partitioned between the rotational and translational degrees of freedom of the particles. The ratio of rotational to translational energy is independent of the vibration intensity and number density of particles for two of the components of the rotational energy. We also perform event-driven simulations of a purely 2-dimensional idealization of our system and get qualitatively matching results.

A.1 Introduction

A granular system driven to a dilute, fluidized, steady-state in which the dissipation is dominated by inter-particle collisions, is generally referred to as a *granular gas*, in analogy to a molecular gas [87]. This analogy has motivated the use of kinetic theories to describe granular gases based on the mean kinetic energy of the

particles—the granular temperature. A full description of the kinematics of colliding frictional spheres must include not only the translational motion but also rotations with a collision model that incorporates both normal inelasticity and tangential frictional impulse. Modern kinetic theories and simulations based on these models have developed a full kinetic description of the particles[5]. However, most experiments on granular gases have focused on the translational degrees of freedom only, with hardly any exploration of rotations. To fill this gap, we performed experiments and event driven simulations of a vibration fluidized 2D granular system. In this paper we report results on the distribution of angular velocities, equipartition of energy, and the temperature ratio between rotational and translational components.

Early [88, 89, 90] and more recent [91, 92] developments of a theory of rough inelastic gases find perturbation solutions of the inelastic Boltzmann equations about the Gaussian reference state. Most recent theoretical investigations of nearly smooth granular gases obtained a non-gaussian angular velocity distributions with power law tails for the homogeneous cooling state and simple shear flows [87]. Kinetic theories of rough inelastic particles [88, 89, 90] have predicted non-equipartition of energy between the translational and rotational modes of the particles. Studies of homogeneous cooling systems [53, 93, 94] predicted the energy ratio to be dependent on inelasticity in addition to the roughness of the particles. Calculations carried out for sheared systems indicated that the ratio between the rotational and total energy does not depend on system parameters, but only on the roughness of the particles. McNamara and co-workers [95] proposed that the boundary induced energy flux play an important role in determining the energy ratio: in stationary states, such as the vibrated system here reported, the ratio depends mainly on the roughness of the particles, while in non-stationary flows, such as in freely cooling systems, the ratio depends on both roughness and inelasticity. These predictions have been tested and observed in simulations [20, 95, 96].

Almost all experiments with granular gases to date [97, 27, 14, 28, 61, 66, 64, 63] have investigated only the translational dynamics of the grains. Experiments on grain rotations have generally focused on measuring contact parameters for binary or particle-plane collisions under various conditions[98, 99, 100, 101, 102, 103]. To the best of our knowledge, the only previous investigation of rotational dynamics in a granular gas was done by Warr and co-workers [104] who have performed an experiment to investigate translations and rotations of discs under vibration using high speed photography and image analysis. Among other results, they report a Maxwellian distribution of velocities, and non-equipartition of energy among the rotational and translational modes. Here we describe the results of experiments that investigate the angular components of a large collection of colliding *spheres* fluidized by intense vertical vibrations and confined to move in a two dimensional vertical plane. We compare the experiments to event driven simulations to help isolate the effects of confinement in the third dimension. The results show non-Gaussianity of velocity distributions, non-equipartition of the kinetic energy between the various degrees of freedom, but independence of the energy ratio of system parameters such as vibration velocity and particle number density.

A.2   Experimental methods

The convenience of imaging and tracking particles in a plane explains the preference for the 2D geometry in experiments of fluidized granular systems (see ref. [97, 27, 14, 28, 61, 66, 64, 63]). The granular gas is generally idealized as a collection of smooth inelastic objects, excited exclusively on the translational modes, confined to move in a plane and free of rotations. This idealization rarely matches reality. In fact, the grains are frictional 3-dimensional objects, move in a quasi-two-dimensional geometry and undergo *rotations* as they interact with other grains and the boundaries of the system. Both in our geometry and in others, the particle-boundary interactions
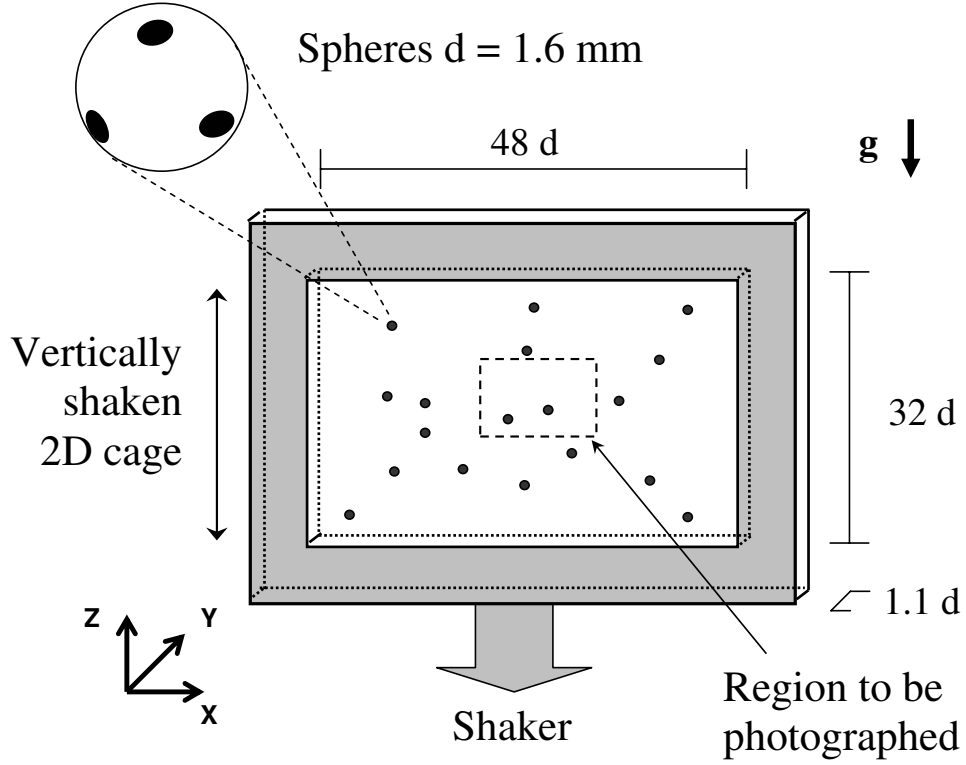
Figure A.1. Experimental set up.

contribute significantly to rotations due to the strong confinement the particles are subject to.

Our granular gas is comprised of spherical particles fluidized by intense vertical vibrations and confined to move in the vertical xz plane as shown schematically in Fig. A.1. The grains are white acetal spheres of $d = 1.6$ mm in diameter with six black dots painted on their surface to mark their orientation. They are confined to move between two vertical, parallel Plexiglas plates (henceforth *walls*) separated by a gap slightly larger than the diameter of a grain ($1.09 \pm 0.02d$). A rectangular acetal frame ($32d$ x $48d$) defines the boundaries within which the particles move. An electromechanical vibrator, (*Ling Dynamics Systems (LDS)* V400, driven by a *LDS* PA500L amplifier), provides vertical sinusoidal oscillations with accelerations up to $55g$.

The particles are photographed in a square region (side=9.4d) in the center of the cell, far from the oscillating boundaries. To ensure unambiguous tracking of positions and orientations, the photos are taken with a Phantom V7 (*Vision Research*) monochromatic camera at a rate of 10000 frames per second. In the images the spheres appear as grey circles with dark spots against a white saturated background as shown in Fig. A.2.

The positions of the spots are measured with an accuracy of 0.004d by obtaining the coordinates of the local minima in a non-thresholded input image. Due to parallax, spots located in an annular region 0.075d from the edge of the spheres look extremely deformed, preventing an accurate measurement of their location. These spots have not been included in the analysis (spots not marked by an 'x' in Fig. A.2a). The locations of the spheres are found as follows. First the images are made binary by appropriately applying a brightness threshold. Then, the binary images are subject to a morphological distance operation where each pixel is assigned its Euclidian distance to the nearest background pixel. In the resulting image, the coordinates of the local maxima correspond to the center of the spheres, which are measured with an accuracy of 0.002d. Spheres that intersect the boundaries have not been included in the analysis due to difficulties in accurately determining their centers, rotations and trajectories.

Figure A.2 illustrates the translation and rotation undergone by the spheres. Figure A.2a shows a photograph of the spheres with the positions of the center of mass (CM) of the spheres and of the spots marked. Figures A.2b and A.2c show a zoomed in view of the particle framed in Fig. A.2a. The markers represent positions of the center of mass of the sphere and of the spots taken at intervals of 0.4ms relative to (b) the laboratory frame and (c) the CM of the sphere.

Energy is transported from the oscillating boundaries to the interior of the cell by inelastic particle collisions. In order to achieve gas like behavior, the grains must
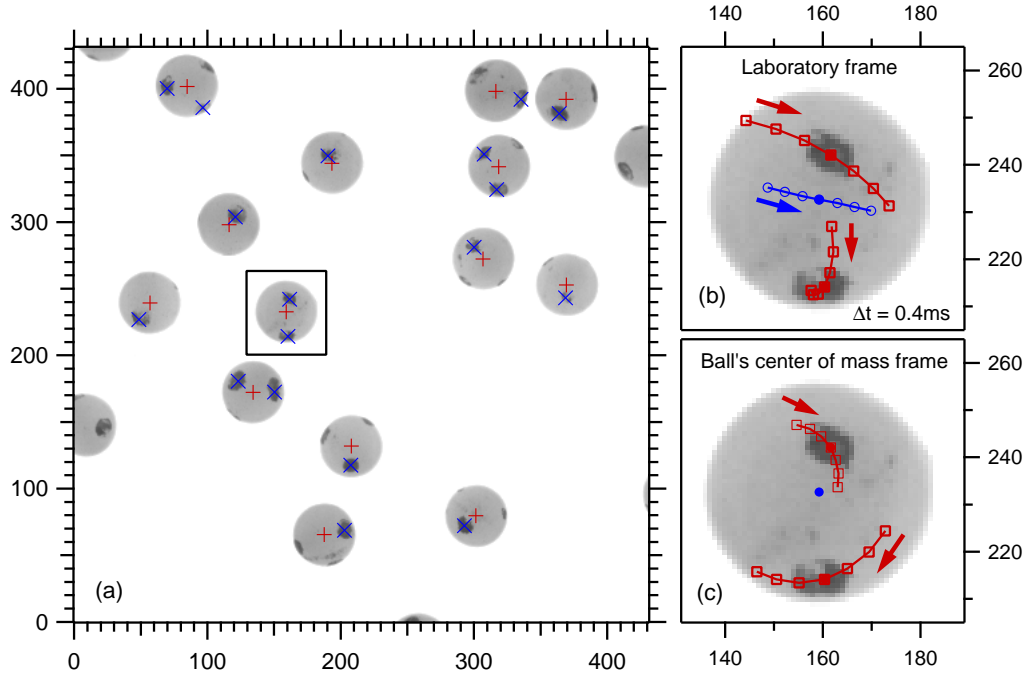
Figure A.2. (Color online) (a) Full field image of the dashed field from Fig.A.1 ($\rho = 0.11$). (+) position of the center of mass of the balls; (x) position of the center of mass of the spots. Spots not marked by an 'x' have not been included in the analysis due to inaccuracies introduced by parallax. A close-up view of the framed ball is shown on the right. (b) Successive positions of the spots and center of mass of the ball in the laboratory reference frame. Filled markers represent the positions at the instant of the snapshot. (c) Successive positions of the spots in the ball's center of mass reference frame. Arrows show the direction of motion in time.

be driven by intense vibrations to balance the losses due to collisions. Above accelerations of $35g$, the density profile asymptotes to a curve approximately symmetric about the center. In this regime, the profile shows a relatively small gradient in the center of the cell and an absence of clustering and inhomogeneities, as shown in Fig. A.3.

Before introducing the experimental results, we outline below the interactions between particles, walls and boundaries, and how they affect the various velocity components.

Translational. The vertical component of the velocity of the particles, v_z, is excited mainly by collisions with oscillating top and bottom boundaries. The horizontal component, v_x, together with the vertical component experience exchange of momentum with angular components during inter-particle collisions. Additionally, they may be excited by sliding collisions with the moving walls.

Rotational. Following our choice of axes (see Fig. A.1), angular velocity components about the x and z directions, ω_x and ω_z, are excited by particle-wall and inter-particle collisions. Under slip conditions, the particles experience energy loss, whereas in non-slip collisions they may experience gain in rotational energy. In contrast, the angular velocity component about the y direction, ω_y, is excited *exclusively* by particle-particle interactions. Since the particle-wall interactions are experimentally inaccessible and thus cannot be quantified, the ω_y component is better suited to investigate energy exchanges and ratios between rotational and translational modes.

Having no access to the direction perpendicular to the plane of motion, we are barred from decoupling the rotations due to particle-particle interactions and particle-boundary interactions. Apart from a somewhat greater contribution of the boundaries to the rotational dynamics, our system is in every respect representative of the general class of systems known as vibrated granular beds.

88
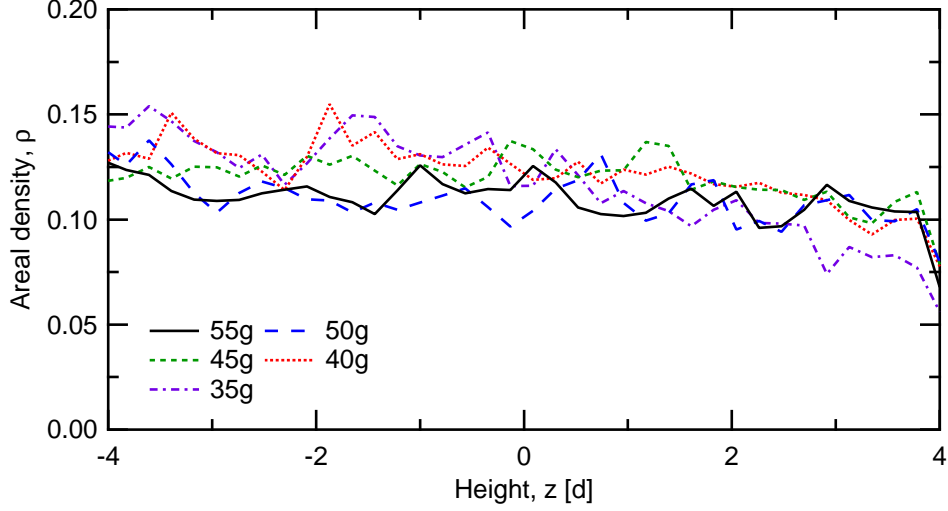
Figure A.3. (Color online) Experimental areal density vertical profile for various accelerations at fixed total area density $\rho_{total} = 0.11$.

A.3 Simulation methods

An event driven molecular dynamics simulation was performed to compare and complement the results of the experiments. Particles of mass m and diameter d move freely under the influence of gravity g inside a 2D vertical cage with the same dimensions as that in the experiments. The cage vibrates vertically and sinusoidally with frequency f and amplitude A. In contrast with the experiment, particles in the simulations are *disks* with rotation moment $1/2$ which can only rotate along axes perpendicular to the 2D plane, corresponding to the y axis in experiments. The collision rule of these disks is characterized by a normal elastic coefficient ϵ, a dynamic friction coefficient μ and a parameter β_0 which is used to distinguish sticking contact and sliding contact [19, 20]. Without extra notation, we choose ϵ to be 0.95, μ to be 0.25 and β_0 to be 0.5 [99] to match the experimental observations.
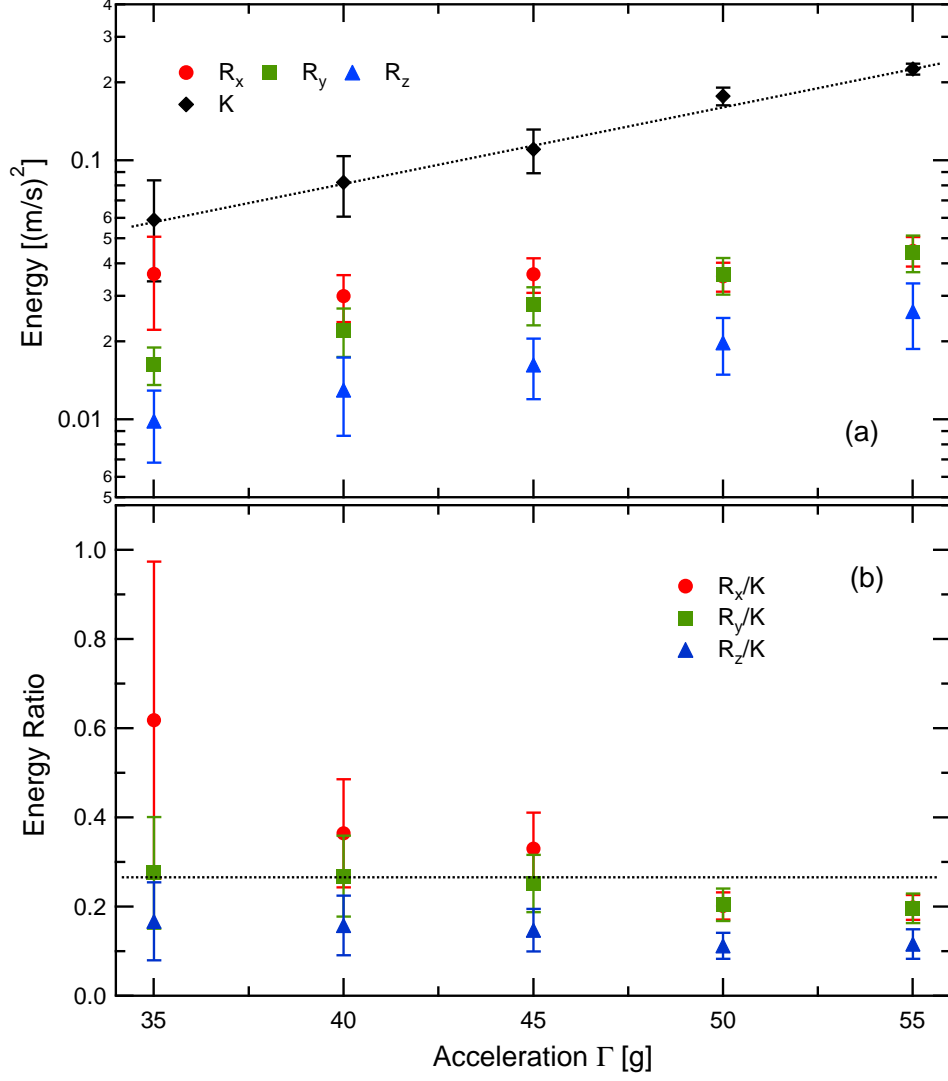
Figure A.4. (Color online) (a) Rotational (R_i) and total translational (K) energies as a function of acceleration, Γ, for fixed total area density $\rho = 0.11$. (b) Ratio between R_i and K as a function of acceleration. Dotted lines are only a guide to the eye.
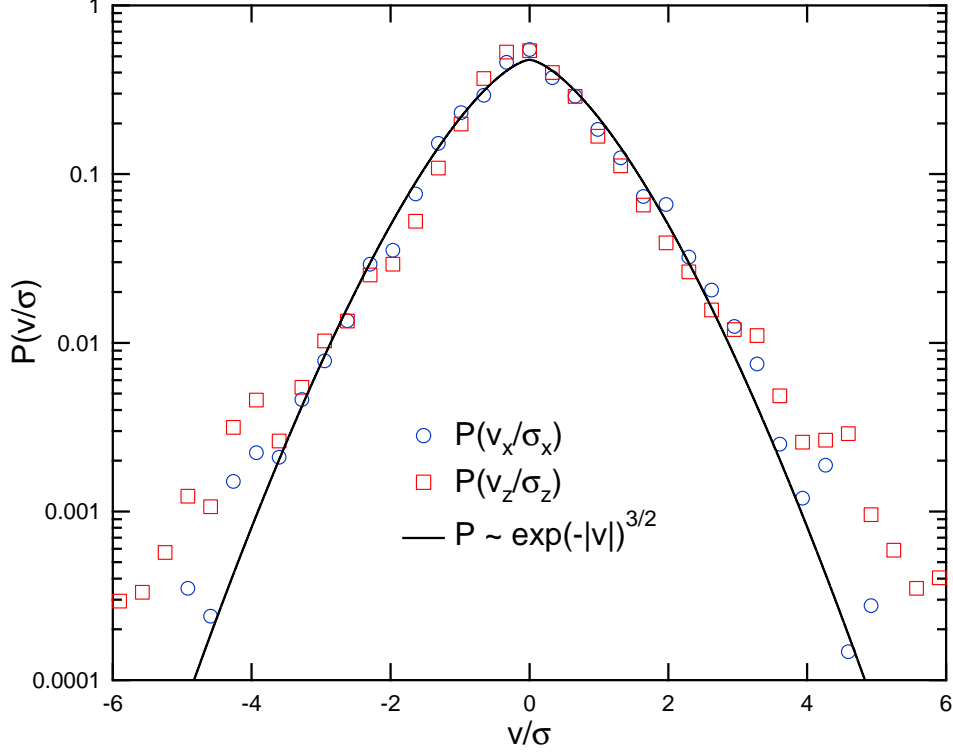
Figure A.5. (Color online) Distributions for the ($\bigcirc$) horizontal, v_x, and ($\square$) vertical, v_z, velocities for acetal spheres, normalized by the root mean square velocities, σ_x and σ_z. Line: distribution previously obtained for spheres made of different materials [14, 22] in the same apparatus. Experimental parameters: $\rho = 0.11$ and $\Gamma = 55g$.

A.4 Experimental results

A.4.1 Velocity distributions

We start with the investigation of the velocity distributions. Previous experiments with spheres of other materials in the same apparatus [14, 22] have shown a robust distribution of translational velocities that among other features is non-gaussian and independent of experimental and particle parameters. We observed the same translational velocity distribution here for the acetal spheres. As before, the distribution is fit by the function $P(v/\sigma) \sim \exp(-\delta(|v|/\sigma)^\alpha$ where $\alpha = 1.51 \pm 0.1$ is the only free parameter, $\sigma^2 = \langle v^2 \rangle$, and $\delta = 0.78$ is imposed by normalization.
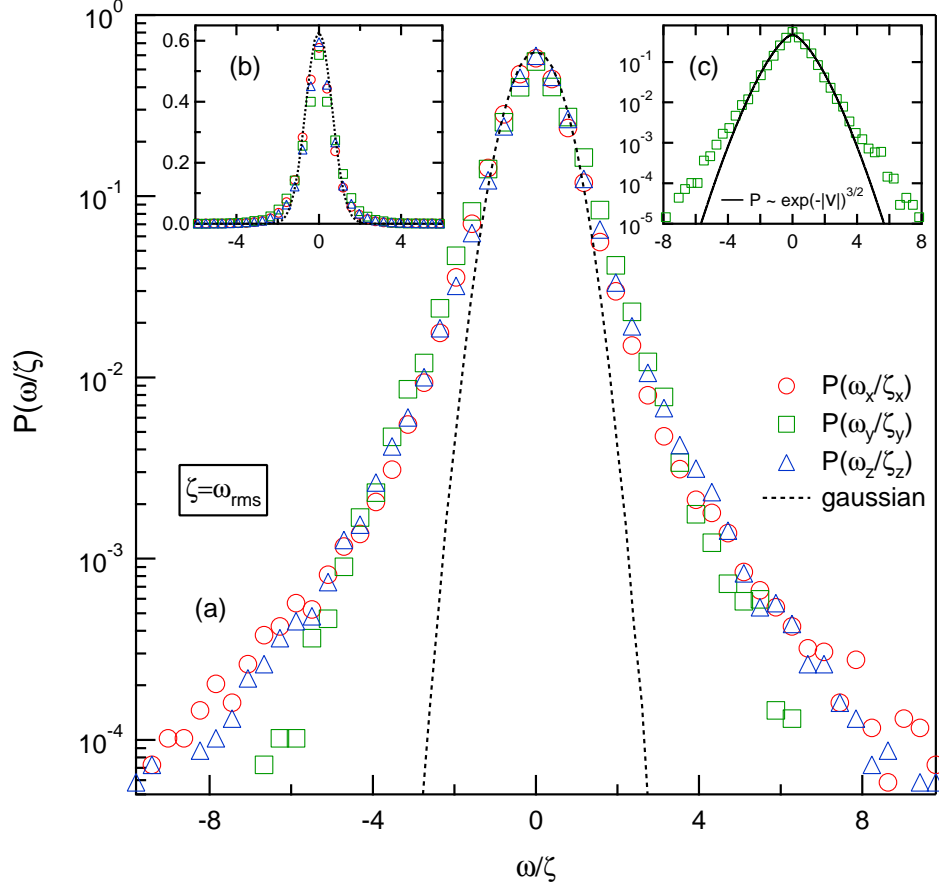
Figure A.6. (Color online) (a) Angular velocity distributions for ω_x, ω_y and ω_z in log scale ($\rho = 0.11$ and $\Gamma = 55g$). Dashed curve show a gaussian distribution. (b) Same distributions in linear scale overlayed on a gaussian curve. (c) $P(\omega_y/\zeta_y)$ overlayed on a $P \sim exp(-|v|^{3/2})$ type distribution.

The angular velocity distributions for the three normalized angular velocity components, ω/ξ, where $\xi = \langle\omega\rangle^{1/2}$ are shown in Figure A.6(a-b). As in the case of the translational velocities, the distributions deviate from a gaussian distribution, particularly on the tails. In spite of the diverse coupling mechanisms with the various energy sources the three components show strikingly similar distributions, except for subtle dispersion present in the tails where the x component has the highest velocities and the y component lowest. We believe that the differences in energy feeding mechanisms are responsible for these differences on the tails. Coupling with the oscillating walls

may be feeding more energy in the x direction whereas total absence of wall coupling mechanisms may lead to lower rotational energy in the y direction. Inset (c) depicts $P(\omega_y/\xi_y)$ compared to the distribution function obtained for the linear velocities distributions. Note that this component of the angular velocity, although exclusively coupled to the linear components by means of inter-particles collisions, shows a distribution with wider tails as compared to its horizontal translational counterpart. It is possible that this is a result of equipartition with vertical translational velocity which due to the strong coupling with the vertical vibrations display a similar excess of high velocity particles. Additionally, the range of velocities reported are comparatively narrower preventing a comparison in the tails where the deviations from Maxwellian is more pronounced.

Our results depart from those obtained in simulations of granular gases of rough particles [106] where Maxwellian distributions for the angular velocity have been observed. In contrast with our experiment, in this simulation, energy is fed exclusively into the rotational degrees of freedom. Additionally, the particles are modeled as perfectly rough, i.e., there is no frictional dissipation. Whereas reproduction of the simulation parameters in experiment is quite difficult, we were able to simulate more accurately our experimental parameters and found that the velocity distributions display the same trend observed in the experiments.

A.4.2 Granular temperature

The average kinetic energy of a granular gas, widely identified as the granular temperature, is a result of the balance between the input of energy and the losses due to inelastic collisions. The granular temperature, therefore, depends on the intensity of vibration and the number of particles in the system. We now turn to the investigation of how the granular temperatures and their ratios depend on driving and system parameters namely the acceleration and particle number density.

Figure A.4a shows the average rotational kinetic energy (R_x, R_y, and R_z) in the x, y, z directions and sum of the translational energies (K) in both x, z directions as a function of acceleration of the cell. The most immediate observation is that the energy is not equipartitioned among the degrees of freedom, even if one decouples the slightly anisotropic translational energy. We should be reminded that this might be partly due to the unequal external energy supply to translational and rotational degree of freedom, i.e. most external energy is fed by vibration to translational motion[105]. Predictably, K increases with vibration intensity, and so do R_y and R_z. Since energy is fed into these rotational components by exchange with translational energy via particle-particle and particle-wall collisions, it is not surprising that R_y and R_z increase proportionately to K for increasing accelerations. This result is captured by the ratios between the rotational and translational temperatures, shown in Fig. A.4b. Note how the ratios R_y/K and R_z/K are invariant for increasing acceleration. In contrast, R_x seems to be insensitive to changes in acceleration. Although the reasons for this distinctive behavior is still unclear, we suspect that it may be related to the fact that the oscillating walls feed energy directly into R_x in addition to the energy exchanged with the translational components. Access to wall particle interactions are necessary to fully understand the various contributions to R_x/K and R_z/K.

Figure A.7a shows the rotational and total translational energies as a function of particle number density in the cell. Again, energy is not equally partitioned, even with increasing density which reduces the mean free time and thus enhances energy exchange between translational and rotational components. With more collisions there are more dissipations and consequent decrease in the the magnitude of all kinetic granular temperatures as seen in the figure. Note that the energy ratio R_y/K and R_z/K shown in Fig. A.7b is invariant under changes in density and very close to those obtained for varying excitations. Similarly to the case for increasing acceleration,
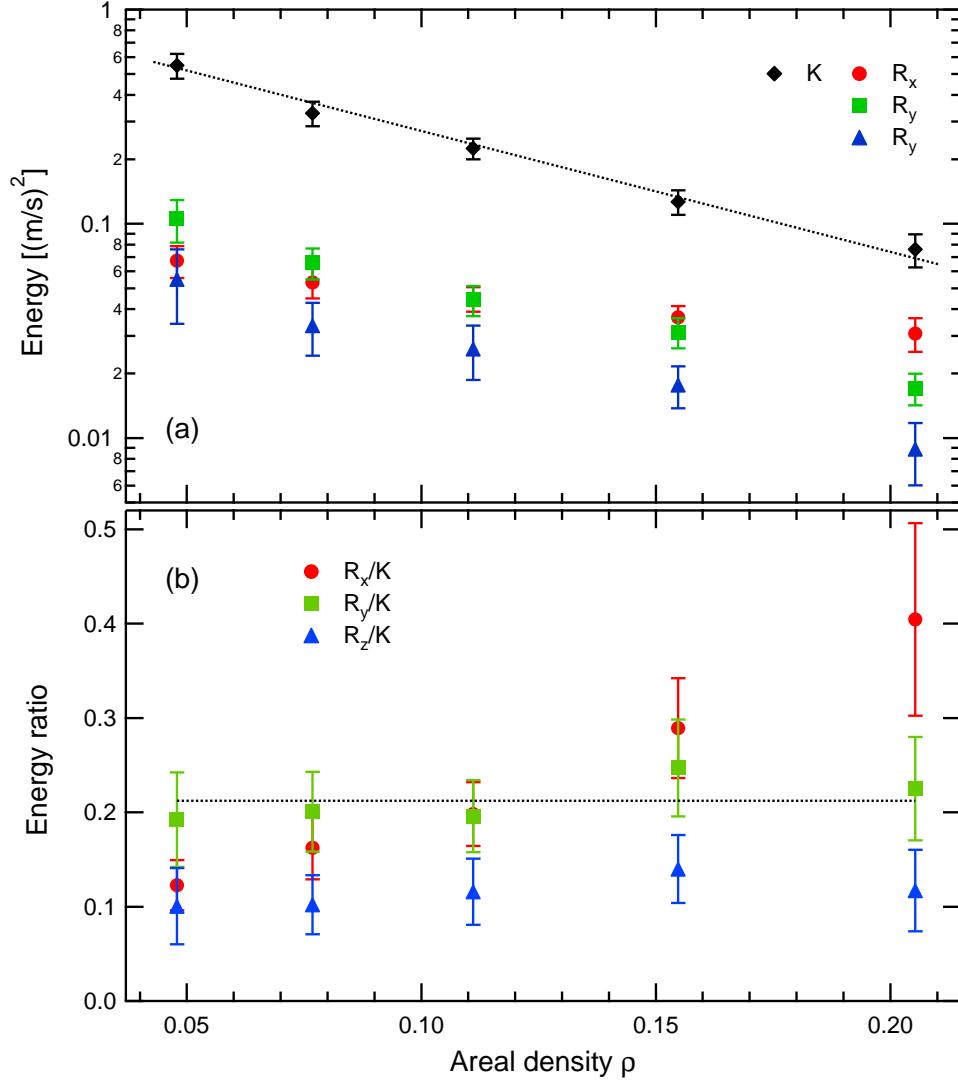
Figure A.7. (Color online) (a) Rotational (R_i) and total translational (K) energies as a function areal density for fixed acceleration $\Gamma = 55g$. (b) Ratio between R_i and K as a function of areal density. Dotted lines are only a guide to the eye.

R_x/K increase with density, a result that may be linked to the additional energy input by the oscillating walls.

The invariance of R_y/K and R_z/K with both acceleration and number density is in agreement with theoretical proposals and simulation observations that the ratios depend on particle parameters but not on parameters of the driving. This is the first experimental observation of this prediction reported in the literature.

The robustness of the above results is further verified by event-driven simulations. In contrast with Ref [95], we simulate not only β_0 but also μ to characterize roughness. The collisional rule depends on these two parameters in the process of energy exchange during a collision. An important quantity characterizing a collision is the impact angle θ, which is defined as the angle between $\overrightarrow{v_i} - \overrightarrow{v_j}$ and $\overrightarrow{r_i} - \overrightarrow{r_j}$ at contact between spheres i and j. For θ smaller than a critical angle θ_0, the two particles slide passed each other at the contact point characterizing a Coulomb contact with dynamic friction coefficient μ. For θ greater than θ_0, the Coulomb contact is broken and the two particles stick to each other at the contacting point with a roughness parameter β_0 [20, 19].

We test different μ and β_0. Fig. A.8 shows a few examples for the general trend of temperature ratio γ as a function of μ and β_0.

Fig. A.9 shows the corresponding translational and rotational energy and their ratio under different driving accelerations. Here we focus on the R_y component of the rotational energy which solely dependent on particle-particle collisions. The simulation results are in agreement with the experimental results where the energy per degree of freedom is not equipartitioned between rotational and translation motion. Also similarly to experiments, as both R_y and K increase with increasing vibration intensity, their ratio remains invariant.

Fig.A.10 illustrates the simulation results for rotational and translational energies as we fix the external driving and increase particles areal density. Again, simulation
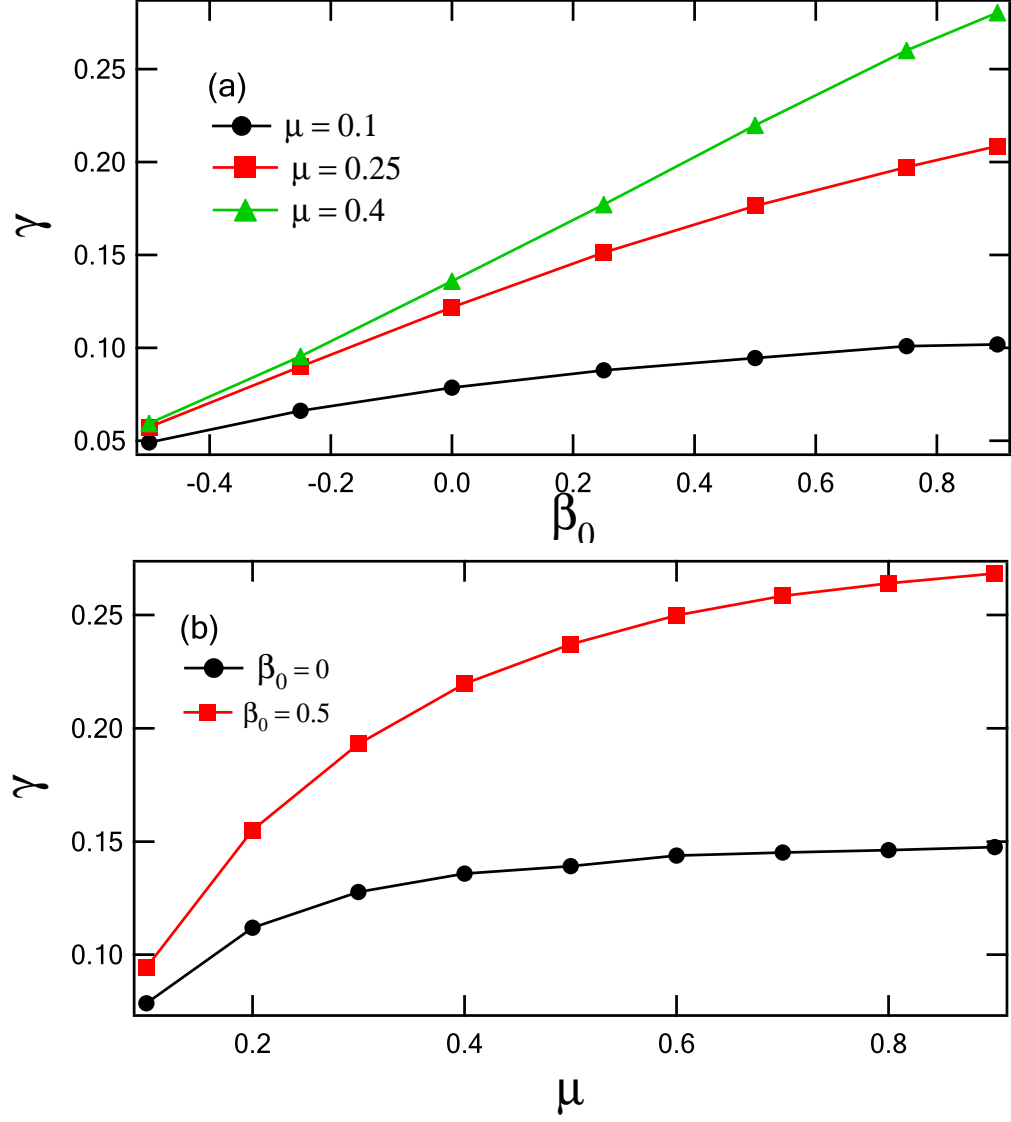
Figure A.8. Rotational and translational energy ratio γ obtained from simulation as a function of the two roughness parameters in the collision model. (a)γ as a function of β_0 with three different μ. (b)γ as a function of μ with two different β_0.
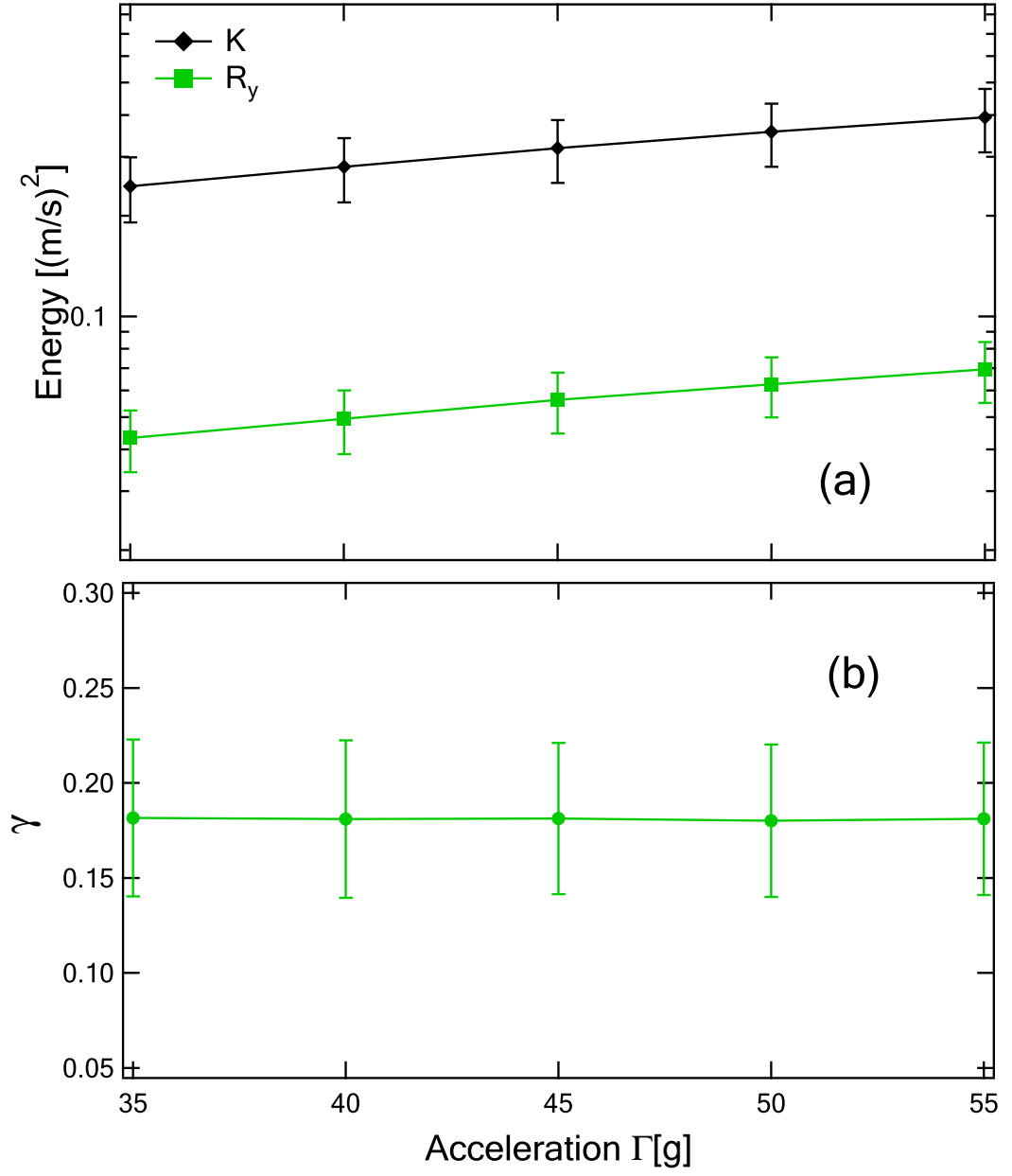
Figure A.9. Simulation results for (a)translational and rotational energy and (b) energy ratio γ as a function of external driving intensity Γ. Γ is increased from 35g to 55g by keeping the driving amplitude and changing the driving frequency.
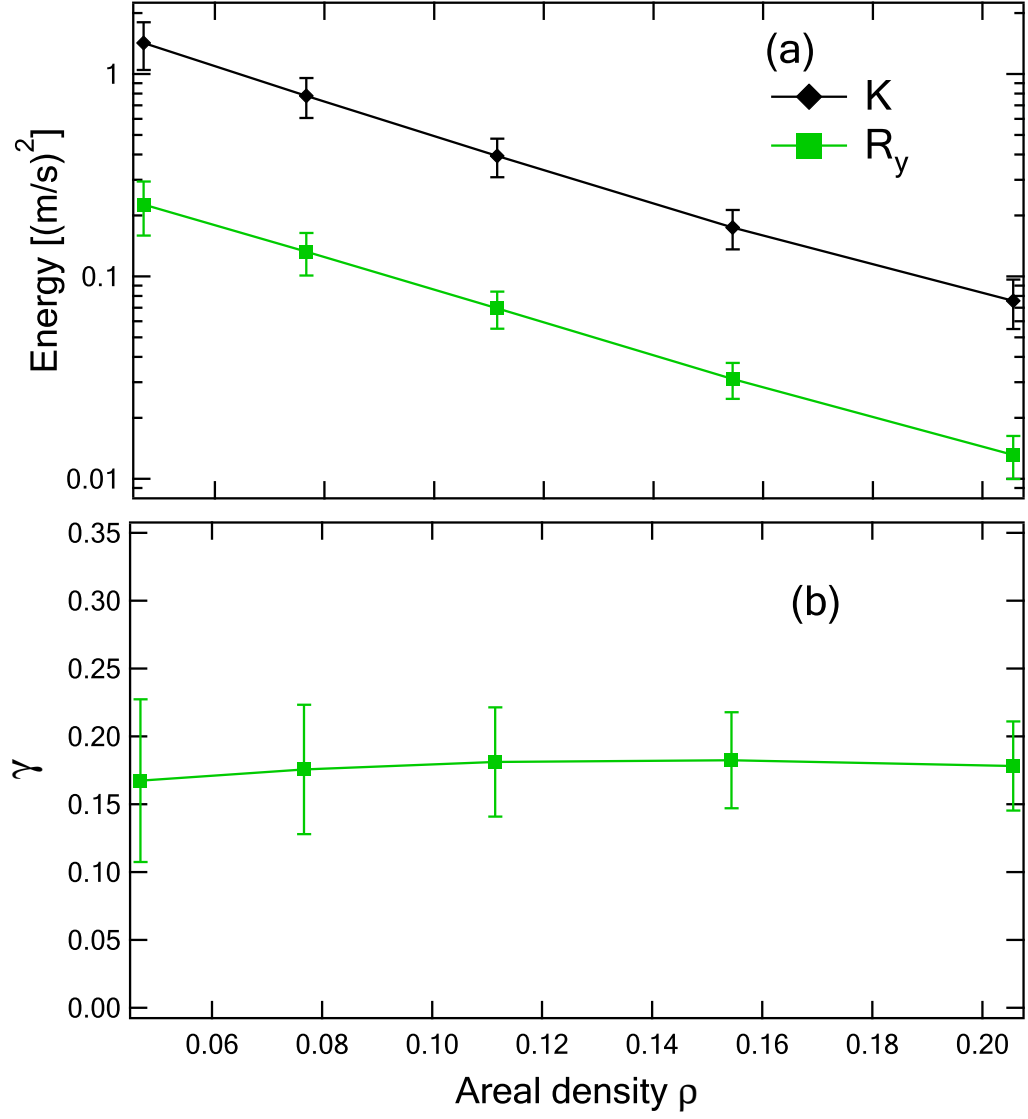
Figure A.10. Simulation results for (a)translational and rotational energy and (b) energy ratio γ as a function of areal density under fixed driving $\Gamma = 55g$.
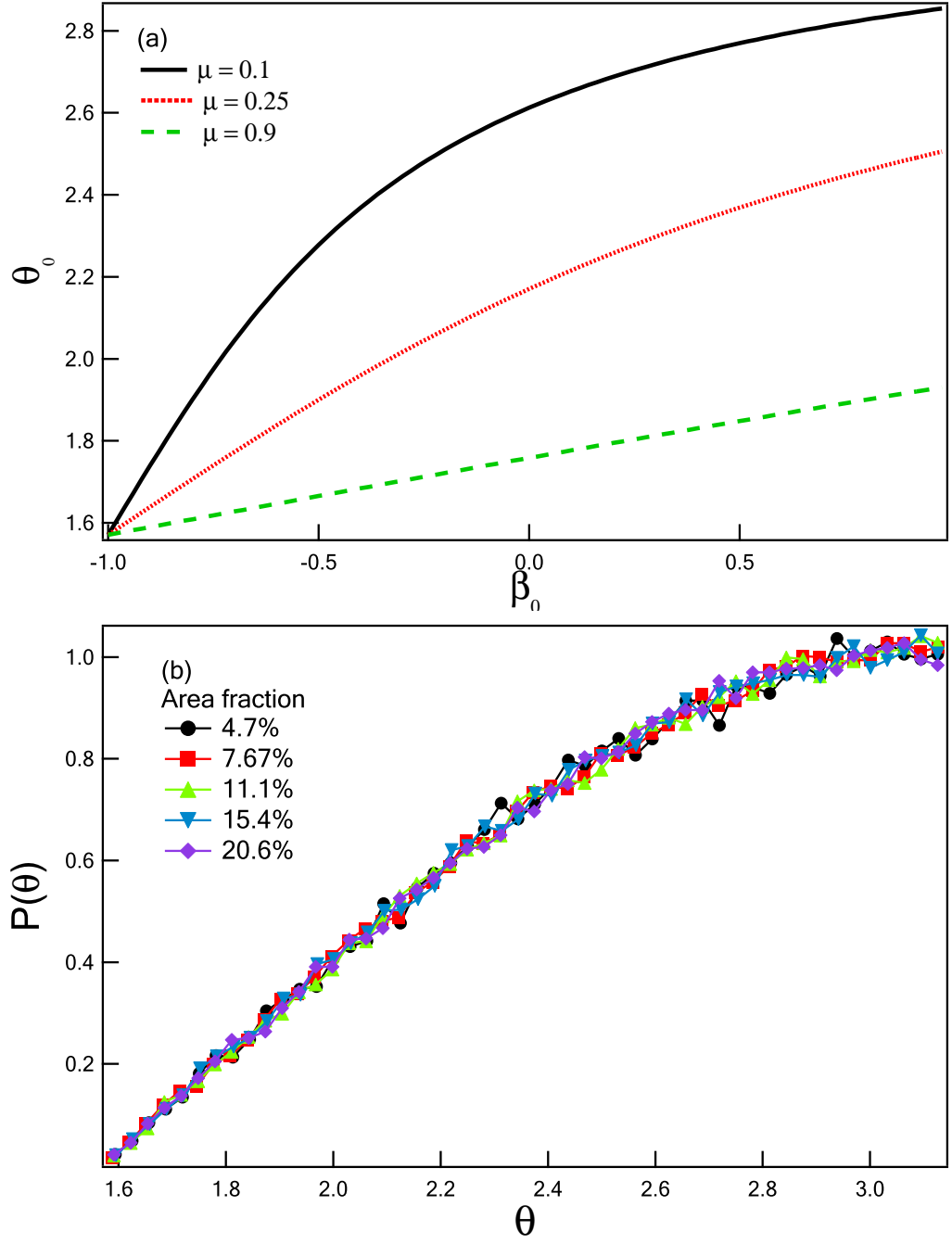
Figure A.11. (a)The critical impact angle θ_0 as a function of β_0 for three different μ. (b)The probability distribution of impact angle θ at different areal density.

results show similar trends as that in experiments. The rotational energy R_y and translational energy K decrease as the areal density increases, but their ratio remains insensitive to the change of areal density. We count that in the most dilute case (areal density 4.7%) particles experience approximately 8 particle-particle collisions on average before they collide with the top or bottom boundaries. The insensitiveness of γ on areal density was also observed in [95], where the authors found that in steady state, γ only depends on the roughness of particles. We need to point out that the collision model we use here is slightly different from [95] where the collisions are separated sliding collision type and sticking collision type, depending on the impact angle θ. We plot the critical angle θ_0 at different β_0 and μ in Fig.A.11(a) for intuitive understanding. It is straightforward to see that the smaller μ or the larger β_0, the larger θ_0. The probability distribution of θ at different areal density is shown in Fig.A.11(b). We can find that the probability distribution at various areal density agree with each other.

A.5   Conclusion

We reported in this paper an experiment to simultaneously track 2D translational and 3D rotational motion of spheres fluidized by intense vertical vibrations confined to move in a quasi bi-dimensional box. Not surprisingly for dissipative system, the velocity distributions of the particles show significant deviations from a gaussian distribution both on the translational and rotational modes. In particular, the distributions of the angular velocities display wider tails than their translational counterparts. In spite of the complex coupling between the various rotational components and the oscillating boundaries, the angular velocities distributions have identical shapes except for subtle differences in the high velocity tails. This unexpected result calls for a more thorough investigation of the different contributions of particle-boundary and particle-particle energy exchange for non-inelastic rough particles.

Our results show that the rotational energy is lower than its translational counterpart. In contrast with the rotational components coplanar with the cell, the energy supplied to R_y comes exclusively from particle-particle interactions making it suitable for comparisons with simulations studies. Remarkably, the energy ratio between R_y and the translational components are found to be independent of external driving and areal density in both experiment and simulations. Moreover, our simulations reveal that the probability distribution of impact angle is insensitive to changes in area fraction. These results may help guide future theoretical explorations that seek to construct a theory of inelastic gases that incorporates all degrees of freedom of the particles. We trust that this investigation will complement previous studies done on the same geometry, add to results of vibrated granular beds and provide valuable new insights on the role of rotations in granular gases.

APPENDIX B

IDL CODES FOR PARTICLE LOCATING USED IN THE 3D EXPERIMENTS

Algorithm for the identification of the centres of partially eclipsed spheres. The codes are written within the IDL programming environment.

```
; $Id: PTL3D.pro,v 1.0 2010/12/14 16:00:00 $
;+
; NAME:
;    PTL3D
;
; PURPOSE:
;
;   Locate eclipsed bright spheres to sub-pixel resolution from their
;     partially exposed edges.
;   Used in the experiments of 3D vibration fluidized granular gaes by
;     Hong-Qiang Wang.
;
; AUTHOR:
;
;      Hong-Qiang Wang, Ph.D.
;      Department of Physics
;      University of Massachusetts Amherst
;      email: hqwang09@gmail.com
;
; CATEGORY:
;
;      Image analysis, particle locating
;
; CALLING SEQUENCE:
;
;      Function PTL3D, img, rmin, rmax, ctdn=ctdn, mcut=mcut, rtlmx=rtlmx,
;    $
; exclude=exclude, gaugradient=gaugradient, _extra = extra
;
; INPUT PARAMETERS (required)
;
;   img:         the TIFF image to be analyzed
;   rmin:        an integer number slightly less than the radius(in unit
;    of pixels) of the feature spheres to be located
;   rmax:        an integer number slightly bigger than the radius(in
;    unit of pixels) of the feature spheres to be located
```

```
;
;  INPUT KEYWORD PARAMETERS ( optional )
;
;    ctdn:          if this keyword is set , then only gradient rays with a
     distance less than ctdn to the candidate centers
;                                    will be taken into accounted to find the
     sub−pixel particle center
;    mcut:          the cutoff value for picking up edge points after a
     Sobel operation ( default : 40)
;    rtlmx:         if this keyword is set , only locate particles to
     pixel resolution
;    exclude:       if this keyword is set , excludes particles locating
     within 2∗rmin−1 of another particle
;    gaugradient: if this keyword is set , using gaugradient instead of
     normal linear gradient , recommended to set this keyword
;    arrcut:        the cutoff value for the accumulated gradient rays
     to pick up candidate particles
;                                    the real value can be find by checking
     the variable rimg which is the image variable
;                                    for the accumulated gradient rays in the
     routine
;
;  OUTPUT
;    res:                   the first two columns contains all the particles
     found in sub−pixel resolution ( if rtlmx is not set )
;
;  DISCLAIMER
;
;    This software is provided as is without any warranty whatsoever.
;    Permission to use , copy , modify , and distribute modified or
;    unmodified copies is granted , provided this disclaimer
;    is included unchanged.
;
;  MODIFICATION HISTORY:
;
;    Packed in 12/14/2010
;=================================================================



;Function for reading 2D data ,
;fdata: name of the file containing the data to be read
;nmcol = number of columns in the data
;nmlin = number of lines in the data
Function ArrayRead , fdata , nmcol=nmcol , nmlin=nmlin

   openr , lun , fdata , / get_lun
   if not keyword_set(nmcol) then begin
      tc = fltarr (1 ,1)
      data = tc
      while not eof(lun) do begin
        readf , lun , data
        tc = [[ tc ] ,[ data ]]
      endwhile
```

```
      tc = tc[*,1:*]
   endif else begin
      if not keyword_set(nmlin) then begin
            tc = fltarr(nmcol,1)
            data = tc
               while not eof(lun) do begin
         readf,lun,data
         tc = [[tc],[data]]
      endwhile
               tc = tc[*,1:*]
       endif else begin
         tc = fltarr(nmcol,nmlin)
         readf,lun,tc
          endelse
   endelse
   free_lun,lun
   return,tc
End


;======================================================
;Name: Function WL_GradientHough_lmx
;Find local maximum points within omask
;
Function WL_lmx, array, omask=omask, arrcut=arrcut
  ON_ERROR, 2
  if not keyword_set(omask) then $
    omask = [[0,0,1,0,0],$
                   [0,1,1,1,0],$
                   [1,1,1,1,1],$
                   [0,1,1,1,0],$
                   [0,0,1,0,0]]
  sz = size(array)
  sm = size(omask)
  if(sz[0] ne 2 or sm[0] ne 2) then message,'error,_WL_lmx,_dimension_of
      _array_ne_mask'
  if(sm[1] ne sm[2] or sm[1] mod 2 ne 1) then message,'error,_WL_lmx,_
      mask_give'
  r = sm[1]/2
  mi = min(array)
  fmi=floor(mi)
  if not keyword_set(arrcut) then arrcut = ceil(mi)

  psuarray = make_array(sz[1]+2*r,sz[2]+2*r,type=sz[3])
  resarray = array
  psuarray[r:sz[1]+r-1,r:sz[2]+r-1] = temporary(array)
  w = intarr(2,1)
  mr = r*(2*r+1)+r
  for i=r, sz[1]+r-1 do begin
    for j=r, sz[2]+r-1 do begin
        mp = max(psuarray[i-r:i+r,j-r:j+r]*omask, mi)
         if mi ne mr $
            or psuarray[i,j] le arrcut then resarray[i-r,j-r] = fmi
    endfor
  endfor
```

105

```
    array = temporary(psuarray[r:sz[1]+r-1,r:sz[2]+r-1])
    w = where(resarray ne fmi, count)
    if count lt 1 then return, 0
    res = intarr(2,count)
    res[0,*] = w mod sz[1]
    res[1,*] = w / sz[1]
    return, res
End


Pro Img_Gradient, img, mimg=mimg, gimg=gimg, gw=gw, scale=scale, xdiv=
    xdiv, ydiv=ydiv
  ON_ERROR, 2
    if not keyword_set(scale) then scale = 3
    if scale mod 2 eq 0 then scale = scale +1
    scale = 3
    r = scale/2

    sz = size(img)
    simg = make_array(sz[1]+2*r, sz[2]+2*r,type=4)

    simg[r-1,r:sz[2]+r-1] = img[0,*]
    simg[sz[1]+r-1,r:sz[2]+r-1] = img[sz[1]-1,*]

    simg[r:sz[1]+r-1,r-1] = img[*,0]
    simg[r:sz[1]+r-1,sz[2]+r-1] = img[*,sz[2]-1]
    simg[r-1,r-1] = img[0,0]
    simg[r-1,sz[2]+r] = img[0,sz[2]-1]
    simg[sz[1]+r,r-1] = img[sz[1]-1,0]
    simg[sz[1]+r,sz[2]+r] = img[sz[1]-1,sz[2]-1]
    simg[r:sz[1]+r-1,r:sz[2]+r-1] = temporary(img)

    xdiv_mask = [[-1,0,1],[-2,0,2],[-1,0,1]]
    ydiv_mask = [[-1,-2,-1],[0,0,0],[1,2,1]]


    xdiv = convol(simg, xdiv_mask)
    ydiv = convol(simg, ydiv_mask)

    xdiv = xdiv[r:sz[1]+r-1,r:sz[2]+r-1]
    ydiv = ydiv[r:sz[1]+r-1,r:sz[2]+r-1]

    if keyword_set(gw) then begin

        ngw = n_elements(gw)
        gimg = (atan(ydiv[gw],xdiv[gw]) + 2*!pi) mod (2*!pi)
        mimg = ydiv[gw]^2 + xdiv[gw]^2

    endif else begin

        gimg = (atan(ydiv,xdiv) + 2*!pi) mod (2*!pi)

        mimg = sqrt(ydiv^2+xdiv^2)
    endelse
```

106

```
  img = temporary(simg[r:sz[1]+r−1,r:sz[2]+r−1])


End

;b: sigma*2^0.5
Pro Gau_Gradient,img,mimg=mimg,xdiv=xdiv,ydiv=ydiv, b=b
  if not keyword_set(b) then b = 1
 M = 2
 N = 2*M + 1
 x = indgen(N)−M
 r = x/b
 e = exp(−r^2)
 gx = e/total(e)
 gy = transpose(gx)
 dgx = x*gx
 dgx = dgx / total(abs(dgx))
 dgy = transpose(dgx)
 xdiv = convol( convol( float(img), dgx), gy)
 ydiv = convol( convol( float(img), dgy), gx)
 mimg = (xdiv^2+ydiv^2)^0.5
End



Function PTL3D, img, rmin, rmax, ctdn=ctdn, mcut=mcut,rtlmx=rtlmx, $
exclude=exclude, gaugradient=gaugradient, _extra = extra
;maxcircles = mxc, weighted=weighted
        if not keyword_set(mcut) then mcut = 40
    sz = size(img)

    mimg = fltarr(sz[1],sz[2], /NOZERO)      ; local big gradient points
    xdiv = fltarr(sz[1],sz[2], /NOZERO)
    ydiv = fltarr(sz[1],sz[2], /NOZERO)
        if keyword_set(gaugradient) then Gau_Gradient,img,mimg=mimg,xdiv
            =xdiv,ydiv=ydiv $
    else Img_Gradient,img,mimg=mimg,xdiv=xdiv,ydiv=ydiv
    rimg = fltarr(sz[1],sz[2])
    gw = where(mimg ge mcut, nw)
    lm = rmax
    ln = rmin

    xgw = gw mod sz[1]
    ygw = gw / sz[1]
    for i=0L, nw−1 do begin

      if xgw[i] gt lm and xgw[i]+lm+1 lt sz[1] and ygw[i] gt lm and ygw[
          i]+lm+1 lt sz[2] then begin

      x = xgw[i]  &  y = ygw[i]
;[1]——————————————————————————————————————————
```

107

```
      if xdiv[xgw[i],ygw[i]] ge 0 and ydiv[xgw[i],ygw[i]] ge 0 then
        begin
       if xdiv[xgw[i],ygw[i]] ge ydiv[xgw[i],ygw[i]] then begin
         dm = ydiv[xgw[i],ygw[i]]/xdiv[xgw[i],ygw[i]]
         de = dm−0.5
         xm = ceil(lm ∗ xdiv[xgw[i],ygw[i]] / mimg[xgw[i],ygw[i]])
         xn = floor(ln ∗ xdiv[xgw[i],ygw[i]] / mimg[xgw[i],ygw[i]])
         for dx = 0, xm−1 do begin
            if de ge 0 then begin
             y = y+1
             de = de − 1
            endif
            x = x+1
            if dx ge xn−1 and dx le xm then rimg[x,y] = rimg[x,y] + mimg
              [xgw[i],ygw[i]]
            de = de + dm
         endfor
       endif else begin
         dm = xdiv[xgw[i],ygw[i]]/ydiv[xgw[i],ygw[i]]
         de = dm−0.5
         ym = ceil(lm ∗ ydiv[xgw[i],ygw[i]] / mimg[xgw[i],ygw[i]])
         yn = floor(ln ∗ ydiv[xgw[i],ygw[i]] / mimg[xgw[i],ygw[i]])
         for dy = 0, ym−1 do begin
            if de ge 0 then begin
             x = x+1
             de = de − 1
            endif
            y = y+1
            if dy ge yn−1 and dy le ym then rimg[x,y] = rimg[x,y] + mimg
              [xgw[i],ygw[i]]
            de = de + dm
         endfor
       endelse
      endif else begin
```
;[2]——
```
      if xdiv[xgw[i],ygw[i]] lt 0 and ydiv[xgw[i],ygw[i]] ge 0 then
        begin
       if (−xdiv[xgw[i],ygw[i]]) ge ydiv[xgw[i],ygw[i]] then begin
         dm = −ydiv[xgw[i],ygw[i]]/xdiv[xgw[i],ygw[i]]
         de = dm−0.5
         xm = ceil(−lm ∗ xdiv[xgw[i],ygw[i]] / mimg[xgw[i],ygw[i]])
         xn = floor(−ln ∗ xdiv[xgw[i],ygw[i]] / mimg[xgw[i],ygw[i]])
         for dx = 0, xm−1 do begin
            if de ge 0 then begin
               y = y+1
               de = de − 1
            endif
            x = x−1
            if dx ge xn−1 and dx lt xm then rimg[x,y] = rimg[x,y] +
               mimg[xgw[i],ygw[i]]
            de = de + dm
         endfor
       endif else begin
         dm = −xdiv[xgw[i],ygw[i]]/ydiv[xgw[i],ygw[i]]
```

```
            de = dm−0.5
            ym = ceil(lm * ydiv[xgw[i],ygw[i]] / mimg[xgw[i],ygw[i]])
            yn = floor(ln * ydiv[xgw[i],ygw[i]] / mimg[xgw[i],ygw[i]])
            for dy = 0, ym−1 do begin
              if de ge 0 then begin
                x = x−1
                de = de − 1
              endif
              y = y+1
              if dy ge yn−1 and dy lt ym then rimg[x,y] = rimg[x,y] +
                  mimg[xgw[i],ygw[i]]
              de = de + dm
            endfor
          endelse
        endif else begin
```

——

```
          if xdiv[xgw[i],ygw[i]] lt 0 and ydiv[xgw[i],ygw[i]] lt 0 then
            begin
          if (−xdiv[xgw[i],ygw[i]]) ge −ydiv[xgw[i],ygw[i]] then begin
            dm = ydiv[xgw[i],ygw[i]]/xdiv[xgw[i],ygw[i]]
            de = dm−0.5
            xm = ceil(−lm * xdiv[xgw[i],ygw[i]] / mimg[xgw[i],ygw[i]])
            xn = floor(−ln * xdiv[xgw[i],ygw[i]] / mimg[xgw[i],ygw[i
                ]])
            for dx = 0, xm−1 do begin
              if de ge 0 then begin
                y = y−1
                de = de − 1
              endif
              x = x−1
              if dx ge xn−1 and dx lt xm then rimg[x,y] = rimg[x,y] +
                  mimg[xgw[i],ygw[i]]
              de = de + dm
            endfor
          endif else begin
            dm = xdiv[xgw[i],ygw[i]]/ydiv[xgw[i],ygw[i]]
            de = dm−0.5
            ym = ceil(−lm * ydiv[xgw[i],ygw[i]] / mimg[xgw[i],ygw[i]])
            yn = floor(−ln * ydiv[xgw[i],ygw[i]] / mimg[xgw[i],ygw[i
                ]])
            for dy = 0, ym−1 do begin
              if de ge 0 then begin
                x = x−1
                de = de − 1
              endif
              y = y−1
              if dy ge yn−1 and dy lt ym then rimg[x,y] = rimg[x,y] +
                  mimg[xgw[i],ygw[i]]
              de = de + dm
            endfor
          endelse
```

——

```
          endif else begin  ;if xdiv[0] ge 0 and ydiv[0] lt 0 then begin
          if xdiv[xgw[i],ygw[i]] ge (−ydiv[xgw[i],ygw[i]]) then begin
```

```
                        dm = −ydiv[xgw[i],ygw[i]]/xdiv[xgw[i],ygw[i]]
                        de = dm−0.5
                        xm = ceil(lm * xdiv[xgw[i],ygw[i]] / mimg[xgw[i],ygw[i]])
                        xn = floor(ln * xdiv[xgw[i],ygw[i]] / mimg[xgw[i],ygw[i]])
                        for dx = 0, xm−1 do begin
                           if de ge 0 then begin
                              y = y−1
                              de = de − 1
                           endif
                           x = x+1
                           if dx ge xn−1 and dx lt xm then rimg[x,y] = rimg[x,y] +
                               mimg[xgw[i],ygw[i]]
                           de = de + dm
                        endfor
                     endif else begin
                        dm = −xdiv[xgw[i],ygw[i]]/ydiv[xgw[i],ygw[i]]
                        de = dm−0.5
                        ym = ceil(−lm * ydiv[xgw[i],ygw[i]] / mimg[xgw[i],ygw[i]])
                        yn = floor(−ln * ydiv[xgw[i],ygw[i]] / mimg[xgw[i],ygw[i
                            ]])
                        for dy = 0, ym−1 do begin
                           if de ge 0 then begin
                              x = x+1
                              de = de − 1
                           endif
                           y = y−1
                           if dy ge yn−1 and dy lt ym then rimg[x,y] = rimg[x,y] +
                               mimg[xgw[i],ygw[i]]
                           de = de + dm
                        endfor
                     endelse
                  endelse
               endelse
            endelse
            endif
         endfor

;Locate the local maximum points from the PTL3D transformed image

      if keyword_set(exclude) then begin
        omask = get_mask(2*rmin−1)
        lmx = WL_lmx(rimg, omask=omask, _extra=extra)
          endif else begin
            lmx = WL_lmx(rimg, _extra=extra)
          endelse

      if n_elements(lmx) eq 1 then begin
        print, 'no particles found!'
        RETURN, 0
      endif

          if keyword_set(rtlmx) then begin
            rimglmx = reform(rimg[lmx[0,*],lmx[1,*]],1,n_elements(lmx
                [0,*]))
```

110

```
                    return, [lmx,rimglmx]
                 endif
       nm = n_elements(lmx[0,*])

           rimglmx = rimg[lmx[0,*],lmx[1,*]]
           rimglmx = reform(rimglmx,1,nm)

           if n_elements(extra) gt 0 then begin
              tagextra = tag_names(extra)
              tagindex = where(tagextra eq 'SAVERIMG', count)
              if count gt 0 then begin
                 if extra.saverimg ne 0 then begin
                         res = [lmx[0,*],lmx[1,*],rimg[lmx[0,*],lmx
                            [1,*]]]
                       return,res
                 endif
              endif
           endif


;————————————————————————————————————————————
; reconstrcut the list of boundary points whose gradient passing lmx
;————————————————————————————————————————————
       gms = make_array(3,nw,/long)   ; The 1st and 2nd column of gms
           contain the x and y position of those
                            ; boundary points selected from those gradient
                               lines passing the center
                            ; points lmx, inherited from lmx, the 3rd
                               contains the index #
       nms = make_array(nm,/long)      ; # of points in gms for each lmx
           points
       k = 0L
       lm2 = lm^2
       ln2 = ln^2
       for i=0, nm-1 do begin
         tempw = where(abs(xgw - lmx[0,i]) le lm and abs(ygw-lmx[1,i]) le
             lm, ntempw)
         for j=0, ntempw-1 do begin
           x0 = xgw[tempw[j]] & y0 = ygw[tempw[j]]
           if xdiv[x0,y0]*(lmx[0,i]-x0) ge 0 and ydiv[x0,y0]*(lmx[1,i]-y0)
               ge 0 then begin

                 if keyword_set(ctdn) then begin
                   dn = abs((x0-lmx[0,i])*ydiv[x0,y0] - (y0-lmx[1,i])*xdiv[
                       x0,y0]) $
                       / sqrt( xdiv[x0,y0]^2 + ydiv[x0,y0]^2 )
                             if dn gt ctdn then continue
                         endif

                 de = (x0-lmx[0,i])^2+(y0-lmx[1,i])^2
                 if de le lm2 and de ge ln2 then begin
                   gms[0,k] = x0
                   gms[1,k] = y0
                   gms[2,k] = i
                   nms[i] = nms[i] + 1
```

111

```
                        k = k + 1
                    endif
            endif
        endfor

    endfor

    tempw = where( nms gt 20, ntempw )
    lmx = lmx[*,tempw]
    nms = nms[tempw]
    nm = ntempw

    gms = gms[*,0:k-1]
    stgms = sort(gms[2,*])
    gms = gms[*,stgms]
    ttw = 0
    for i=0L, ntempw-1 do begin
        tw = where(gms[2,*] eq tempw[i])
        ttw = [ttw,tw]
    endfor
    ttw=ttw[1:*]
    gms = gms[*,ttw]

    fgms = float(gms[0:1,*])+.5


;------smallest sum distance between center point and rays------
    res_2 = fltarr(3,nm)
    if keyword_set(oldsweep) then begin
        res_2[2,*] = 1e10
        k = 0
        l = 0
        de = 0
        while k lt nm do begin
            x0 = lmx[0,k]+.5 & y0 = lmx[1,k]+.5
            xn = -1 & yn = -1
            while 1 do begin
             for xm = -0.45, 0.5, 0.1 do begin
              for ym = -0.45, 0.5, 0.1 do begin
                x = x0 + xm
                y = y0 + ym
                dm = total(abs((x-fgms[0,l:l+nms[k]-1])*ydiv[gms[0,l:l+nms[k
                    ]-1], gms[1,l:l+nms[k]-1]] $
                        -(y-fgms[1,l:l+nms[k]-1])*xdiv[gms[0,l:l+nms[k]-1],
                            gms[1,l:l+nms[k]-1]]) $
                        / sqrt( xdiv[gms[0,l:l+nms[k]-1], gms[1,l:l+nms[k
                            ]-1]]^2 $
                            +ydiv[gms[0,l:l+nms[k]-1], gms[1,l:l+nms[k
                                ]-1]]^2 )) $
                        / nms[k]
                if dm lt res_2[2,k] then begin
                    res_2[0,k] = x
                    res_2[1,k] = y
                    res_2[2,k] = dm
```

```
        endif
      endfor
    endfor

    if abs(res_2[0,k]-xn) lt .005 and abs(res_2[1,k]-yn) lt .005 then
        begin
      break
    endif else begin
      xn = res_2[0,k]
      yn = res_2[1,k]
    endelse

    if x0 le 1 or x0 ge sz[1]-2 or y0 le 1 or y0 ge sz[2]-2 then
        break

    if xn-x0 lt -0.4 then begin          ;6   5   4
      if yn-y0 lt -0.4 then begin        ;
                                         ;7   0   3
        x0 = x0 - .9 & y0 = y0 - .9   ;
      endif else begin                   ;8   1   2
        if yn-y0 gt 0.4 then begin
          x0 = x0 - .9 & y0 = y0 + .9
        endif else begin
          x0 = x0 - .9
        endelse
      endelse
    endif else begin
      if xn-x0 gt 0.4 then begin
        if yn-y0 lt -0.4 then begin
          x0 = x0 + .9 & y0 = y0 - .9
        endif else begin
          if yn-y0 gt 0.4 then begin
            x0 = x0 + .9 & y0 = y0 + .9
          endif else begin
            x0 = x0 + .9
          endelse
        endelse
      endif else begin
        if yn-y0 lt -0.4 then begin
          y0 = y0 - .9
        endif else begin
          if yn-y0 gt 0.4 then begin
            y0 = y0 + .9
          endif else begin
            break
          endelse
        endelse
      endelse
    endelse
  endwhile

;-------Change the 3rd column of res_2 to mean radius
```

```
            res_2 [2 ,k] = total (sqrt ((x−fgms [0 ,l:l+nms[k]−1])^2+(y−fgms [1 ,l:l
                +nms[k]−1])^2))/nms[k]
;────────────────────────────────────────────────


        l = l + nms[k]
        k = k+1
      endwhile
   endif else begin
      l = 0
      k = 0
      while k lt nm do begin
        c_i = fgms [0 ,l:l+nms[k]−1] * ydiv [gms[0 ,l:l+nms[k]−1], gms[1 ,l:l+
            nms[k]−1]] − $
                          fgms [1 ,l:l+nms[k]−1] * xdiv [gms[0 ,l:l+nms[k]−1],
                              gms[1 ,l:l+nms[k]−1]]
        abi = mimg [gms[0 ,l:l+nms[k]−1], gms[1 ,l:l+nms[k]−1]]^2
        c_1 = total(−ydiv [gms[0 ,l:l+nms[k]−1], gms[1 ,l:l+nms[k]−1]] * c_i
            / abi )
        c_2 = total ( xdiv [gms[0 ,l:l+nms[k]−1], gms[1 ,l:l+nms[k]−1]] * c_i
            / abi )
          a_11 = total ( (ydiv [gms[0 ,l:l+nms[k]−1], gms[1 ,l:l+nms[k]−1]])
              ^2 / abi )
          a_12 = total ( −ydiv [gms[0 ,l:l+nms[k]−1], gms[1 ,l:l+nms[k]−1]]
              * $
                                    xdiv [gms[0 ,l:l+nms[k]−1], gms[1 ,l:l+
                                        nms[k]−1]] / abi)
          a_22 = total ( (xdiv [gms[0 ,l:l+nms[k]−1], gms[1 ,l:l+nms[k]−1]])
              ^2 / abi)

          denom = a_11 * a_22 − a_12^2
          res_2 [0 ,k] = (c_2*a_12 − c_1 * a_22) / denom
          res_2 [1 ,k] = (c_1*a_12 − c_2 * a_11) / denom
          res_2 [2 ,k] = total (abs( xdiv [gms[0 ,l:l+nms[k]−1], gms[1 ,l:l+
              nms[k]−1]] * res_2 [1 ,k] − $
                                      ydiv [gms[0 ,l:l+nms[k]−1], gms
                                          [1 ,l:l+nms[k]−1]] * res_2
                                          [0 ,k] + c_i ) $
                                  /( xdiv [gms[0 ,l:l+nms[k]−1], gms[1 ,l:l
                                      +nms[k]−1]]^2 + $
                                      ydiv [gms[0 ,l:l+nms[k]−1], gms[1 ,l:l
                                          +nms[k]−1]]^2)^0.5) / nms[k]


          l = l + nms[k]
      k = k+1
          endwhile
   endelse


        return ,res_2
End

;Program purpose: testing the accuracy of centers found by PTL3D for
    partial circles
```

114

```
;img: N x X x Z, three dimensional arrary, containing N images in size X
     versus Z
;dia: estimated decimal diameter of circles
;arrcut: arrcut for circles
Pro GH_test, img, dia, usegms=usegms, arrcut=arrcut
  sz = size(img)
  center = fltarr(3,sz[1])
  rmin = floor(dia)
  rmax = ceil(dia)
  if sz[0] ne 3 or sz[2] le rmax*4 or sz[3] le rmax*4 then message,'
     error, __GH_test,_input_image_too_small'
  if not keyword_set(arrcut) then arrcut =10000


  mask = indgen(2,sz[2],sz[3])
  mask[0,*,*] = indgen(sz[2],sz[3]) mod sz[2]
  mask[1,*,*] = indgen(sz[2],sz[3]) / sz[2]

  nangle = 6
  res = fltarr(sz[1], 2*rmax+1, nangle)  ;for moving masks with the same
       radius
  ret = fltarr(sz[1], 2*rmax+1, nangle)  ;for expanding masks with the
     same center
  if keyword_set(usegms) then begin
     ratios = fltarr(sz[1],2*rmax+1, nangle)
     ratiot = fltarr(sz[1],2*rmax+1, nangle)
        temimg = bytarr(sz[2],sz[3])+1B
        teming = bytarr(sz[2],sz[3])+1B
  endif
  flag = bytarr(sz[1],2*rmax+1, nangle)  ;corresponding to res
  flah = bytarr(sz[1],2*rmax+1, nangle)  ;corresponding to ret
  r2 = rmax^2
  for i=0, sz[1]-1 do begin
    if not keyword_set(usegms) then begin
       center[*,i] = PTL3D(reform(img[i,*,*]), rmin, rmax, arrcut=arrcut)
    endif else begin
       center[*,i] = PTL3D(reform(img[i,*,*]), rmin, rmax, /savegms,
          arrcut=arrcut)
          gms = ArrayRead('gms.txt',nmcol=3)
          ngms = n_elements(gms[0,*])
          agms = bytarr(sz[2],sz[3])
          agms[gms[0,*],gms[1,*]] = 1B
       endelse

    for k=0, 2*rmax do begin
       r=2*rmax+1 - k
           for j=0, nangle-1 do begin
              in = reform(img[i,*,*])
              io = reform(img[i,*,*])
              temimg[*] = 1B
              teming[*] = 1B
              theta = j * 2 * !pi / nangle
              xi = center[0,i] + r*cos(theta)
              zi = center[1,i] + r*sin(theta)
```

115

```
                dis = reform((xi-mask[0,*,*])^2 + (zi-mask[1,*,*])^2)
                    dit = reform((center[0,i]+rmax*cos(theta)-mask[0,*,*])^2
                        + (center[1,i]+rmax*sin(theta)-mask[1,*,*])^2)
                w = where(dis lt r2, nw)
                v = where(dit lt k^2,nv)
                if keyword_set(usegms) then begin
                    if nw gt 0 then temimg[w] = 0
                    ww = where(temimg eq 1B and agms eq 1B, nww)

                    if nv gt 0 then teming[v] = 0
                vv = where(teming eq 1B and agms eq 1B, nvv)

                endif

                if nw gt 0 then in[w] = 0
                    txz = PTL3D(in, rmin, rmax, arrcut=arrcut)
                    if n_elements(txz) eq 3 then begin
                        res[i,k,j] = ((txz[0]-center[0,i])^2 + (txz[1]-
                            center[1,i])^2)^0.5
                            if keyword_set(usegms) then ratios[i,k,j] =
                                float(nww) / ngms
                        flag[i,k,j] = 1B
                endif

            if nv gt 0 then io[v] = 0
                uxz = PTL3D(io, rmin, rmax, arrcut = arrcut)
                if n_elements(uxz) eq 3 then begin
                    ret[i,k,j] = ((uxz[0]-center[0,i])^2 + (uxz[1]-center[1,
                        i])^2)^0.5
                            if keyword_set(usegms) then ratiot[i,k,j] =
                                float(nvv) / ngms
                    flah[i,k,j] = 1B
                endif

        endfor
    endfor
  endfor

  rdev = fltarr(3,rmax*2+1)       ;M1 dependence on when moving the mask
  rdew = fltarr(3,rmax*2+1)       ;M2 "
  if keyword_set(usegms) then rdev = fltarr(4,rmax*2+1)
  if keyword_set(usegms) then rdew = fltarr(4,rmax*2+1)
  for i=0,rmax*2 do begin
;----method 1 ------
        dis = reform(res[*,i,*])
    dag = reform(flag[*,i,*])
    rst = reform(ratios[*,i,*])
    w =where(dag gt 0, nw)
        if nw gt 0 then begin
            if keyword_set(usegms) then begin
                rdev[0,i] = total(rst[w]) / nw
            rdev[1,i] = total(dis[w]) / nw
            rdev[2,i] = (total((dis[w]-rdev[1,i])^2) / nw)^0.5
            rdev[3,i] = nw
```

116

```
                endif else begin
                   rdev[0,i] = total(dis[w]) / nw
                   rdev[1,i] = (total((dis[w]-rdev[0,i])^2) / nw)^0.5
                      rdev[2,i] = nw
                endelse
             endif
;----method 2 ------
     dis = reform(ret[*,i,*])
     dag = reform(flah[*,i,*])
     rst = reform(ratiot[*,i,*])
    w =where(dag gt 0, nw)
          if nw gt 0 then begin
             if keyword_set(usegms) then begin
                   rdew[0,i] = total(rst[w]) / nw
                rdew[1,i] = total(dis[w]) / nw
                rdew[2,i] = (total((dis[w]-rdew[1,i])^2) / nw)^0.5
                rdew[3,i] = nw
             endif else begin
                rdew[0,i] = total(dis[w]) / nw
                rdew[1,i] = (total((dis[w]-rdew[0,i])^2) / nw)^0.5
                   rdew[2,i] = nw
             endelse
          endif
  endfor

  tdev = fltarr(3,nangle)      ;dependence on angle, M1
  if keyword_set(usegms) then tdev = fltarr(4,nangle)
  tdew = fltarr(3,nangle)      ;dependence on angle, M2
  if keyword_set(usegms) then tdew = fltarr(4,nangle)

  for i=0,nangle-1 do begin
;---- method 1 ------
        dis = reform(res[*,*,i])
    dag = reform(flag[*,*,i])
    rst = reform(ratios[*,*,i])
        w = where(dag gt 0, nw)
          if nw gt 0 then begin
             if keyword_set(usegms) then begin
                   tdev[0,i] = total(rst[w]) / nw
                   tdev[1,i] = total(dis[w])/nw
                tdev[2,i] = (total((dis[w]-tdev[1,i])^2) / nw)^0.5
                tdev[3,i] = nw
             endif else begin
                tdev[0,i] = total(dis[w])/nw
                tdev[1,i] = (total((dis[w]-tdev[0,i])^2) / nw)^0.5
                   tdev[2,i] = nw
             endelse
          endif
;---- method 2 ------
        dis = reform(ret[*,*,i])
    dag = reform(flah[*,*,i])
    rst = reform(ratiot[*,*,i])
        w = where(dag gt 0, nw)
          if nw gt 0 then begin
```

```
                    if keyword_set(usegms) then begin
                         tdew[0,i] = total(rst[w]) / nw
                         tdew[1,i] = total(dis[w])/nw
                    tdew[2,i] = (total((dis[w]-tdew[1,i])^2) / nw)^0.5
                    tdew[3,i] = nw
                    endif else begin
                       tdew[0,i] = total(dis[w])/nw
                       tdew[1,i] = (total((dis[w]-tdew[0,i])^2) / nw)^0.5
                         tdew[2,i] = nw
                    endelse
               endif
     endfor

  pdev = fltarr(3,sz[1])   ;dependence on different particles   M1
  if keyword_set(usegms) then pdev = fltarr(4,sz[1])
  pdew = fltarr(3,sz[1])   ;dependence on different particles   M2
  if keyword_set(usegms) then pdew = fltarr(4,sz[1])

  for i=0,sz[1]-1 do begin
;---- M1 ----
          dis = reform(res[i,*,*])
     dag = reform(flag[i,*,*])
     rst = reform(ratios[i,*,*])
          w = where(dag gt 0, nw)
          if nw gt 0 then begin
            if keyword_set(usegms) then begin
                    pdev[0,i] = total(rst[w]) / nw
                    pdev[1,i] = total(dis[w])/nw
               pdev[2,i] = (total((dis[w]-pdev[1,i])^2) / nw)^0.5
                    pdev[3,i] = nw
            endif else begin
               pdev[0,i] = total(dis[w])/nw
               pdev[1,i] = (total((dis[w]-pdev[0,i])^2) / nw)^0.5
                    pdev[2,i] = nw
            endelse
          endif
;---- M2 ----
     dis = reform(ret[i,*,*])
     dag = reform(flah[i,*,*])
     rst = reform(ratiot[i,*,*])
          w = where(dag gt 0, nw)
          if nw gt 0 then begin
            if keyword_set(usegms) then begin
                    pdew[0,i] = total(rst[w]) / nw
                    pdew[1,i] = total(dis[w])/nw
               pdew[2,i] = (total((dis[w]-pdew[1,i])^2) / nw)^0.5
                    pdew[3,i] = nw
            endif else begin
               pdew[0,i] = total(dis[w])/nw
               pdew[1,i] = (total((dis[w]-pdew[0,i])^2) / nw)^0.5
                    pdew[2,i] = nw
            endelse
          endif
     endfor
```

```
openw , lun , 'rdev.txt' ,/ get_lun
printf , lun , rdev
free_lun , lun

openw , lun , 'rdew.txt' ,/ get_lun
printf , lun , rdew
free_lun , lun

openw , lun , 'tdev.txt' ,/ get_lun
printf , lun , tdev
free_lun , lun

openw , lun , 'tdew.txt' ,/ get_lun
printf , lun , tdew
free_lun , lun

openw , lun , 'pdev.txt' ,/ get_lun
printf , lun , pdev
free_lun , lun

openw , lun , 'pdew.txt' ,/ get_lun
printf , lun , pdew
free_lun , lun
End
```

BIBLIOGRAPHY

[1] P.G.de Gennes Rev. Mod. Phys.**71**, 374(1999).

[2] H.M.Jaeger, S.R.Nagel, and R.P.Behringer, Rev. Mod. Phys. **68**, 1259 (1996)

[3] Campbell CS. 1990. Rapid granular flows. Annu. Rev. Fluid Mech. 22:57-92.

[4] Levy A., Kalman H., eds. 2001. *Handbook of Converying and Handling of Particular Solids.* Amsterdam:Elsevier.

[5] Goldhirsch I., Annu. Rev. Fluid Mech.**35**, 267(2003).

[6] Goldhirsch I., Zanetti G. Phys. Rev. Lett. **70**, 1619(1993).

[7] McNamara S., Young W.R., Phys. Fluids**4**,496(1991); McNamara S., Young. W.R., Phys. Rev. E**50**,28(1994).

[8] Tan M.-L., Goldhirsch I., Phyr. Rev. Lett. **81**, 3022(1998).

[9] CKK Lun, J.Fluid Mech. **59**, 223(1991).s

[10] I. Pagonabarraga, E.Trizac, T.P.C. van Nojie and M.H.Ernst Phys. Rev. E **65**, 011303(2001).

[11] S. Chapman and T.G. Cowling, *The Mathematical Theory of Nonuniform Gases.* (Cambridge University Press, Cambridge,1970).

[12] J.T.Jenkins and S.B.Savage, Journal of Fluid Mec hanics **130**, 187(1983).

[13] C.K.K.Lun, S.B.Savage, D.J.Jeffrey and N.Chepurniy, Journal of Fluid Mechanics, **140**, 223(1984).

[14] F.Rouyer, N.Menon, Phys. Rev. Lett. **85**, 3676(2000).

[15] R.D.Wildman, J.M.Huntley, and D.J.Parker, Phys. Rev. E **63**, 061311(2001)

[16] X.Yang and D.Candela, Phys. Rev. Lett. **85**, 298(2000).

[17] J.Crocker and D.Grier, Journal of Colloid and Interface Science, **179**, 298(1996).

[18] Please refer `http://www.physics.emory.edu/~weeks/idl/` for an online tutorial of particle tracking and the related software package.

[19] O.R.Walton and R.L.Brann, J. Rheol **30**, 949 (1980), O.R.Walton, in *Particulate Two Phase Flow*, edited by M.C.Roco(Butterworth-Heinemann, Boston, 1992)

[20] S. Luding, Phys. Rev. E **52**, 4442 (1995).

[21] C.Bizon, M.D.Shattuck, J.B.Swift, W.DMcCormick, and H.L.Swinney, Phys. Rev. Lett.**80**, 57(1998).

[22] K.Feitosa, Ph.D dissertation, University of Massachusetts(2004).

[23] P.A.Thompson and G.S.Grest, Phys. Rev. Lett.,**67**, 1751(1991).

[24] P.K.Haff and B.T.Werner, Power Technology **48**, 239(1986).

[25] S.McNamara, E.G.Flekkoy, and K.J.Maloy, Phys. Rev. E **61**, 4054(2000).

[26] G. Gallavotti and E.G.D. Cohen, Phys. Rev. Lett. **74**, 2694 (1995); J. Stat. Phys. **80**,931(1995).

[27] W.Losert *et al.*, Chaos **9**, 682(1999).

[28] K.Feitosa and N.Menon, Phys. Rev. Lett., **88**, 198301(2002).

[29] R.D.Wildman and D.J.Parker, Phys. Rev. Lett. **88**, 064301(2002).

[30] A.Barrat, E.Trizac, Granular Matter **4**(2), 57(2002).

[31] Hong-qiang Wang, Guo-jun Jin, and Yu-qiang Ma, Phys. Rev. E **68**, 031301(2003).

[32] S.R.Dahl, C.M.Hrenya, V.Garzo and J.W.Dufty, Phys. Rev. E **66**, 041301(2002).

[33] A.Barrat and E.Trizac, Physical Review E **66**, 051303(2002).

[34] J.M.Montanero and V.Garzo, Molecular Simulation **29**(6-7), 357(2003).

[35] V.Garzo and J.Dufty, Phys. Rev. E **60**, 5706(1999).

[36] U.Marini Bettolo Marconi and A.Puglisi, Phys. Rev. E **66**, 011301(2002).

[37] W.A.M.Morgado, Physica A **320**, 60(2003).

[38] J.J.Brey and M.J.Ruiz-Montero, Phys. Rev. E **80**, 041306(2009).

[39] J.S.van Zon and F.C.MacKintosh, Phys.Rev.Lett. **93**, 038001(2004); J.S.van Zon and F.C.MacKintosh, Phys. Rev. E **72**, 051301(2005).

[40] Y.Srebro and D.Levine, Phys. Rev.Lett., **93**, 240601(2004); Y.Shokef and D.Levine, Phys. Rev. E **74**, 051111(2006).

[41] J.B.Knight, C.G.Fandrich, C.N.Lau, H.M.Jaeger, and S.R.Nagel, Phys. Rev. E **51**, 3957(1995).

[42] E.E.Ehrichs, H.M.Jaeger, G.S.Karczmar, J.B.Knight, V.Y.Kuperman, and S.R.Nagel, Science **267**, 1632(1995).

[43] N.Menon and D.J.Durian, Science **275**, 1920(1997).

[44] E.Falcon, S.Fauve, and C.Laroche, Eur. Phys. J.B **9**, 183(1999).

[45] R.D.Wildman and J.M.Huntley, Powder Technol, **113**, 14(2000).

[46] R.D.Wildman, J.M.Huntley, J.-P.Hansen, D.J.Parker, and D.A.Allen, Phys. Rev. E **62**, 3826(2000).

[47] X.Yang C.Huan, D.Candela, R.W.Mair, and R.L.Walsworth, Phys. Rev. Lett.,**88**, 044301(2002).

[48] C.Huan *et al.*, Phys. Rev. E **69**, 041302(2004).

[49] M.K.Cheezum, W.F.Walker and W.H.Guilford, **81**, 4, 2378(2001).

[50] *The Image Processing Handbook, 3rd ed.* by John C. Russ, CRC Press(1998).

[51] A.Barrat, E.Trizac, M.H.Ernst, J. Phys.:Condens.Matter **17**, S2429(2005).

[52] T.P.C. van Noije, M.H.Ernst, Granular Matter **1**, 57(1998).

[53] A.Goldshtein, M.Shapiro, J. Fluid Mech. **282**, 75(1995).

[54] J.J.Brey, M.J.Ruiz-Montero, D.Cubero, Phys. Rev. E **54**, 3664(1996).

[55] J.M.Montanero, A.Santos, Granular Matter **2**, 53(2000).

[56] S.J.Moon, M.D.Shattuck, J.B.Swift, Phys. Rev. E **64**, 031303(2001).

[57] S.J.Moon, J.B.Swift, H.L.Swinney, Phys. Rev. E **69**, 011301(2004).

[58] J.J.Brey, M.J.Ruiz-Montero, Phys. Rev. E **67**, 021307(2003).

[59] O.Herbst, P. Müller, M.Otto, A.Zippelius, Phys. Rev. E **70**, 051313(2004).

[60] E.Ben-Naim, J.Machta, Phys. Rev. Lett. **94**, 138001(2005).

[61] A.Prevost, D.A.Egolf, J.S.Urbach, Phys. Rev. Lett.,**89**, 084301(2002).

[62] P.M.Reis, R.A.Ingale, M.D.Shattuck, Phys. Rev. E **75**, 051311(2007).

[63] A.Kudrolli, J.Henry, Phys. Rev. E **62**, R1489(2000).

[64] I.S.Aranson, J.S.Olafsen, Phys. Rev. E **66**, 061302(2002).

[65] A.Barrat, E.Trizac, Eur. Phys. J. E **11**, 99(2003).

[66] G.W.Baxter, J.S.Olafsen, Nature **425**, 680(2003).

[67] J.S.van Zon *et al.*, Phys. Rev. E **70**, 040301(R)(2004).

[68] D.Risso, P.Cordero, Phys. Rev. E **65**, 021304(2002).

[69] D.J. Evans, E G.D. Cohen, and G. P. Morriss, Phys. Rev. Lett. **71**,2401 (1993).

[70] J. Kurchan, J. Phys. A **31**, 3719(1998); J. L. Lebowitz and H. Spohn, J. Stat. Phys. **95**,333(1999).

[71] F.Bonetto, J.L.Lebowitz, Phys. Rev. E **64**, 056129(2001).

[72] L.Biferale, D.Pierotti, and A.Vulpiani, J. Phys. A **31**, 21 (1998).

[73] S.Aumaitre, J.Farago, S.Fauve and S.McNamara, Eur. Phys. J. B **19**, 255 (2004).

[74] S.Aumaitre, S.Fauve, S.McNamara, and P.Poggi, Eur. Phys. J. B **19**, 449 (2001).

[75] W.I.Goldburg, Y.Y.Goldschmidt, and H.Kellay, Phys. Rev. Lett.**87**,245502 (2001).

[76] S.Ciliberto and C.Laroche, J. Phys. IV(France) **8**, 215 (1998).

[77] G.M.Wang, E.M.Sevick, E.Mittag, D.J.Searles, and D.J.Evans, Phys.Rev.Lett. **89**, 050601 (2002).

[78] D.M.Carberry, J.C.Reid, G.M.Wang, E.M.Sevick, Debra J.Searles, and Denis J.Evans, Phys. Rev. Lett. **92**, 140601(2004).

[79] G.M.Wang, J.C.Reid, D.M.Carberry, D.R.M.Williams, E.M.Sevick, and Denis J.Evans, Phys. Rev. E **71**, 046142(2005).

[80] R.van Zon, S.Ciliberto, and E.G.D.Cohen, Phys. Rev. Lett.**92**, 130601(2004).

[81] N.Garnier and S.Ciliberto, Phys. Rev. E **71**,060101(2005).

[82] K.Feitosa and N.Menon, Phys. Rev. Lett.,**92**, 164301(2004).

[83] A.Puglisi, P.Visco, A.Barrat, E.Trizac,F.Wijland, Phys. Rev. Lett.**95**, 110202(2005).

[84] P.Visco, A.Puglisi, A.Barrat,E.Trizac and F.Wijland, Europhys. Lett. **72**, 55(2005)

[85] F.Bonetto, G.Gallavotti, A.Giuliani and F.Zamponi, J. Stat. Mech. P05009(2006).

[86] PPuglisi A, Visco P, Barrat A, Trizac E, van Wijland F, Phys. Rev. Lett. **95**, 110202(2005).

[87] I. Goldhirsch, S.H. Noskowicz and O. Bar-Lev, J. Phys.: Condens. Matter **17**, S2591 (2005); Phys. Rev. Lett. **95**, 068002 (2005).

[88] J.T Jenkins and M.W. Richman, Phys. Fluids **28**, 3485 (1985).

[89] C.K.K. Lun and S.B. Savage, J. Appl. Mech. **54**, 47 (1987).

[90] C.K.K. Lun, J. Fluid Mech. **233**, 539 (1991).

[91] J.T. Jenkins and C. Zhang, Phys. Fluids **14**, 1228 (2002).

[92] D.K. Yoon and J.T. Jenkins, Phys. Fluids **17**, 083301 (2005).

[93] M. Huthmann and A. Zippelius, Phys. Rev. E **56**, R6275 (1997).

[94] O. Herbst, M. Huthmann and A. Zippelius, Gran. Matter **2**, 211 (2000).

[95] S. McNamara and S. Luding, Phys. Rev. E **58**, 2247 (1998).

[96] S. Luding, M. Huthmann, S. McNamara and A. Zippelius, Phys. Rev. E **58**, 3416 (1998).

[97] J.S. Olafsen and J.S. Urbach, Phys. Rev. Lett. **81**, 4369 (1998); Phys. Rev. E **60**, R2468 (1999).

[98] S.F. Foerster, M.Y. Louge, A.H. Chang and K. Allia, Phys. Fluids **6**, 1108 (1994).

[99] A. Lorenz, C. Tuozzolo and M.Y. Louge, Exper. Mech. **37**, 292 (1997).

[100] J. Calsamiglia, S.W. Kennedy, A. Chatterjee, A. Ruina and J.T Jenkins, J. Appl. Mech. **66**, 146 (1999).

[101] A.H. Kharaz, D.A. Gorham and A.D. Salman, Meas. Sci. Tech. **10**, 31 (1999); Powder Tech. **120**, 281 (2001).

[102] D.A. Gorham and A.H. Kharaz, Powder Tech. **112**, 193 (2000).

[103] H. Dong and M.H. Moys, Minerals Eng. **16**, 543 (2003).

[104] S. Warr, G.T.H. Jacques and J.M. Huntley, Powder Tech. **81**, 41 (1994).

[105] H.Q.Wang, N.Menon, Phys. Rev. Lett. **100**, 158001(2008).

[106] R. Cafiero, S. Luding and H.J. Herrmann, Europhys. Lett. **60**, 854 (2002).